FORCE GENERATION OF ACTIN FILAMENTS GROWING AGAINST A BARRIER

A THESIS SUBMITTED FOR THE DEGREE OF
DOCTOR OF PHILOSOPHY (SCIENCE)
IN PHYSICS (THEORETICAL)

by
RAJ KUMAR SADHU

Department of Physics
University of Calcutta

2019

Dedicated to

My Parents

ACKNOWLEDGEMENTS

I would like to thank my supervisor Dr. Sakuntala Chatterjee for her guidance, constant support and encouragements. I would specially thank her for giving me the opportunity to think independently that helps me a lot to understand the depth of the problems. I would also like to thank Prof. Subhrangshu Sekhar Manna for his questions and encouragements in group meetings, seminars and conferences.

I would also like to thank my B. Sc. teacher Prof. G. C. Jha and M. Sc. teacher Dr. Pankaj Mishra for their way of teaching that helps me a lot in my study.

I would like to thank my group members Subrata da and Shauri for their academic and non-academic helps and supports. I would like to thank Rakesh for his companionship and his constant academic and non academic supports. I would also like to thank my seniors Sayani di, Argya da, Suman da, Debmalya da, Shinde da, Kartik da, Somnath da, Krishnendu da, Sagar da, Biplab da, Subhajit da, Supriyo da, Nirnai da, Aslam da, my frineds and juniors Subhadip, Sumata, Sudipta, Chandreyi, Anita, Sutapa, Debasis, Ananda, Amrit, Sabana, Rahul, Imadul, Sandip, Indranil, Dheeraj, Tuhin, Keshab, Anirban and Amal for their companionship. Without them, life at S N Bose would not be so enjoyable. I would also like to thank my all friends from P. K. Roy Memorial College, Dhanbad and Indian Institute of Technology (Indian School of Mines), Dhanbad.

I would like to thank the social activity group of S N Bose centre and all its members, that helps me to spend some part of my life with the people and students of the slums. I would like to thank the organization 'Uttarpara Prerna' and all its members, specially Pritam Chatterjee for giving me the opportunity to serve our society on behalf of this organization for years. I would like to thank our singing group 'SNB Khaja Band' and all its members, specially Sarowar (Goba) da for making a pleasant and enjoyable stay in S N Bose centre. I would like to thank all the S N Bose staffs, cleaners, gardeners and cooking team for making the environment so beautiful and comfortable for stay.

Finally I would like to thank my parents, my sisters and other family members for their encouragement and support. Without them it would not be possible to reach upto this position.

PUBLICATIONS

- **Actin filaments growing against a barrier with fluctuating shape**, Raj Kumar Sadhu and Sakuntala Chatterjee, *Phys. Rev. E* **93**, 062414 (2016).

- **Actin filaments growing against an elastic membrane: Effect of membrane tension**, Raj Kumar Sadhu and Sakuntala Chatterjee, *Phys. Rev. E* **97**, 032408 (2018).

- **Actin filaments pushing against a barrier: Comparison between two force generation mechanisms**,
  Raj Kumar Sadhu and Sakuntala Chatterjee, *Eur. Phys. J. E* (In press).

CONTENTS

LIST OF FIGURES

LIST OF TABLES

1

INTRODUCTION

The cytoskeletol protein is found in most of the eukaryotic cells. It is equivalent to the skeleton of our body, which is responsible for the overall structure of the cell. The cytoskeletol consists of three major proteins: Actin filaments, microtubules and intermediate filaments, collectively known as biofilaments. Among them, actin is the most abundant protein in the eukaryotic cell. These filaments consume chemical energy, grow and generate significant amount of force. This force is used by the cell in their movements, which play an important role in morphogenesis, wound repair, cancer invasion etc. [1–5]. Actin filaments also play important role in other biological processes, like cell division, muscle contraction, cell signalling etc. In the present chapter, we discuss about the actin filaments and its force generation mechanism. In the subsequent sections, we will discuss some recent experimental and theoretical works related to this topic. Finally, we will motivate our thesis and briefly outline our results.

1.1 FORCE GENERATION BY ACTIN FILAMENTS

The actin filament is a double helical structure, consisting of two protofilaments, both grow parallel to each other. A schematic diagram of actin filament is shown in Fig. 1.1. The size of each actin monomer is roughly $5.4nm$. The actin filament is asymmetric and polar in nature where the two ends, called the pointed end and the barbed end have different properties. Polymerization is a reversible process where monomers are added and released (depolymerized) from both ends of the filament. The rate of polymerization process depends upon the actual monomer concentration near the filament end. A concentration of the monomer, at which there is no net growth of filament, is known as the critical concentration. Due to the heterogeneous nature of actin filaments, the two ends of the filaments have different critical concentrations. The pointed end of the actin filament has a critical concentration six times higher than the barbed end. Thus, at some monomer concentration, which is in between the critical concentration of the two ends, the barbed end will have a net growth while the pointed end will have a net shrink.

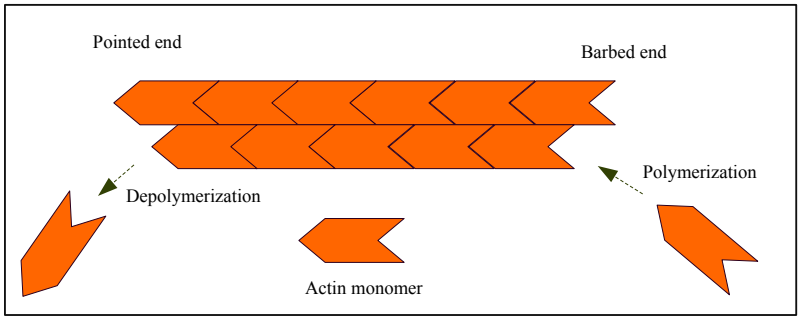

Figure 1.1: Structure of Actin filament. The actin filament is formed by two protofilaments, which grow parallelly with each other. The actin filament is asymmetric, where one end, called the barbed end has generally high growth rate than the pointed end.

The actin organises into different kind of structures, like linear bundle, two dimensional networks, three dimensional gels etc. It is mainly concentrated in a layer just beneath the plasma membrane. The growth of the barbed end of actin near the cell membrane pushes the membrane and form the protrusion (Fig. 1.2). Two types of protrusions are mainly caused by the actin polymerization: Filopodium, which are small finger like structures caused by the parallel growth of actin filaments and the lamellipodium, which are broad structures caused by the growth of branched actin networks. After the protrusion is formed, the leading edge of the cell is attached with the cell-substrate. Finally, the rare part of the cell retracts and the whole cell thus crawls forward with the help of myosin motors sliding on actin filaments. The crawling motion of the cell is a non-equilibrium process as it is continuously driven by actin networks. This process is very important in morphogenesis, would healing, tumor invasion etc. For example, during morphogenesis, there is a targeted movement of the cells to specific sites to form organs or tissues. For wound healing, cells move to the wound site to kill the micro-organisms that cause infection. In all the above examples, the cell actually crawls to reach the required target, for which the force generation by actin polymerization is responsible. Recent experimental developments and theoretical models have provided us with a better understanding of force generation by actin filaments and cell motility.

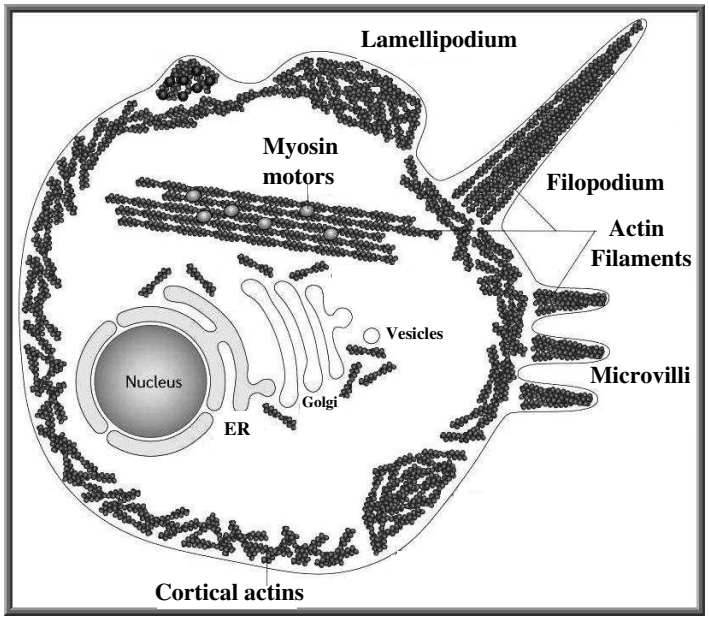

Figure 1.2: Protrusion caused by actin polymerization. Filopodium are small finger like structures, that are formed by the growth of parallel actin filaments. Lamellipodium are another type of protrusion, which are caused by the growth of branched actin filaments. The figure is produced from Ref. [6] with some modification.

1.2 EXPERIMENTAL MEASUREMENTS OF FORCE-VELOCITY CURVES

There are large number of experimental literatures, where the force generation mechanism by actin filaments have been studied [7–21]. In these experiments, the filaments are generally allowed to grow against some biological barrier and an external load (force) is applied in the opposite direction of the filament growth. The velocity of the barrier decreases as the load increases and this dependency is known as the force-velocity curve. The opposing force at which the barrier velocity becomes zero is known as the stall force. This is also known as the maximum force generated by the filaments.

The force-velocity curves are measured in many experiments, but surprisingly, the actual nature of force-velocity curve is found to depend upon the experimental set up. In [7], the forces generated in the process of actin-based propulsion is measured using a micromanipulation experiment. A comet-like structure, growing from a coated polystyrene bead is held by a micropipette while the bead is attached to a force probe. Both the pulling and pushing forces are applied and the force-velocity curve is measured. It is found that the curve is linear for pulling forces and decays more weakly for pushing forces. The nature of the force-velocity curve is thus convex. In [8], the force-velocity curve of few growing actin filaments is experimentally measured, which are growing between magnetic colloidal particles. When magnetic field is applied, the colloidal particles assemble into chains under controlled loading or spacing. When the filaments elongate, the beads separate, and the force velocity

curve is precisely measured. The force-velocity curve is found to be convex in nature. In a similar type of experiment [9], a population of actin filaments are allowed to grow against a load applied by magnetic microparticles. The filaments are arranged in stiff bundles by the actin bundling protein *fascin* and are constrained to point toward the applied load. The velocity of filament elongation is measured as a function of force. In this case also, the nature of the force-velocity curve is found to be convex.

In [10], the growth velocity of actin networks against a flexible cantilever is measured using a differential atomic force microscope. The force-velocity relationship of the growing network is measured until network elongation ceases at the stall force. They found that the growth velocity of a branched actin network is load-independent over a wide range of forces. The actual nature of the curve is found to be concave. Surprisingly, the growth velocity is found to depend upon the loading history rather than solely on the instantaneous load [10]. In [11], an atomic force microscopy cantilever is placed in the path of a migrating *keratocyte* cell. The deflection of the cantilever provides a direct measure of the force exerted by the lamellipodial leading edge. The force-velocity curve obtained from this measurement is concave. In [22], the force-velocity relationship of fish *keratocytes* cell is measured using spherical-probe-based scanning force microscope. In this case also, a concave force-velocity relation is obtained. In [12], the actin driven protrusion forces in the lamellipodium of *keratocytes* cell is studied. A vertically mounted glass fiber acted as a flexible barrier is placed in front of migrating *keratocytes* with parallel phase contrast microscopy. A laser beam was coupled into the fiber and allowed detecting the position of the fiber by a segmented photodiode. An interesting force-velocity curve is obtained in this case. The velocity initially increases with force and then decreases at high forces. They showed that the initial increase in velocity is an artifact, caused by the curved geometry of the fiber. Due to the fiber curvature, the contact area between fiber and lamellipodium increases with time. Due to the increase in contact area, more filaments push the barrier as the force increases, thus the velocity increases with force in this regime.

1.3 THEORETICAL STUDIES OF FORCE-VELOCITY CURVES

There are large number of theoretical literatures, where the force generation mechanism by actin filaments have been studied [13–19, 23–29]. In most of these literatures, the actin filaments are modelled as rod-like polymers growing and pushing against a rigid barrier (Fig. 1.3) [13, 17, 19, 23]. The filaments are allowed to grow (shrink) by the addition (subtraction) of monomers. In order to measure the stall force or force-velocity curve, an external force (F) is applied in the opposite direction of the growing filaments [13–19]. As the magnitude of the force increases, the velocity deceases and finally becomes zero at the stall force.

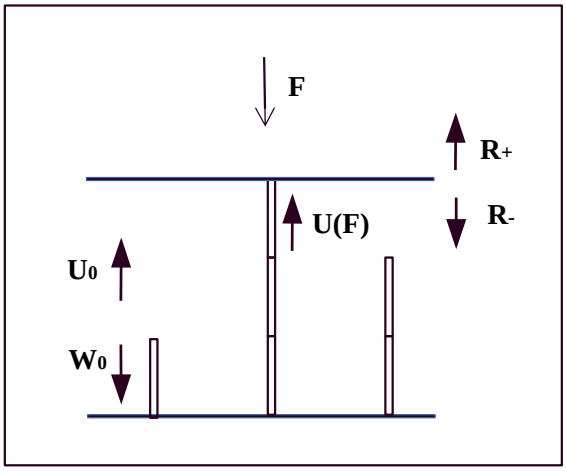

Figure 1.3: Theoretical modelling of force generation by actin filaments. The actin filaments are assumed to be rod-like elements growing in the upward direction against a rigid wall like barrier. An external force F is acting on the barrier in the opposite direction of the filament growth. The filaments, which are not in contact with the barrier, grow upward (downward) with force independent rate U_0 (W_0). The filament that is in contact with the barrier grows with force dependent rate $U(F)$. The barrier grows upward (downward) with rate R_+ (R_-), which may in general depend upon the external force.

In theoretical literatures also, the nature of force-velocity curves are found to depend upon the modelling details. Force generation by a single actin filament growing against a barrier has been explained using a simple Brownian ratchet mechanism in [13]. Thermal fluctuations of the barrier create a gap between the barrier and the filament tip, making it possible for the filament to grow by adding one monomer in the gap. This mechanism predicts a convex force-velocity curve. The above simple model has been subsequently generalized in [14], where details of interaction between the actin monomers and the barrier have been considered. This study also predicts a convex force-velocity curve. In [15], the three-dimensional dynamics of the growth of a semi-flexible actin polymer against a fluctuating obstacle is studied numerically. The velocity is measured as a function of the external load and a convex curve is obtained in this case. However, when the Brownian ratchet mechanism is extended for multiple filaments, the nature of the force-velocity curve is found to crucially depend on how the details of the interaction and load sharing among the filaments were modelled [16–19]. In [16], a two-dimensional model for lamellipodial protrusion is studied by considering the filament as well as barrier flexibility. Two types of sharing of work of protrusion is considered among the filaments: A perfect work sharing (PWS), where the total work of protrusion is divided perfectly evenly among all polymerization events and a zero work sharing (ZWS), where only the lead polymerization event does the maximum possible protrusion work. The shape of the force-velocity curves are found to be convex, but for the ZWS case, the velocity falls much faster in the small force region in comparison to the PWS case. In [17], the force generated by parallel actin filaments is studied against a rigid barrier. The

filaments do not have any lateral interactions and are only interacting mechanically with the barrier. The force-velocity curve is found to be concave for small force while convex for large force. They also identify two regimes: At low force, there is a non-condensed regime where the filaments are spread out spatially while at high force, there is a condensed regime, where filaments accumulate near the barrier. In [18], the force generation by parallel biofilaments have been studied with lateral interactions among the protofilaments. It is noted that the force-velocity curves explicitly depend upon the geometry of the filament bundles as well as the interaction strength between the protofilaments. However, the shape of the force velocity curves remain convex in any case.

There are certain models, which showed a crossover from convex to concave force-velocity curve, when some model parameters are varied [23, 30, 31]. In [30], a hybrid mesoscopic model for actin polymerization is developed that combines the microscopic dynamics of semiflexible actin filaments and the viscous retrograde flow of actin network modelled as a macroscopic gel. It is shown that the force-velocity curve can be convex as well as concave, depending on the characteristic time scale of recoil of the gel like network. In [31], the growth of multiple biofilaments have been studied against a hard obstacle in order to elucidate the nature of load sharing in the growth of these biopolymers. They vary the diffusion coefficient and the number of filaments and obtain the force velocity curve of different nature. For small number of filaments, a convex force velocity curve is obtained while for large number of filaments with large diffusion coefficient, a concave force velocity curve is obtained. In [23], the growth of branched actin networks is studied against a rigid movable wall. They use several parameters in their model: The initial distance of the movable wall form the filament tip, minimum distance between two branching point, maximum number of branches allowed to form etc. By varying these parameters, both the convex as well as the concave force-velocity curves are obtained.

1.4 MEASUREMENT OF STALL FORCE

The stall force generated by actin filaments is measured in many experimental literatures. It is found that single actin filament generates forces of the order of peconewton while actin gels or comet tails generate forces of the order of nanonewtons. In [20], assembly of actin filaments is observed using evanescent wave fluorescence microscopy. It is found that polymerization of an individual actin filament produced a force of at least 1.3 pN, close to the theoretical maximum $(\sim 2pN)$ under the same experimental conditions. In [21], the force generated by the polymerization of multiple actin filaments against a barrier is measured directly, using an optical trap. It is found that the growth of approximately eight parallel-growing actin filaments can be stalled by relatively small applied load of $1pN$, which is

equal to the theoretical stall force required to stall a single actin filament. They explain their observation by arguing that only the longest filament is in direct contact with the barrier, suggesting that the separate filaments in the bundle do not co-operate with each other in the force generation mechanism. In [12], the actin driven protrusion forces in the lamellipodium of *keratocytes* cell is studied using a glass fiber as a vertical barrier. The cell is found to stall at force $2.9 \pm 0.6nN$. Assuming the density of filaments to be 240 filament per μm, they estimated the stall force per filament to be $1.7 \pm 0.8pN$. In [7], the forces generated in the process of actin-based propulsion is measured using a micromanipulation experiment. They apply both the pulling and pushing forces in the range $-1.7nN$ to $4.3nN$. They note that a force of $4.3nN$ is not sufficient to stop the growth of the actin comet. Because of comet buckling under larger forces, the value of the stall force cannot be reached experimentally, but a lower estimate is given to be $4.3nN$. In [32], the compressive force generated by actin comet tails is studied on lipid vesicles. They developed a model system where large artificial lipid vesicles coated with the protein ActA are propelled by actin polymerization in cytoplasmic extract. They estimate the magnitude of force generated by actin comet tails in the range $0.4 - 4nN$. In [11], the force generated by growing *keratocyte* cell is measured using an atomic force microscopy cantilever. The whole cell stall force is found to be $\sim 40nN$ in this case.

The theoretical prediction of stall force for a single filament ranges form one to several piconewtons. In [17], the expression for the stall force is found to be $F_s = \frac{k_B T}{d} ln \frac{U_0}{W_0}$, where d is the actin monomer length and U_0 (W_0) is the (de)polymerization rate of actin filament. Using a monomer concentration of $0.24\mu M$, the stall force for a single filament, using the above expression is $\sim 1pN$. In [13], a similar expression for the stall force is obtained. Within a comparatively higher monomer concentration ($10\mu M$), the stall force of a single filament is found to be $\sim 7.8pN$. For multiple filaments, the stall force is found to scale linearly with the number of filaments in [17, 18, 33]. However, an absence of linear scaling of stall force with the number of filaments has been reported in [19, 29] and was explained by using effects like ATP hydrolysis of actin monomers. In [29], the force generation by multiple actin filaments has been studied using the ATP-hydrolysis. The filaments are growing against a hard obstacle which moves diffusively in the force field of an optical trap. It is noted that the stall force of N filaments is less than N times the stall force of a single filament. In another study [19], collective dynamics and force generation by biofilaments have been studied against a rigid wall using ATP (GTP)-hydrolysis of actin (microtubule) monomer. In this case, the hard wall is not diffusing but only moves when filament pushes it. The stall force of N filaments is found to be greater than N times the stall force of a single filament. Thus, unlike in [29], the collective growth of filaments enhances the stall force in this case.

1.5 IMPORTANCE OF MEMBRANE PROPERTIES ON THE FORCE GENERATION MECHANISM BY ACTIN FILAMENTS

The actin filaments grow against the cell membrane or a biological barrier in *in vitro* experiments, which has a central importance in actin polymerization and cell motility [34–37]. The mechanical characteristics of the plasma membrane, such as, the membrane tension directly affects the rate of those processes that involves the membrane deformation. For example, extension of the plasma membrane that takes place during cell motility and cell spreading depends strongly on membrane tension. In [38], the authors note that an artificial increase in membrane tension in immortalized *mouse embryonic fibroblasts* cell stopped the lamellipodia protrusion while a decrease in tension restored the protrusion. In [39], it was shown that when the membrane tension is decreased by adding certain ampiphillic compounds, the lamellopodial extension rate increases, while in situations where membrane tension is increased using osmotic methods, the extension rate drops. This observation shows that there is an inverse relationship between tension and extension rate. Although the membrane tension is generally considered as an obstacle to cell movement, it was shown in [40] that the membrane tension also optimizes the motility in *Caenorhabditis elegans* sperm cells by streamlining actin polymerization in the direction of movement. They observed that membrane tension reduction leads to an unorganized and rough lamellipodium, which composed of short filaments angled away from the direction of movement. Due to the lack of directional polymerization of filaments, the cell displacement speed is reduced. On the other hand, an increase in tension reduces lateral membrane protrusions in the lamellipodium, and filaments are longer and more oriented toward the direction of movement, thereby speed up the motility. In an *in vitro* reconstitution of lipid bilayer in [41], it has been found that membrane elasticity causes formation of filament bundles that support membrane protrusions from branched filament network. The above literatures show that plasma membrane and its elastic tension play a very important role in actin polymerization and cell motility. The cell membrane also possesses bending rigidity which has been measured in many experimental literatures [42–46]. The value of the membrane rigidity is found to depend not only on the measurement techniques but also on the environmental conditions such as immersing medium and presence of various molecules and salts. However, the effect of bending rigidity on the force generation mechanism is not directly shown in any of these experiments.

We note from above experimental literatures that the membrane, against which actin filaments grow, may in general have shape fluctuations and other properties, like elastic tension or bending rigidity etc. However, in most of the theoretical literatures, the shape fluctuations or other properties of the barrier have been neglected and it is considered as a rigid wall like object. There are, however, certain theoretical models where these properties are explicitly

considered. In [24] a flexible plasma membrane was explicitly modelled and it was shown that thermal fluctuation of this flexible obstacle substantially enhances the growth velocity of a filopodial protrusion. It was argued that in the case of a flexible membrane, a filament only has to overcome the local bending energy in order to polymerize, whereas for a rigid obstacle, the full load force must be overcome. Thus, a flexible membrane gives rise to a larger velocity for a given load. In [25], the growth of actin filaments have been studied against an elastic membrane. The elastic membrane was described using a solid-on-solid (SOS) model and the leading edge of the actin mesh was modelled by an advancing uncorrelated front. The elastic energy of the membrane is described by a one-dimensional SOS Hamiltonian, which is proportional to the contour length of the membrane. The steady-state fluctuations of the driven membrane show a non-monotonic behavior with the driving rate, where the strongly driven and weakly driven regimes are separated by a minimum in the width of the membrane profile. This similar modelling strategy is generalized in [26] to understand certain aspects of crawling motion of a cell on a flat substrate, particularly, how the asymmetry between the leading and trailing edge of the membrane decides the shape and velocity of the membrane. In [24, 27, 28], the growth dynamics of actin filaments is studied, where the energy of the membrane is described by a Helfrich Hamiltonian [47]. In [27], the growth of branched actin network is studied in order to investigate the effect of molecular transport on the force-velocity relation. The energy of the membrane is described using a Helfrich Hamiltonian, containing an elastic energy term and a bending energy term. The elastic energy is taken to be proportional to the square of height gradients while the bending energy is proportional to the square of the Laplacian of height. They note that facilitated transport of G-actin monomer helps the actin monomer to reach near the membrane leading edge and can enhance the growth of the actin network.

1.6 MOTIVATION AND PLAN OF THE THESIS

In this thesis, we study the force generation by actin filaments growing against a barrier. The filaments are polymerizing against the barrier and push it. The barrier also undergo independent thermal fluctuations, unaided by the filaments. We are interested to know how the local shape fluctuations of the barrier, its elastic properties or bending rigidity affect the force generation process. We are also interested to know how the independent dynamics of the barrier play a role in this mechanism.

In most of the theoretical literatures discussed above, the force generation mechanism is studied against a rigid barrier [13, 17, 19, 23, 31, 48, 49]. In some of the models, the barrier is even taken as a passive object without any independent dynamics [17, 19, 23]. Inside a cell, actin filaments grow against a cell membrane, which in general have local shape

deformations caused by many different biological processes. Even in *in vitro* experiments, the biological barrier against which actin filaments grow, may have shape fluctuations and other properties, like elasticity, bending rigidity etc. We ask a very general question here: What happens when such a barrier with above properties is placed in the path of growing filaments? How the growth of the filaments are affected by the presence of the such a barrier and what is the effect on the barrier due to the presence of these filaments?

We use simple lattice gas model for the description of our system. In order to study the system numerically, we use kinetic Monte Carlo simulation technique. The filaments are modelled as parallel rigid rods growing upward and pushing the barrier. The barrier is modelled using simple lattice gas modelling, by considering its shape fluctuations and other properties, like elasticity, bending rigidity etc. We first model the barrier by a surface having local shape deformations. An external force is acting on the barrier in a direction opposite to the growth of the filaments. The dynamics of such a barrier can be described by a one-dimensional Kardar-Parisi-Zhang (KPZ) surface. The barrier fluctuates independently and due to the external force, it has a bias in the opposite direction of the filament growth. The filaments, on the other hand, try to push the barrier upward, thereby work against the external force. We further model the barrier by a Solid-On-Solid (SOS) surface considering other properties like elasticity and/or bending rigidity etc. In these cases, the barrier try to remain flat in order to minimize its elastic and/or bending energy and the filaments grow and try to distort the barrier. Thus, in all the cases, there is always a competition between the filament and the barrier dynamics and the dynamics of one is affected by the other.

In all the above cases, we assume that the filaments can always grow and push the barrier, however, another way of modelling the filament barrier interaction is that a filament can only grow when local shape fluctuations of the barrier create a space for the insertion of an actin monomer. In our last chapter, we use both these filament-barrier interactions considering different types of the barrier along with a rigid barrier and note that these two interactions give rise to qualitatively different results.

In chapter 2, we study the force generation by actin filaments growing against a barrier having local shape fluctuations. We model the barrier as a KPZ surface. An external load is acting in the direction opposite to the filament growth. The local shape deformation allow the filaments to grow by making local distortions in the barrier that have less energy cost. Thus, the force generation process is enhanced in the presence of local shape fluctuations of the barrier. Indeed, we note that stall force in this case is comparatively higher that the rigid barrier keeping other conditions same. We also note that the relative time scale between the barrier dynamics and the filament dynamics is very crucial, and the shape of the force velocity curve (convex or concave) changes as this relative time scale changes. The stall force decreases as the barrier dynamics becomes faster than the filament dynamics. The stall

force is also found to depend on the barrier size for single filament, while for N number of filaments, the stall force is independent of system size and scales linearly with N.

In chapter 3, we study the force generation mechanism by actin filaments growing against an elastic barrier. The elastic energy is taken to be proportional to the sum of local height gradients (or the contour length) of the barrier. We note that the average velocity of the barrier shows non-monotonic variation with the elastic constant (μ), with a peak at $\mu = \mu^*$. We note that μ^* is the elasticity where the elastic force of the barrier exactly balances the polymerization force of the filament. Below μ^*, we do not have the steady state and the elastic energy of the barrier increases with time. For an elastic barrier also, we note that the relative time scale plays a crucial role. The shape of elasticity-velocity curve (convex or concave) depends upon this relative time scale. The value of μ^* decreases as the barrier dynamics becomes faster. Within small filament density, μ^* is found to be independent of filament density. However, for high enough filament density, filaments are no longer independent of each other, and μ^* starts decreasing with filament density.

In chapter 4, we study the force generation by actin filaments growing against an elastic membrane, but unlike Chapter 3, the elastic energy is proportional to the square of the local height gradients. The form of the elastic energy directly affects the qualitative nature of the results in the present case. The elastic energy cost, in this case, will increase as the contour length increases, even for very small elasticity. Thus, the system is always in the steady state for any non-zero value of elasticity. The shape of elasticity-velocity curve also depends upon the relative time scale in a similar way as in the previous case.

In chapter 5, We study the force generation by a set of parallel actin filaments growing against a membrane whose energy is described by a Helfrich Hamiltonian. The Hamiltonian contains an elastic energy term, which is proportional to the square of local height gradients and a bending energy term, which is proportional to the square of the Laplacian of height. We note that the shape of the membrane changes qualitatively when we change the value of elasticity (σ) keeping the bending rigidity (κ) fixed at some moderate or large value. This effect gives rise to a non-monotonic variation in the bending energy cost in order to push the membrane. We also note that there is a rich interplay between the elastic and bending energy scales in the system: For large κ and σ, the variation in elastic energy cost in order to push the membrane dominates over the bending energy cost while for large κ but small σ, variation in the bending energy cost dominates. This effect gives rise to non-monotonic variation in the membrane velocity with σ. Starting from a non-zero value at $\sigma = 0$, the velocity first decreases with σ, reaches a minimum, then increases again, reaches a peak, and finally decreases to zero as σ becomes very large. The peak position of the curve (σ^*) shifts towards the smaller elasticity as the bending rigidity is increased. The value of σ^* is independent of filament density or membrane size within small density of filaments, however, for large filament density, σ^* explicitly depends upon the filament density as well as the

size of the membrane. For small κ, the $\sigma - V$ curve is convex and changes to concave when the membrane dynamics becomes faster, however, for large κ, the $\sigma - V$ curves remain non-monotonic and σ^* decreases as the membrane dynamics becomes faster. The $\kappa - V$ curves are monotonic for any value of σ.

In chapter 6, we study the comparison between the two force generation mechanisms, where the filaments barrier interaction have two different forms. In one case, the filament only grows when there are sufficient gap between the filament tip and the barrier while in the other case, the filament is able to grow and push the barrier even if there is no gap between the barrier and the filament tip. We note that this very small difference in the filament barrier interactions gives rise to many qualitative differences between these two processes. Particularly, how the relative time scale between the barrier and the filament dynamics influence the force generation properties, are significantly different for these two cases.

2

ACTIN FILAMENTS GROWING AGAINST A KARDAR-PARISI-ZHANG (KPZ) MEMBRANE

2.1 INTRODUCTION

In this chapter, we study the force generation by parallel actin filaments growing against a barrier having local shape fluctuations. An external force (or load) is applied on the barrier against the direction of filament polymerization. To keep our description simple, we use a lattice gas model and describe the barrier by a Kardar-Parisi-Zhang (KPZ) interface. A KPZ interface is a well studied model for surface height fluctuations in the presence of a field [50–61]. Under the action of this field, the interface tends to move in the direction of the field and thus have a non-zero velocity in this direction. In our model, the direction of this external field (or force) is opposite to the filament polymerization. Since, the barrier can not penetrate the filaments and it has to always stay above the filament tips, it gives rise to a competition between the filament and the barrier dynamics. We are interested to find out how the presence of the fluctuating barrier affects the dynamics of the actin filaments, and how the presence of the filaments affects the shape of the barrier.

Our numerical simulations and analytical calculations show that there is a rich interplay between the polymerization dynamics of the filaments and the shape fluctuations of the barrier. In order to polymerize, the filaments must push against the barrier and work against the external force, either causing a local change in its profile (which requires less energy) or causing a global movement of the whole barrier (which involves a large energy cost). For small and intermediate value of the external force, the barrier motion is governed by its global movement, and for large force, the local fluctuations become important. These local movements cost less energy and can continue even when the force is significantly large. As a result, the stall force in our system is much higher than that for a rigid barrier [17]. For a single filament, the stall force is found to increase with the size of the barrier. For N filaments stall force is independent of the barrier size and scales linearly with N. The barrier shape is also affected by the growing filaments and the scaling behavior of its height profile shows continuous variation as a function of the external load.

There are two time-scales in our system, one associated with the (de)polymerization of the filaments and the other with the thermal fluctuations of the barrier. Our results show that the choice of these time-scales may crucially determine the nature of the force-velocity curve. This is because the local movements of the barrier make increasingly important contribution to its velocity as the thermal fluctuations become faster. Even for small or intermediate load, therefore, the barrier velocity is not governed by its global movement alone and this changes the qualitative nature of dependence of velocity on load. The stall force is also found to decrease for faster barrier dynamics. Some of the results discussed above have been published in [62].

This chapter is organized as follows. In section 2.2, we describe our model. Our results for the single filament and multiple filaments are presented in sections 2.3 and 2.4, respectively, and conclusions are in section 2.5.

2.2 DESCRIPTION OF THE MODEL

The present model consists of N parallel filaments growing against a barrier with a fluctuating height profile (see Fig. 2.1). We model the filaments as rigid polymers, made of rod-like monomers of length d, such that a (de)polymerization event (decreases) increases the length of the filament by an amount d. The barrier is modelled as a one dimensional surface. In our lattice model, the discrete surface elements are represented as lattice bonds of length λ, which can have two possible orientations, $\pm\pi/4$. We denote these two cases by symbols / and \ and call them upslope and downslope bonds, respectively. Height at any particular lattice site i is defined as $h_i = \delta/2 \sum_{j=1}^{i-1} \tan\theta_j$, where θ_j is the orientation of the j-th bond and $\delta = \sqrt{2}\lambda$. The total number of such bonds is L. One / followed by a \ forms a local hill and in the reverse order \/ they form a local valley. The local height of the surface fluctuates due to transition between these hills and valleys. When a local hill (valley) at a given site flips to a valley (hill), the height of that particular site decreases (increases) by an amount δ. We assume δ is equal to the monomer length d in most of our cases. As explained below, this assumption means that height fluctuation of the surface creates a gap which is just enough for insertion of a monomer. Towards the end of the sec 2.3, we briefly discuss the case of $\delta \neq d$. The interface described above has some specific properties, like, the magnitude of the height difference between two consecutive sites remains conserved. The contour length of the interface also remains conserved. This type of simple modelling makes it easier to handle the problem analytically. However, in our later chapters, we will relax these constraints when we consider the elastic or bending energy of the barrier explicitly.

A filament whose tip is in contact with the barrier, is called a bound filament and in absence of any such contact, it is called a free filament. The surface site where a bound

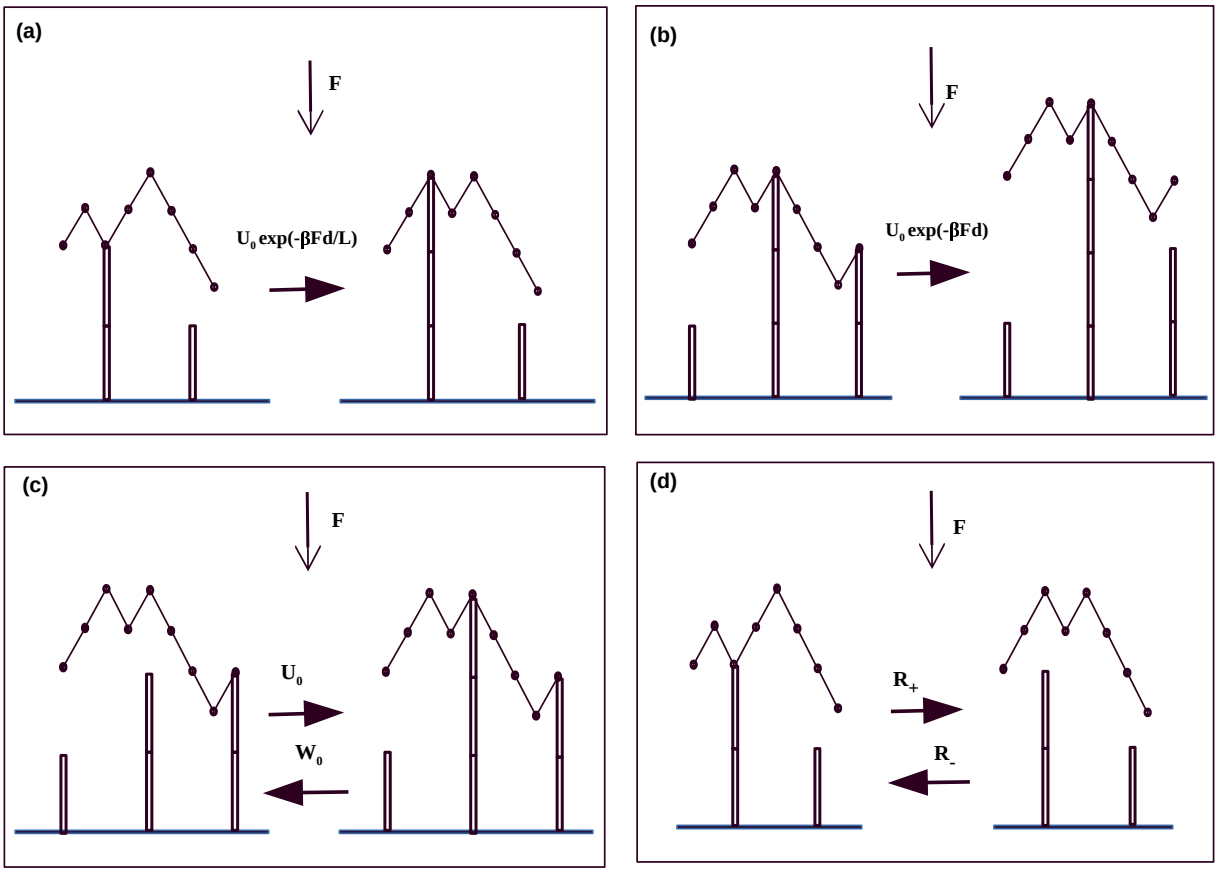

Figure 2.1: Schematic representation of the KPZ barrier model. **(a):** Polymerization of a bound filament by causing a local change in barrier height with rate $U_0 e^{-\frac{\beta F d}{L}}$. **(b):** A bound filament polymerizes by causing global movement of the whole barrier with rate $U_0 e^{-\beta F d}$. **(c):** A free filament polymerizes and depolymerizes with rates U_0 and W_0, respectively. Since these processes do not involve any barrier motion, these rates are independent of F. **(d):** Thermal fluctuation of the barrier: a local valley can flip to a hill with rate R_+ and the reverse process occurs with rate R_-. We use local detailed balance, $R_+/R_- = \exp(-\beta F d/L)$, except at the binding sites, where hill to valley transition may be blocked due to presence of a filament.

filament can form a contact, is called a binding site. When a bound filament polymerizes, it creates space for insertion of another monomer by pushing the barrier up and in this process perform work against the external load (which tends to push the barrier down). When the bound filament pushes against a local valley, that valley flips to a hill and the height of the binding site increases by an amount d [Fig. 2.1(a)]. However, polymerization of a bound filament which is not in contact with a local valley, requires a global movement of the whole barrier as shown in Fig. 2.1(b), when height of all the L sites are increased by an amount d. Assuming F/L is the load per site, the energy cost for the first process is just Fd/L, and for the second process it is Fd. Following the rule of local detailed balance, we assign rates $U_0 exp(-\beta Fd/L)$ and $U_0 exp(-\beta Fd)$ to these two types of polymerization processes, respectively. Here, β is the inverse temperature and U_0 is the free filament polymerization rate that does not involve any barrier movement and hence is independent of F. We also assume the depolymerization rate is same for both free and bound filaments and is denoted as W_0 [see Fig. 2.1(c)]. When a bound filament depolymerizes, it loses contact with the barrier and becomes a free filament. In certain configurations, when there is only one bound filament, its depolymerization results in an unsupported barrier.

Apart from being pushed by the filaments, the barrier can also show thermal fluctuations, when local hills can flip to valleys and vice versa. However, due to presence of the filaments, these transitions can sometimes get blocked. For example, if a bound filament is in contact with a hill, then that particular hill cannot flip to a valley, until the filament depolymerizes and a gap is created for a local downward movement of the barrier. When both forward and reverse transitions are allowed, their rates satisfy local detailed balance $\frac{R_+}{R_-} = e^{-\beta Fd/L}$, where R_+ is the rate at which local surface height can increase (i.e. a valley flips to a hill) and R_- be the reverse transition rate [see Fig. 2.1(d)]. Note that in absence of any external load F, the transition between hills and valleys become symmetric at all sites other than the binding sites and the surface has a local Edwards-Wilkinson dynamics [63]. For non-zero F, hill to valley transitions are generally favored (except, possibly, at the binding site) and the barrier behaves like a KPZ surface with a downward bias.

We perform simulations using kinetic Monte Carlo technique. The relative time scale between the filament dynamics and the barrier dynamics is quantified by a parameter $\mathcal{S}$. For a system consisting of N filaments and L barrier sites, each Monte Carlo time-step consists of N filament updates and $\mathcal{S}$ independent barrier updates. In case of a bound filament polymerization, the barrier heights are also simultaneously updated. More specifically, for $N < \mathcal{S}$, we first choose a filament at random and perform polymerization or depolymerization move as described above. Then we choose $\mathcal{S}/N$ barrier sites in random sequential order and update them. Repeating this process N times completes one Monte Carlo step. Similarly, for $N > \mathcal{S}$, we first perform $N/\mathcal{S}$ filament updates and then choose one barrier site at random

U_0	Free filament polymerization rate	$2.784s^{-1}$
W_0	Filament depolymerization rate	$1.4s^{-1}$
d	Size of an actin monomer	$2.7nm$
T	Temperature	$300K$

Table 2.1: Parameters used in our simulation. The value of parameters U_0 and W_0 are taken from Refs. [1, 64] and the value of d is taken from Refs. [1, 23].

and update it; repeat this process $\mathcal{S}$ times and that defines one Monte Carlo step. We assume periodic boundary condition for the surface and an equal number of upslope and downslope bonds, i.e. no overall tilt. We start with an initial configuration where all N filaments have unit length, containing one monomer each and the upslope and downslope bonds are placed alternatingly (a flat surface). We let the system evolve for a long time, according to above dynamical rules. All our measurements are performed in steady state. The various simulation parameters are given in Table 2.1.

Note that the relative time-scale between the surface and filament dynamics can also be changed by rescaling R_+ and R_-, but we have used $R_- = U_0$ and $R_+ = U_0 e^{-\beta F d/L}$ throughout and controlled the relative time-scale by $\mathcal{S}$ instead.

2.3 RESULTS FOR SINGLE FILAMENT

For a single filament, we first present the results for $\mathcal{S} = L$ and later we consider the effect of variation of $\mathcal{S}$. We define the velocity V of the barrier as the rate of change of the average height of the surface after the system has reached steady state. We present the force-velocity curve in Fig. 2.2(a). This curve has a convex shape where velocity decays rapidly for small force, and for large force it decays slowly. In fact for small and intermediate values of force, the velocity falls off exponentially (Fig. 2.2(a), inset) and close to stalling it shows deviation from the exponential form. We explain below that the exponential dependence originates from the global movement of the barrier [as shown in Fig. 2.1(a)] which dominates V for small and moderate F range. In Fig. 2.2(b) we show the variation of stall force F_s with barrier size L. Stall force increases with L, although logarithmically slowly. Note that stall force is often interpreted as the maximum polymerization force generated by the filament and therefore it is somewhat surprising that it depends on the size of the barrier. This is because, as shown below, in our system the local fluctuations of the barrier, which depend on L, make substantial contribution towards its net velocity and this becomes particularly significant in the stalling regime.

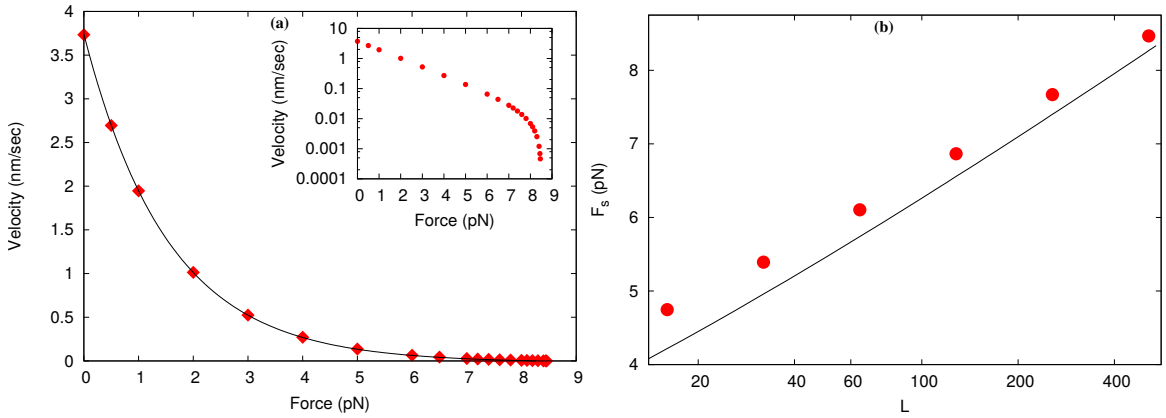

Figure 2.2: Force-velocity characteristic and stall force for a single filament. **(a):** Force-velocity curve has a convex shape. Inset shows exponential decay of the barrier velocity for small and intermediate F, when the global motion of the barrier dominates. Close to stalling the local fluctuations become important. We have used $L = 512$ here. **(b):** Stall force increases with barrier size L. In both the panels, we have used $\mathcal{S}/L = 1$. Discrete points show simulation data and continuous lines show analytical results. Other simulation parameters are as in Table 2.1.

2.3.1 *Analytical calculation of velocity due to global movement*

In our system there are two possible barrier movements: Global and local. In a global movement, a bound filament polymerizes by pushing the whole barrier up, such that the average height changes by an amount d. The rate at which this process happens is $U_0 \exp(-\beta F d)$. Let this process contribute a velocity V_1 to the barrier in steady state, which can be written as

$$V_1 = p_0 d U_0 exp(-\beta F d). \tag{2.1}$$

Here, p_0 is the probability that the filament is in contact with the barrier. Note that here we have ignored the possibility that the bound filament is pushing against a valley (in that case no global movement takes place, only a local flip is sufficient for polymerization). In fact we have verified in our simulation (data presented in Fig. 2.3(b)) that the probability of finding a valley at the binding site is indeed small.

To write V_1 as a function of F we still need to calculate p_0. Define p_i as the probability that the distance between the filament tip and the binding site is i. Clearly, $i = 0$ corresponds to the contact probability. It is easy to see that for $i > 0$, the probability p_i satisfies master equation for a biased random walker:

$$\frac{dp_i}{dt} = W_0 p_{i-1} + U_0 p_{i+1} - (W_0 + U_0) p_i \tag{2.2}$$

and for $i = 0$ one has

$$\frac{dp_0}{dt} = U_0 p_1 - W_0 p_0. \tag{2.3}$$

Here, we have ignored any change in p_i due to height fluctuations at the binding site. For fast barrier dynamics, when height fluctuations increase, this assumption breaks down. In steady state, these equations yield a recursion relation $p_i = \left(\frac{W_0}{U_0}\right)^i p_0$, for positive i. This recursion relation, along with the normalization condition $\sum_i p_i = 1$ yields the expression $p_0 = (1 - W_0/U_0)$, which is independent of F. So the final expression for V_1 becomes

$$V_1 = d(U_0 - W_0)\exp(-\beta F d). \tag{2.4}$$

2.3.2 *Analytical calculation of velocity due to local fluctuations*

To calculate the velocity due to local height fluctuations of the barrier, we consider a local valley (hill) flipping to a hill (valley) which increases (decreases) the average height by an amount d/L. As discussed in section 2.2, the transition rates at the binding site is different from the rest of the system, since a hill to valley transition may be blocked, if a filament is in contact. Then the barrier velocity due to local height fluctuations can be written as

$$V_2 = \frac{dU_0}{L}\left[\left((1+p_0)p_v(0) + \sum_{i=1}^{L-1} p_v(i)\right)e^{-\beta F d/L} - (1-p_0)p_h(0) - \sum_{i=1}^{L-1} p_h(i)\right] \tag{2.5}$$

where $p_v(i)$ and $p_h(i)$ denote the probability to find a valley and a hill, respectively at a distance i from the binding site. In the above equation, the first term on the right-hand-side represents the situation where a valley at the binding site flips to a hill, due to thermal fluctuations or due to being pushed by the filament. The second term presents flipping of a valley to a hill at all the other sites. The third term describe the case when there is a hill at the binding site which can flip to a valley when no filament is in contact. The fourth term describe flipping of a hill to a valley in rest of the system.

The probabilities $p_v(i)$ and $p_h(i)$ can be calculated within a mean field approximation by considering a KPZ surface with the binding site acting as a "defect site", where the transition rates are different from the rest of the system. The shape of the barrier changes due to transition between local hills and valleys. The probability to find a hill at a site s located at a distance i from the binding site is $p_h(i)$ and it can be written as $\rho_i(1-\rho_{i+1})$, where ρ_i is the probability that the bond preceding the site s has $\pi/4$ orientation and the $(1-\rho_{i+1})$ is the probability that the bond immediately after the site s has $-\pi/4$ orientation. Here, we have used mean-field theory and neglected correlation between the bonds. The probability to find a valley at site s can similarly be written as $(1-\rho_i)\rho_{i+1}$. The transition

rate from a hill to a valley is R_- and the reverse process occurs with rate R_+. For $i \neq 0$, $R_+/R_- = \exp(-\beta F d/L)$. However, when $i = 0$, or, in other words, the site s is the binding site itself, then although valley to hill transition is not affected, the reverse transition can take place only when the filament is not in contact with the binding site. We therefore make the simplifying assumption that the effect of the filament can be included by merely rescaling the hill to valley transition rate at the binding site by the probability that the filament is in contact. In section 2.3 we calculate the contact probability $p_0 = 1 - W_0/U_0 \simeq 1/2$. The master equations describing the time-evolution of ρ_i can then be written as

$$\frac{d\rho_i}{dt} = (1-\rho_i)(R_-\rho_{i-1} + R_+\rho_{i+1}) - \rho_i[R_-(1-\rho_{i+1}) + R_+(1-\rho_{i-1})], \qquad \text{for } 2 \leq i \leq L-1 \tag{2.6}$$

and at the binding site,

$$\frac{d\rho_1}{dt} = (1-\rho_1)[R_-(1-p_0)\rho_L + R_+\rho_2] - \rho_1[R_-(1-\rho_2) + R_+\rho_1(1-\rho_L)], \tag{2.7}$$

where we have applied periodic boundary condition, which also gives

$$\frac{d\rho_L}{dt} = (1-\rho_L)(R_-\rho_{L-1} + R_+\rho_1) - \rho_L[R_-(1-\rho_1)(1-p_0) + R_+(1-\rho_{L-1})]. \tag{2.8}$$

We solve the above equations in steady state when the left hand sides vanish. To leading order in $1/L$, we find $\rho_i = a + bi/L$, where a and b are related via the condition $\sum_{i=1}^{L} \rho_i = L/2$ and b satisfies the quadratic equation

$$\left[\frac{\beta F d}{2L} - \frac{p_0}{4}\left(1 - \frac{2}{L}\right)\right] b^2 + \left[1 - \frac{\beta F d}{4L} - \frac{p_0}{2}\left(1 - \frac{1}{L}\right)\right] b + \frac{1}{4}\left(\frac{\beta F d}{L} - p_0\right) = 0, \tag{2.9}$$

one of whose roots can be discarded from the condition that $0 \leq \rho_i \leq 1$ for all i. For a given F, therefore, ρ_i varies linearly with the distance from the binding site with a gradient $1/L$. For $F = 0$, we have $a = (\sqrt{2} - 1)$ and $b = (3 - 2\sqrt{2})$. For $0 \leq F \leq F_s$, the range of variation of a and b are rather small and occur at third or higher decimal places. Therefore, ρ_i does not change significantly with F. Our simulation data in Fig. 2.3(a) show similar qualitative behavior, although close to the binding site there is deviation of ρ_i from linearity. The quantitative values of a and b however, do not match with simulations. We attribute this mismatch to the mean field theoretic assumptions used in our calculation.

We calculate $p_v(i)$ and $p_h(i)$ from ρ_i and compare with simulation in Fig. 2.3(b). Notice that from our analytical expression for ρ_i, it follows immediately that $(p_v(i) - p_h(i))$ is independent of i and $\sim b/L$. This has important consequence for our calculation of V_2. Moreover, the probability that the filament is in contact with a valley is given by $p_v(0)p_0$ and our nu-

merical results in Fig. 2.3(b) show that this probability is rather small. Our calculations also show that $p_v(i)$ and $p_h(i)$ have very weak dependence on F.

Thus, for large L, the total velocity of the barrier $V = V_1 + V_2$ can be written as

$$V(F) = d(U_0 - W_0)\, e^{-\beta F d} + \frac{dU_0}{L}\left[p_v(0)(1+p_0) - (1-p_0)p_h(0) + \sum_{i=1}^{L-1}\{p_v(i)(1-\frac{\beta d F}{L}) - p_h(i)\}\right] \tag{2.10}$$

where we have retained terms upto order $1/L$ and ignored higher order terms. In Fig. 2.2(a) we compare our calculation with simulation results and obtain reasonably good agreement. For small F, the first term in Eq. 2.10 dominates the velocity and as F increases, local fluctuations become more important. The last term in Eq. 2.10, within the braces, which represents the velocity due to hill-valley fluctuations at all sites, except the binding site, is the most dominant term in the local movement. In the stalling region, the positive contribution from the global movement and the negative contribution from the local fluctuations cancel each other, where the first and last term of Eq. 2.10 determine the major balance. The stall force F_s can be obtained by graphically solving the above transcendental equation after putting its left hand side zero. This gives stall force as a function of L and we compare this variation with simulation results in Fig. 2.2(b). We find good agreement for large L but as expected, for small L there are deviations. Note that the stall force in our system is substantially higher than that for a rigid barrier [17]. Since the local movements cost much less energy, they can continue even when the load is high.

2.3.3 *Variation of the shape of the barrier with load*

We have seen above how the barrier fluctuations affect the growth of the filament. The barrier properties are also altered in this process. As the load increases, the height profile of the barrier shows larger variation across the system. We characterize it by measuring the scaling of average height with distance from the binding site: $\langle h(r) - h(0)\rangle \sim r^{\alpha}$, where $h(r)$ is the height of a site at a distance r from the binding site. In Fig. 2.4 we plot α as a function of the external force, which shows that for small force α increases slowly, around the stalling force there is a sharp increase and finally for very large force, α saturates to unity. Note that large value of α indicates presence of large hills and valleys in the system. $\alpha = 1$ corresponds to a phase separation of upslope and downslope bonds in the system which gives rise to one single large hill, the highest point being the binding site. This situation is similar to the case of an elastic membrane, when the membrane tension is large and the membrane is stretched completely. Note that our analytical calculation of the density profile gives, $\langle h(r) - h(0)\rangle \sim$

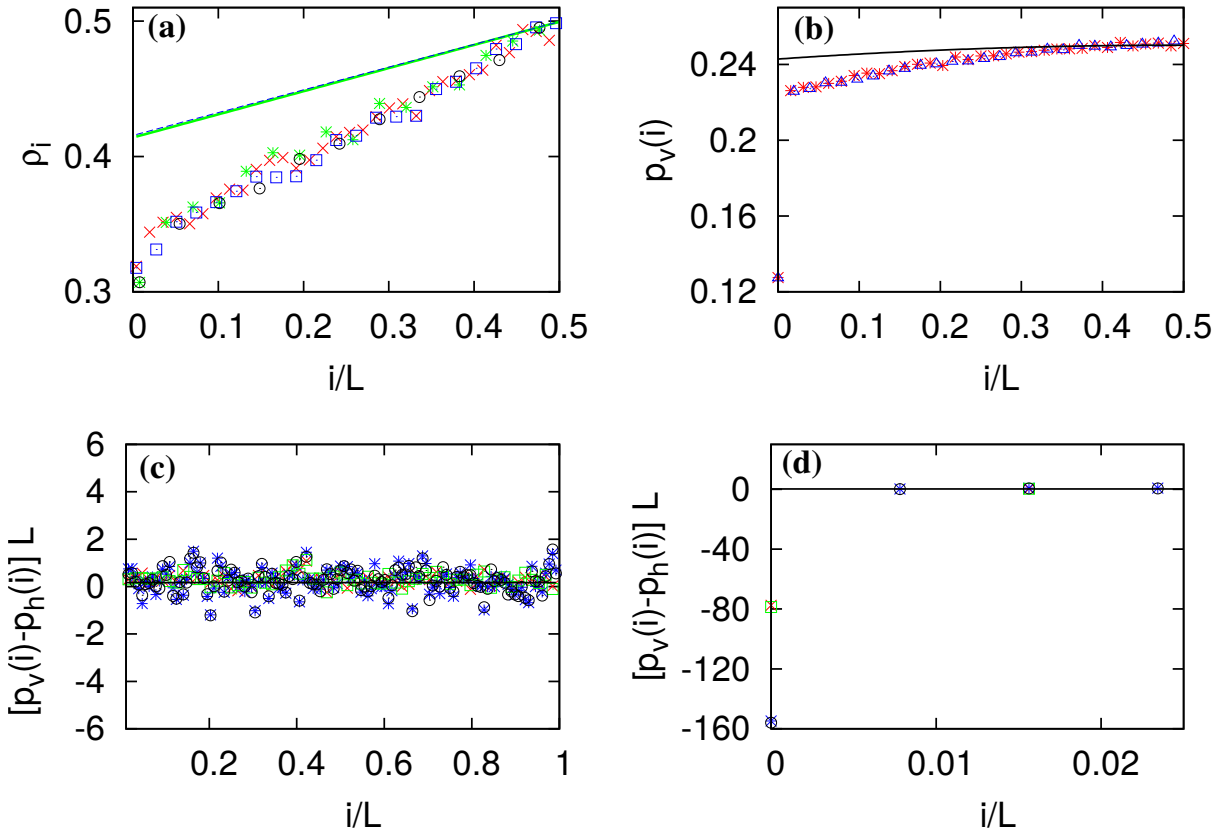

Figure 2.3: Average shape of the barrier for single filament. Discrete points show simulation results and continuous lines show analytical prediction. **(a):** Probability ρ_i to find an upslope bond as a function of scaled distance i/L from the binding site. $\rho_i = 1/2$ for $i = L/2$ and for larger i, we have $\rho_i = 1 - \rho_{i-L/2}$. The open symbols correspond to $F = 0$ and the close symbols correspond to $F = 4pN$. Symbols $*$ and $\circ$ are for $L = 128$ and $\times$ and $\square$ are for $L = 256$. These data show that, except close to the binding site, ρ_i increases linearly with i with a gradient $\sim 1/L$. We also find that ρ_i remains almost same for these F values. The continuous lines are analytical predictions, where green solid line is for $F = 0$ and blue dashed line is for $F = 4pN$. **(b):** Probability $p_v(i)$ to find a valley at a distance i from the binding site. For $i = 0$ the probability is substantially smaller compared to the rest of the system, which means it is rather unlikely to find a valley at the binding site. The symbols $*$ and Δ represent $F = 0pN$ and $4pN$, respectively. We have used $L = 512$ here. **(c) and (d):** $[p_v(i) - p_h(i)]$ shows a sharp jump at $i = 0$ and then remains constant at a value that scales as $1/L$. The open symbols correspond to $F = 0$ and the closed symbols correspond to $F = 4pN$. Symbols $*$ and $\circ$ are for $L = 256$ and $\times$ are $\square$ are for $L = 512$. Other simulation parameters are as in Table 2.1.

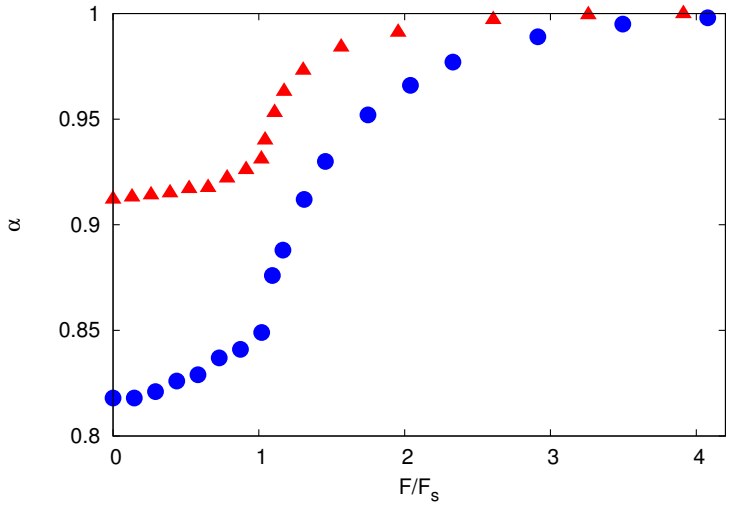

Figure 2.4: Variation of α as a function of external load. Close to the stalling force, α shows a sharp increase. Here, we have used $S/L = 1$ and $L = 256$ (red triangle) and 128 (blue circle). Other simulation parameters are as in Table 2.1.

$\frac{b}{2L}r^2 + (\frac{b}{2L} + a)r$, which in the limit of large L gives, $\alpha = 1$. In this case, we do not have any F dependency in α, as we have neglected the F-dependency in the calculation of ρ_i.

2.3.4 *Effect of faster and slower barrier dynamics*

We find the nature of the force-velocity curve depends on the relative time-scale of the barrier and filament dynamics. For faster barrier dynamics, the local fluctuations of the barrier increases and as a result their contribution to the net velocity is also higher. This means even for small force, the velocity is not dominated by the global movement (first term in Eq. 2.10) alone. In addition, our simple expression for the contact probability $p_0 = (1 - W_0/U_0)$, which was derived neglecting the local fluctuations at the binding site, does not remain valid for fast barrier dynamics and p_0 increases with F in this case (see our data in Fig. 2.5). As a result, the velocity does not decay exponentially for small force, but follows a slower decay. For a given F, as the barrier dynamics becomes faster, the velocity becomes higher and the convex nature of the curve is gradually lost. Moreover, since stalling phenomenon in our system can be described as a balance between global and local velocity of the barrier (see Eq. 2.10), larger contribution from local movement implies this balance is reached at a smaller value of force. Therefore, for faster barrier dynamics we have a smaller stall force. We present our data in Figs. 2.6(a) and 2.6(b).

Our data in Fig. 2.6(b) imply that in the limit of infinitely slow barrier dynamics, when the barrier can be considered as an effectively rigid object, the stall force diverges. Note that even in this limit, our model remains different from the rigid barrier case studied in [17], where

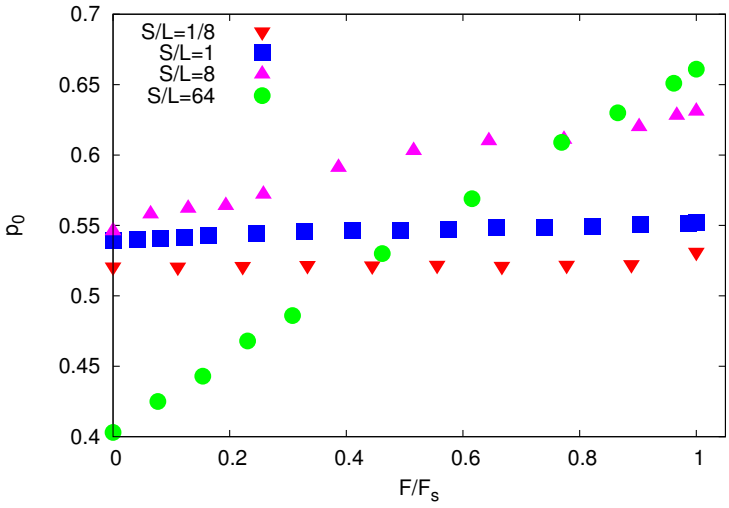

Figure 2.5: Contact probability p_0 as a function of F for single filament. Our analytical calculation yields $p_0 = (1 - W_0/U_0) \simeq 0.5$. For slow barrier dynamics, we find reasonable agreement. But for fast barrier dynamics, our analytical prediction does not remain valid any more and p_0 increases with F. Here we take L=64. All other simulation parameters are as in table 2.1.

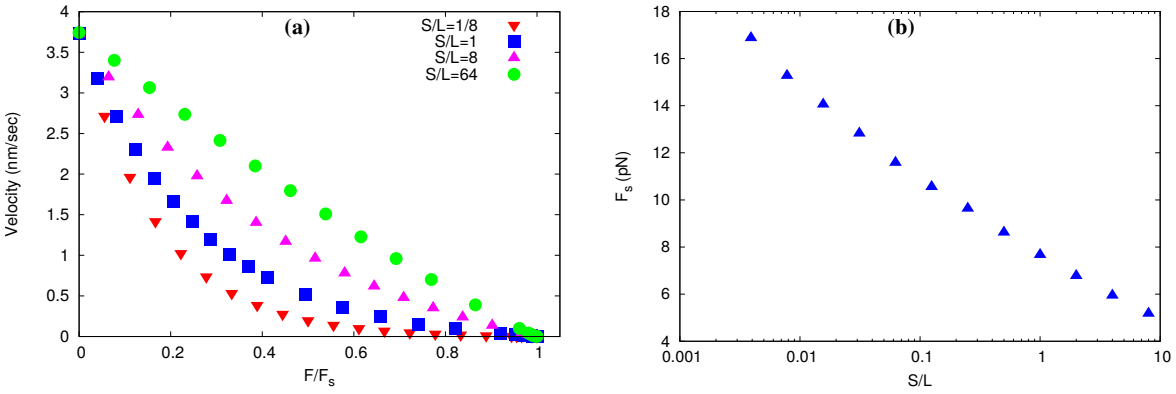

Figure 2.6: Force-velocity characteristic for a single filament depends on the relative time-scale between the filament and barrier dynamics. **(a):** Velocity of the barrier vs scaled force for different values of $\mathcal{S}/L$. For large $\mathcal{S}/L$, the convex nature of force-velocity characteristic is lost. As $\mathcal{S}/L$ increases, the local fluctuations of the barrier become more important and even for small F, the barrier velocity is not governed by the global movement alone, and hence V does not decay exponentially anymore. Here, we have used $L = 64$. **(b):** Stall force decreases as a function of $\mathcal{S}/L$. Since local movements of the barrier become more important for large $\mathcal{S}/L$, the balance between global and local movements is reached at a smaller force. Note however, that the x-axis is plotted in a log-scale, indicating a weak dependence of stall force on the time-scale. Here we have used $L = 256$. Other simulation parameters are as in Table 2.1.

at least one filament is always bound to the barrier. For $N = 1$ this would mean whenever there is a depolymerization, the barrier also moves down, along with the filament tip. On the contrary, we allow unsupported barrier in our system and when the barrier is effectively rigid, it shows only global movement which is always in the upward direction. The force velocity curve is perfectly exponential in this case and zero velocity is reached at $F \to \infty$ limit.

2.3.5 *Results for $\delta < d$*

Throughout this section, we have considered the case where δ, the barrier fluctuation length scale is equal to the monomer length d, i.e., the local movement of the barrier occur in steps whose size is equal to that of a monomer. In this section, we show the results for $\delta < d$ for single filament. The force velocity curve for different values of d/δ is shown in Fig. 2.7(a). We note that the curves are convex even for much smaller values of δ. For small values of F, the points collapse with each other, as for small F, only the global movement plays significant role which is independent of the value d/δ, and the local fluctuations are negligible. On the other hand, for large F, the velocity for smaller δ stalls at larger forces. This is because for small value of δ, the local fluctuations are less costly and near the stalling regime, these local fluctuations make significant contributions in the velocity. We explicitly show the variation of F_s as a function of d/δ in the inset of Fig. 2.7(a) and note that F_s increases as $(d/\delta)^{0.6}$. We also note that the relative time-scale between the filament and barrier dynamics affects the $F - V$ curve in the same way as for $d = \delta$ case [Fig. 2.7(b)]. The stall force continues to show dependence on the barrier properties [inset Fig. 2.7(b)]. Thus, we can say that the qualitative conclusions of our earlier results also remain valid for $\delta < d$. In other words, even when the shape fluctuations of the barrier occur over much smaller length scales, their effect cannot be ignored.

2.4 RESULTS FOR MULTIPLE FILAMENTS

In the case of N filaments in the system, we mainly consider the case when the ratio N/L is small. We assume the binding sites are uniformly placed on the lattice, at a distance L/N. Between the segment of two successive binding sites, the same considerations as in a single filament case apply. We assume these segments are independent and apply our results for the single filament case for each segment.

To start with, we consider the velocity of the barrier due to its global movement $V_1 = p_0 N d U_0 \exp(-\beta F d)$. As before, p_0 is the probability to find a filament in contact with the barrier and $p_0 N$ is the average number of bound filaments in the system. Here, we have

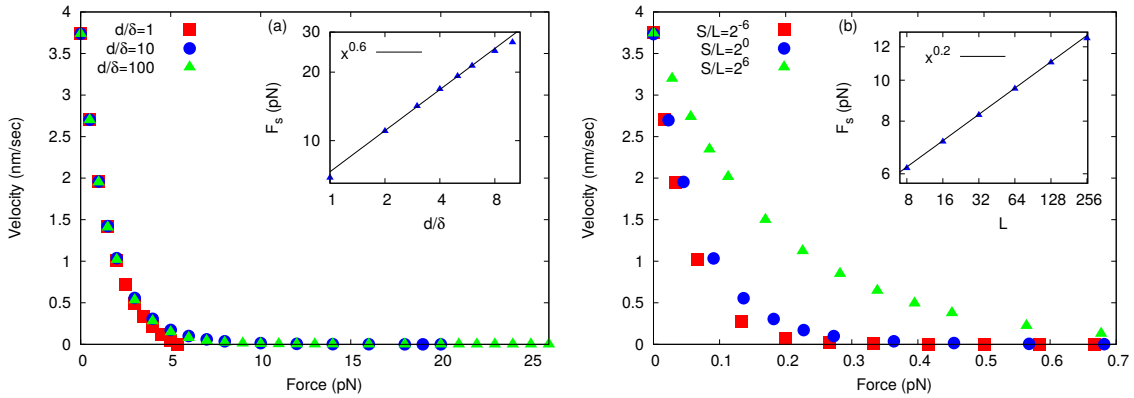

Figure 2.7: Results for $\delta < d$. **(a):** The force velocity curves are convex even for $d/\delta >> 1$. For small F, the points collapses with each other, as in this regime, only the global movements play significant role and the local fluctuations are negligible. **Inset (a):** The stall force increases as $(d/\delta)^{0.6}$, this is because for small δ, the local fluctuations becomes less costly and near the stalling regime, these local fluctuations maintains the velocity of the barrier. Here we use $L = 32$ and $\mathcal{S}/L = 1$. **(b):** The shape of the force velocity curve changes as $\mathcal{S}/L$ changes. **Inset (b):** The stall force increases as $L^{0.2}$. For the inset, we use $L = 64$ and $d/\delta = 2$. Other simulation parameters are as in Table 2.1.

neglected any correlation between the binding sites. To calculate p_0, we write down master equations for average number N_i of filaments at a distance i from the corresponding binding site. By definition, N_0 is the average number of bound filaments and the contact probability is $p_0 = N_0/N$. The time-evolution equations for N_i can be written as

$$\frac{dN_0}{dt} = U_0 N_1 - \{(N_0 - 1)U_0 e^{-\beta F d} + W_0\}N_0 \tag{2.11}$$

$$\frac{dN_1}{dt} = \{(N_0 - 1)U_0 e^{-\beta F d} + W_0\}N_0 + U_0 N_2 - (N_0 U_0 e^{-\beta F d} + W_0 + U_0)N_1 \tag{2.12}$$

$$\frac{dN_i}{dt} = (N_0 U_0 e^{-\beta F d} + W_0)N_{i-1} + U_0 N_{i+1} - (N_0 U_0 e^{-\beta F d} + W_0 + U_0)N_i \quad \text{for } i \geq 2 \tag{2.13}$$

Here, we have assumed that the distance i between the filament tip and the binding site can change only due to polymerization and depolymerization dynamics and the global movement of the whole barrier due to polymerization of bound filaments. We have neglected local height fluctuations occurring at the binding sites. As we show below, this approximation works reasonably well as long as filament density N/L is small and the time-scale of barrier fluctuation is comparable or slower than the filament dynamics. For very fast motion of the barrier, the height fluctuations at the binding sites become more frequent and this assumption breaks down.

Solving the Eqs. 2.11, 2.12, 2.13 in steady state, we obtain the recursion relation

$$N_{i+1} = \left(\frac{N_0 U_0 e^{-\beta F d} + W_0}{U_0}\right)^i N_1; \; i = 1, 2, \ldots \tag{2.14}$$

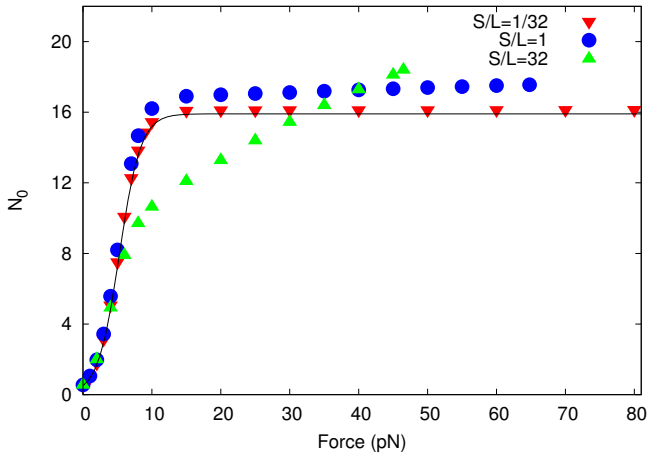

Figure 2.8: Average number of bound filaments N_0 as a function of force F. For slow barrier dynamics, our analytical prediction in Eq. 2.16 agree well with numerics. But as the barrier dynamics becomes faster, deviations are observed. Here we have used $L = 256$, $N = 32$. Other simulation parameters are same as in Table 2.1.

and

$$N_1 = \frac{(N_0 U_0 e^{-\beta F d} + W_0 - U_0 e^{-\beta F d})}{U_0} N_0 \tag{2.15}$$

Using the normalization relation, $\sum N_i = N$ we get

$$N_0 = \frac{N(U_0 - W_0)}{U_0 - U_0 e^{-\beta F d} + N U_0 e^{-\beta F d}} \tag{2.16}$$

and the contact probability has the form $p_0 = \frac{(U_0 - W_0)}{U_0 + (N-1) U_0 e^{-\beta F d}}$. In Fig. 2.8 we compare this result with simulation and find reasonable agreement. For small F, the contact probability is approximately $1/N$ times the single-filament value, indicating that for small F, at most one filament is in contact with the barrier.

For the local movement of the barrier, we need to calculate the probability to find hills and valleys. As discussed above, for each segment between two successive binding sites, we use our results for $p_v(i)$ and $p_h(i)$ for the single filament case (with the modification that i in this case varies from 0 to $(L/N - 1)$). The velocity due to local fluctuations then becomes

$$V_2 = \frac{N d U_0}{L} \left[\left(p_v(0)(1 + p_0) + \sum_{i=1}^{L/N-1} p_v(i) \right) e^{-\beta F d/L} - (1 - p_0) p_h(0) - \sum_{i=1}^{L/N-1} p_h(i) \right] \tag{2.17}$$

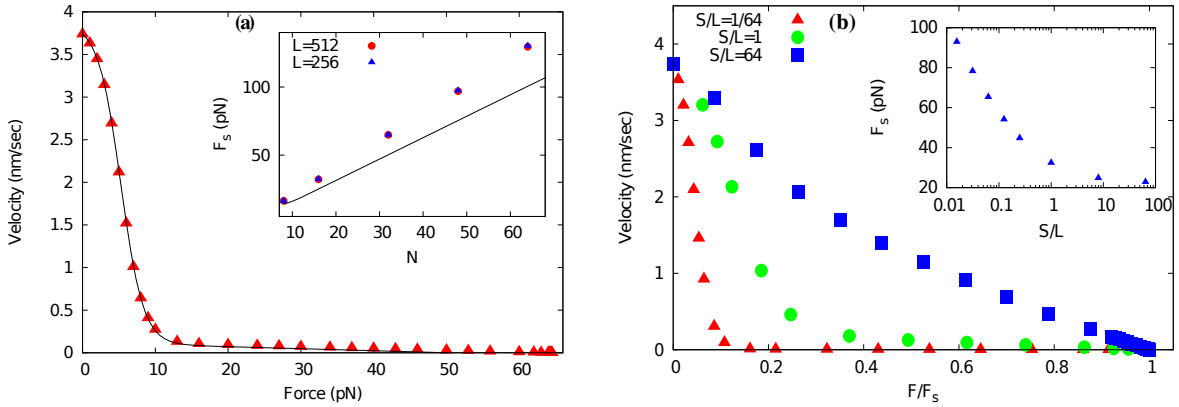

Figure 2.9: Force-velocity characteristic for multiple filaments. **(a):** Velocity shows very slow decay for large F, when global movement can be neglected and V can be assumed to be governed by local fluctuations alone. Here, we have used $L = 512$ and $N = 32$. Inset shows stall force as a function of N for two different L values. We find stall force scales linearly with N and remains independent of L. The continuous lines show analytical results. **(b):** Dependence of force-velocity characteristic on the time-scale of barrier dynamics. In this case we find same qualitative effect as in the single filament case. Here, we have used $N = 16$ and $L = 128$. Other simulation parameters are as in Table 2.1.

The total velocity to leading order in $1/L$ and N/L becomes

$$V(F) = \frac{d(U_0 - W_0)}{1 + (N-1)e^{-\beta F d}} N\, e^{-\beta F d} + \frac{dU_0 N}{L}\Big[\{p_v(0)(1+p_0) - p_h(0)(1-p_0)\} + \sum_{i=1}^{L/N-1}\Big\{p_v(i)\Big(1 - \frac{\beta F d}{L}\Big) - p_h(i)\Big\}\Big] \tag{2.18}$$

The stall force can be obtained by solving the above transcendental equation graphically for $V(F) = 0$ and we compare the analytical stall force with our simulation results in Fig. 2.9(a), inset. We find that the stall force is independent of L in this case and scales with N, which can be easily seen from Eq. 2.18. Since the value of the stall force is rather large in this case, one can neglect global movement of the barrier close to the stalling regime. In addition, $p_0 \approx (1 - W_0/U_0)$ for large force, and $(p_v(i) - p_h(i))$ is of order N/L. Using these in Eq. 2.18 it directly follows that the stall force for N filaments is independent of L and scales as N. We also investigate the effect of barrier movement time-scale on the force-velocity dependence [Fig. 2.9(b)] and we find qualitatively the same effect as in $N = 1$ case.

2.5 SUMMARY

In this chapter, we have studied force generation by a set of parallel actin filaments polymerizing against a barrier. A similar question has been addressed in many recent works where the barrier was modelled as a rigid wall, which may have a thermal ratchet like motion [13, 14, 65, 66], or may be a passive obstacle which can move only when pushed by the filaments

[17, 19, 23, 67–69]. In this chapter, we have considered a barrier with thermal fluctuations but instead of modelling it as a rigid wall, we allow for its shape fluctuations. Interestingly, we note that the qualitative shape of the F-V curve depends upon the relative time-scale between the filament polymerization and barrier fluctuation. For slow barrier dynamics, the curve has a convex shape and V shows an exponential decay for small and moderate F. But for fast barrier dynamics when the local fluctuations become more important, there is significant deviation from exponential dependence. In experimental and theoretical literatures also, the qualitative nature of the force-velocity curve was found to depend on the details of the experimental set-up or the modelling details as described in chapter 1 [7–10, 13, 14, 17, 19]. Certain theoretical models even showed a crossover from convex to concave force-velocity curve, as some model parameters are varied [23, 30, 31]. A similar effect is seen in [30] also, for a hybrid mesoscopic model, that combines the microscopic dynamics of semi-flexible actin filaments and the viscous retrograde flow of actin network modelled as a macroscopic gel. It was shown that the force-velocity curve can be both convex and concave, depending on the characteristic time-scale of recoil of the gel-like network. It is remarkable that our simple lattice gas model can reproduce this same effect, which underlines the importance of the relative time-scale of obstacle and filament dynamics on the force generation mechanism.

Finally, our simple model shows that a non-rigid obstacle can produce remarkable effects on force generation of parallel actin filaments. Our results underline the importance of the local shape distortions and the independent dynamics of an obstacle. Many of our conclusions are generic and can be expected to remain valid in systems where different descriptions of a non-rigid obstacle are used. This also opens up the possibility of observing some of these effects in experiment. For example, the change of shape of the barrier with external load can be monitored in an experiment and our prediction that the height variation across the barrier increases with load, can be explicitly verified. The key feature of a fluctuating barrier is that one component of velocity comes from the local fluctuations and a direct measurement of this component will surely give insights into the effects of barrier fluctuations. Our model shows that for multiple filaments close to stalling regime, velocity is dominated by these local movements and we also predict the scaling behavior of this velocity with filament density and barrier size. It would be interesting to verify these predictions in experiments, which would not only shed light on the qualitative nature of the local fluctuations but would also provide insights about their quantitative behavior.

3

ACTIN FILAMENTS GROWING AGAINST AN ELASTIC MEMBRANE: GRADIENT MODEL

3.1 INTRODUCTION

The plasma membrane is elastically deformable and has a role of central importance in the motility process [34–37]. Extension of the plasma membrane that takes place during cell motility and cell spreading depends strongly on membrane tension. The lamellopodial extension rate increases (decreases) when the membrane tension is decreased (increased) [39]. A flexible membrane enhances formation of filopodial protrusion and also allows merging of smaller neighboring protrusions into a larger one [24]. Thus, elastic properties of the plasma membrane have significant influence on actin polymerization and force generation process. This gives rise to a more general theoretical question: What happens when a flexible, elastically deformable obstacle is placed in the path of growing filaments? In this chapter, we focus on this aspect, and study the force generation by actin filaments growing against an elastically deformable barrier. The elastic energy of the membrane is taken to be proportional to its contour length. Due to this elastic energy, the membrane tries to stay flat and any deformation from this flat state costs energy. The filaments, on the other hand, push the membrane and try to deform it. Thus, similar to Chapter 2, in this case also there is a competition between the dynamics of the filaments and the barrier. We are interested to find out how the membrane elasticity affects the growth of the filaments and how the polymerization force exerted by the filaments affects the membrane deformations.

We find that the average membrane velocity shows a peak as a function of the membrane tension μ. This is somewhat surprising since a larger membrane tension is expected to make the polymerization process more costly and hence the growth process slower. We show that the peak results from the competition between the polymerization force of the filaments and the elastic force of the membrane. We also show that for small μ, the system does not have a steady state and the total contour length of the membrane keeps increasing with time. For large values of μ, the system reaches a steady state and the membrane velocity then decreases with μ. The relative time-scale between the filament and the membrane dynamics plays very

crucial role to determine the qualitative shape of the elasticity-velocity curve. Some of the results discussed above have been published in [70].

This chapter is organized as follows. In section 3.2, we describe our model. Our results for the single filament and multiple filaments are presented in sections 3.3 and 3.4, respectively, and conclusions are in section 3.5.

3.2 DESCRIPTION OF THE MODEL

The present system consists of a set of N parallel filaments growing against an elastic membrane as shown in Fig. 3.1. The membrane is modelled as a one dimensional lattice of length L and lattice constant d. At each site i of the lattice a height h_i is assigned. For a completely flat membrane, when height of all sites are the same, the elastic energy is minimum. Presence of a local height gradient stretches the membrane and costs energy.

The membrane is modelled as a solid-on-solid (SOS) surface without diffusion [71] and the Hamiltonian has the form [25, 72–74]

$$\mathcal{H}_1 = \mu \sum_{i=1}^{L} |h_i - h_{i+1}| \tag{3.1}$$

where μ is the elastic tension. In the absence of any filament, the membrane undergoes equilibrium thermal fluctuations and the probability to obtain a particular height profile $\{h_i\}$ follows Boltzmann measure with the above Hamiltonian. The sum in Eq. (3.1) is related to the total contour length $\mathcal{C}$ of the particular height configuration of the membrane, such that $\mathcal{C} = \sum_{i=1}^{L} |h_i - h_{i+1}| + Ld$. Note that since the energy is linear in $\mathcal{C}$, the energy cost for increasing the contour length by an amount δ just depends on δ and is independent of $\mathcal{C}$. We call Eq. (3.1) the "gradient model". We assume periodic boundary condition on the membrane, $h_{L+1} = h_1$. This model was used in Ref. [72] to study thermally excited protrusions in lipid membranes. In Ref. [73], the critical behavior of this model was analysed using functional renormalization. In Ref. [25], this model was used to describe a membrane and scaling properties of the height fluctuations were studied when the membrane was driven by an advancing uncorrelated front representing the actin meshwork. In our next chapter, we will also consider the case where the elastic energy of the barrier is proportional to the square of local height gradients [26, 73].

The membrane can undergo independent thermal fluctuations in its local height [see Figs. 3.1(a) and 3.1(b)] and tends to minimize its elastic energy. In our lattice model, we assume that as a result of these fluctuations, the local height can increase or decrease by a discrete

amount δ. The rates of the dynamical moves that changes the energy by an amount $\triangle E$ are assumed to satisfy local detailed balance

$$\frac{R_+}{R_-} = e^{-\beta \Delta E} \tag{3.2}$$

where R_+ (R_-) is the rate of those processes that increases (decreases) the energy by an amount ΔE [Fig. 3.1a]. For $\Delta E = 0$, the rate is taken to be unity [Fig. 3.1b]. Unlike the previous case (Chapter 2), here the height of a membrane site can fluctuate without any restriction, such that the height difference between two neighboring site may be greater than unity or even zero. Thus, in this case, the contour length of the barrier is no more conserved.

The filaments are modelled in a similar way as in the Chapter 2. A (de)polymerization event increases (decreases) the length of a filament by an amount d. Throughout this work, we consider δ, the unit of barrier height fluctuation, and the monomer size d to be the same. There are two types of filaments we need to consider: free filaments, which are not in touch with the membrane, and bound filaments, whose tip is in contact with a membrane site. The point of contact is called the binding site. For a free filament, the polymerization process happens with a rate U_0 and depolymerization happens with a rate W_0 [see Fig. 3.1(d)]. However, for a bound filament, a polymerization process increases the height of the binding site by an amount d [see Fig. 3.1(c)] and hence an energy cost ΔE is involved. Note that the change in energy can be positive or negative, or even zero, depending on the local height configuration around the binding site. For a positive (negative) energy cost, the bound filament polymerization rate is taken to be $U_0 R_+$ ($U_0 R_-$), while for zero energy cost, the rate is simply U_0. The depolymerization rate of bound filament does not involve any membrane movement and hence is equal to W_0.

The elastic interaction of the membrane tends to keep the membrane flat and the bound filaments generally grow by causing protrusions in the membrane. Although in principle, it is possible that the local height configuration around the binding site is such that the polymerization of bound filament actually releases some elastic energy, such configurations are rare and most of the time elastic force acts against polymerization force. The elasticity-velocity curve therefore plays a similar role as the force-velocity curve measured in Chapter 2 and in many other studies [7–10, 13, 23, 31, 62].

Note that the height of the membrane at the binding sites should be such that the membrane always stays above the filament tips, and this puts some restrictions in height fluctuations at the binding sites. Any height fluctuation that brings a binding site at a lower height than the filament tip is forbidden. Everywhere else in the membrane, the height fluctuations will occur in accordance with Eq. (3.2).

We perform simulations using kinetic Monte Carlo technique as discussed at the end of model section of chapter 2. We start with an initial configuration where all N filaments have

unit length, containing one monomer each and a flat membrane. The system undergoes time evolution and after a large number of Monte Carlo steps, we perform our measurements.

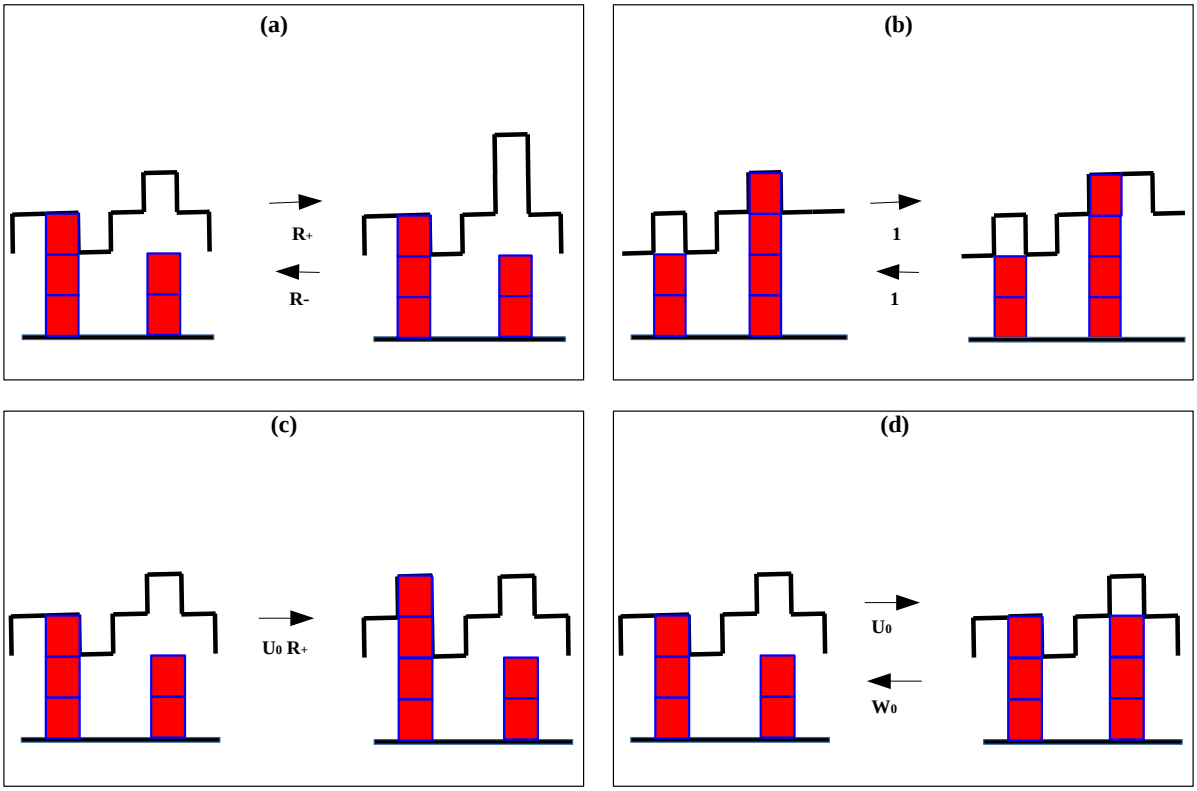

Figure 3.1: Schematic representation of gradient model. The square blocks show actin monomers, which join together to form rod-like filaments. The thick solid line represents the shape of the elastic membrane. **(a):** A bulk site of the membrane thermally fluctuates and changes its height by an amount d, which in turn changes the membrane contour length by $2d$. The forward process increases the energy and occur with rate R_+ while the reverse process decreases the energy and happens with rate R_-. **(b):** A bulk site of the membrane changes its height by an amount d but the energy remains same and thus the movement happens with rate unity. **(c):** A bound filament pushes the binding site by an amount d that costs energy and occurs with rate $U_0 R_+$. **(d):** A free filament polymerizes (depolymerizes) with rate U_0 (W_0).

3.3 RESULTS FOR SINGLE FILAMENT

In the present model, since the elastic energy of the membrane is proportional to its contour length, the change in local height by an amount d that causes $\mathcal{C}$ to change by $2d$, brings about a change $2\mu d$ in the energy. In our simulation, we choose $R_+ = e^{-\beta\mu d}$ and $R_- = e^{\beta\mu d}$. The bound filament polymerization that leads to an increase (decrease) in energy happens with rate $U_0 R_+$ ($U_0 R_-$). All other movements of the membrane where energy does not change, occur with rate unity. We first present the results for $\mathcal{S}/L = 1$.

3.3.1 *Peak in the elasticity-velocity curve*

The polymerization of the bound filament pushes the membrane upward and gives rise to a nonzero membrane velocity, which is measured as the rate of change of the average membrane height in the long time limit. We measure the velocity V as a function of μ and present our data in Fig. 3.2(a), for $\mathcal{S}/L = 1$. We find that V shows a nonmonotonic dependence on μ: Starting from a nonzero value for $\mu = 0$, it increases with μ for small μ values, and after reaching a peak at a certain μ^*, the velocity decreases again. Presence of a peak is somewhat surprising, since increasing μ ought to make it more difficult for the filament to push against the membrane. We also find that V scales as $1/L$. In the remaining part of this sub-section, we explain different aspects of this data in detail.

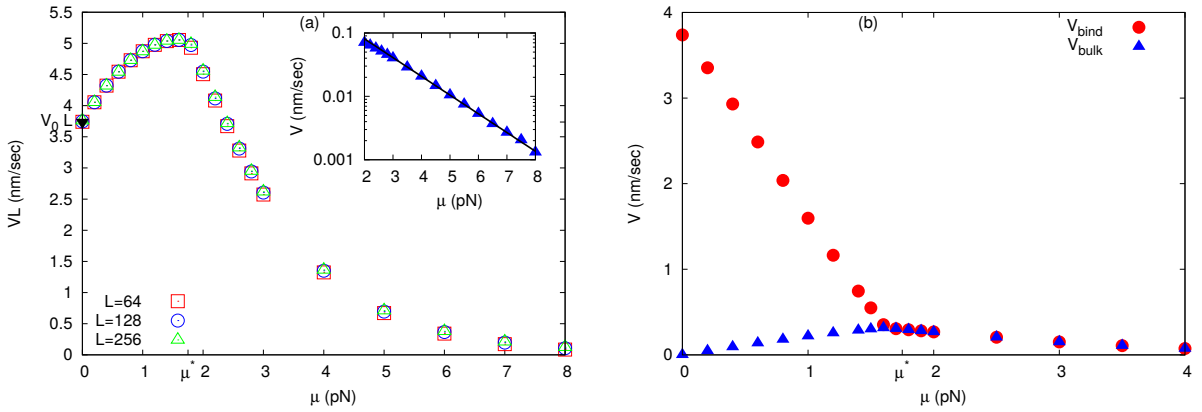

Figure 3.2: $\mu - V$ curve for a single filament. **(a):** The average velocity of the membrane as a function of μ shows a peak at μ^*. While $V \sim 1/L$, the peak-position μ^* does not depend on L. The solid triangle on the y-axis marks $V_0 = \frac{d}{L}(U_0 - W_0)$, which is the expected value of V at $\mu = 0$. **Inset:** For large μ, the membrane velocity decreases exponentially with a decay constant $\simeq 0.67$, which is close to the value of βd. Here, we have used $L = 64$. **(b):** The variation of average velocity of the binding site (V_{bind}) and the average velocity of a bulk site (V_{bulk}) with μ, shows that V_{bind} decreases monotonically with μ while V_{bulk} increases with μ for $\mu < \mu^*$. For $\mu > \mu^*$, these two velocities are equal. Here we have used $L = 16$. For all the above plots, we have used $\mathcal{S}/L = 1$. Other simulation parameters are as in Table 2.1.

First we consider $\mu = 0$. In this case, there is no energy cost involved in stretching the membrane, and thus the single filament present in the system polymerizes with rate U_0, irrespective of whether it is free or bound to the membrane. The velocity of the barrier in this case turns out to be $V_0 = d(U_0 - W_0)/L$. We briefly present the calculation below.

Let p_0 be the probability that the filament is in the bound state. The height at the binding site can (a) increase due to bound filament polymerization that happens with an effective rate $U_0 p_0$, (b) increase due to thermal fluctuation that happens with rate 1, or (c) decrease due to thermal fluctuation, provided the filament is not in a bound state (since the membrane always needs to stay above the filament tip) and this process happens with effective rate

$(1-p_0)$. It follows therefore that the average velocity of the membrane can be written as $V_0 = V(\mu = 0) = \frac{d}{L} p_0 (U_0 + 1)$, where the pre-factor d/L is the change in average height of the membrane due to d-unit change in the binding site height. Here, we have assumed $\mathcal{S}/L = 1$. The contact probability p_0 can be calculated by noting that the height difference between the filament tip and the binding site performs a biased random walk, with the restriction that it cannot cross the origin and become negative [62].

Let p_i be the probability that there is a gap of size i between the binding site and the filament tip. Clearly, the contact probability p_0 corresponds to $i = 0$. The master equation for p_i with $\mu < \mu^*$ can be written as

$$\frac{dp_i}{dt} = (U_0 + \frac{\mathcal{S}}{L} e^{\beta\mu d}) p_{i+1} + (W_0 + \frac{\mathcal{S}}{L} e^{-\beta\mu d}) p_{i-1} - (U_0 + \frac{\mathcal{S}}{L} e^{\beta\mu d} + \frac{\mathcal{S}}{L} e^{-\beta\mu d} + W_0) p_i; \quad for\ i > 0$$

and

$$\frac{dp_0}{dt} = (U_0 + \frac{\mathcal{S}}{L} e^{\beta\mu d}) p_1 - (\frac{\mathcal{S}}{L} e^{-\beta\mu d} + W_0) p_0; \quad for\ i = 0$$

where all symbols have their usual meaning. Here, we have used the fact that for $\mu < \mu^*$, the binding site moves faster than the rest of the system and hence has a larger height than all bulk sites. Although the system is not in steady state for $\mu < \mu^*$, the probability p_i still reaches a stationary value. In steady state one has the recursion relation,

$$p_i = \Big(\frac{\frac{\mathcal{S}}{L} e^{-\beta\mu d} + W_0}{\frac{\mathcal{S}}{L} e^{\beta\mu d} + U_0} \Big)^i p_0$$

which by applying normalization condition gives the expression for the contact probability,

$$p_0 = \frac{U_0 - W_0 + \frac{\mathcal{S}}{L} e^{\beta\mu d} - \frac{\mathcal{S}}{L} e^{-\beta\mu d}}{\frac{\mathcal{S}}{L} e^{\beta\mu d} + U_0}; \ for\ \mu < \mu^*. \tag{3.3}$$

Alternatively, the binding site being driven by the growing filament, its velocity must be same as the growth velocity of the filament. The later quantity is simply $\{U_0 p_0 e^{-\beta\mu d} + U_0(1 - p_0) - W_0\}$, while the velocity of the binding site has the form $\{U_0 p_0 e^{-\beta\mu d} + \frac{\mathcal{S}}{L} e^{-\beta\mu d} - \frac{\mathcal{S}}{L}(1 - p_0) e^{\beta\mu d}\}$. Equating these two gives the same expression for p_0 as in Eq. (3.3).

For $\mu = 0$ and $\mathcal{S}/L = 1$, the contact probability $p_0 = \dfrac{U_0 - W_0}{1 + U_0}$. Using this value, we have $V_0 = \frac{d}{L}(U_0 - W_0)$. Comparison of this value with our simulation data in Fig. 3.2(a) show good agreement.

Next, we explain the presence of the peak in the $\mu - V$ curve. Note that for $\mu = 0$ the system has no steady state and the filament pushes the binding site upward, while other $(L-1)$ sites of the system which are not coupled (μ being zero), undergo equilibrium fluctuations

and show no net velocity. Consequently, the height difference between the binding site and the bulk sites and hence the contour length $\mathcal{C}$ keeps increasing with time. For nonzero μ there is an energy cost associated with stretching the membrane. This elastic force tries to reduce $\mathcal{C}$ and the bulk sites feel an upward pull towards the binding site. The strength of this pull increases as μ increases and this explains why the membrane velocity increases with μ. However, for small values of μ, this elastic force is not strong enough to counter the polymerization force exerted by the filaments, and the bulk sites are not able to catch up with the binding site, which still moves at a larger velocity and $\mathcal{C}$ keeps increasing with time. Finally, when μ reaches a critical value μ^*, such that the elastic force exactly balances the polymerization force, the average velocity of the bulk sites becomes equal to that of the binding site. As μ is increased further, the elastic force becomes stronger than the polymerization force and it becomes increasingly difficult for the filament to push the binding site. However, as soon as a successful polymerization takes place, and the binding site height increases, the bulk sites quickly catch up because the elastic energy associated with a nonflat profile is high for μ values in this range. The whole membrane now moves with the same velocity and $\mathcal{C}$ stabilizes. The membrane velocity in this case is dominated by the polymerization events at the binding site, the rate of which is $U_0 \exp(-\beta\mu d)$. Thus the membrane velocity decreases exponentially with μ in this range [see data in Fig. 3.2(a), inset].

To verify the above mechanism, we measure the velocity of the binding site and the bulk sites separately and plot the data in Fig. 3.2(b). As argued above, we find that for small μ, the binding site velocity is higher than the bulk site and these two velocities become equal for $\mu \geq \mu^*$. The difference between the binding site and the bulk site velocities can be alternatively measured by $\frac{<\mathcal{C}(t)-\mathcal{C}(0)>}{t}$ for large t, where $\mathcal{C}(0)$ is the initial contour length and $\mathcal{C}(t)$ is the length of the contour after evolving the system upto t MC steps. Our plot in Fig. 3.3(b) shows that for $\mu < \mu^*$, this quantity decreases linearly with μ and becomes zero at μ^*. We also measure the ratio $\lambda =< (|h_{b+1} - h_b| + |h_b - h_{b-1}| + 2d)/\mathcal{C} >$, averaged over different configurations. Here, b denotes the binding site. λ gives the fraction of contour length that is contained between the binding site and its two neighbors. For $\mu < \mu^*$, when the binding site moves faster than the rest of the membrane, for large times, this fraction is very close to 1, since the length of the rest of the membrane becomes negligible compared to the growing separation between the binding site and its neighbors. Our data in Fig. 3.3(a) show that λ stays at 1 for small μ and then shows a sharp fall at $\mu = \mu^*$. For $\mu \gg \mu^*$, when the polymerization is almost impossible and the membrane velocity is close to zero, the membrane is flat and λ then becomes $2/L$. In this limit, the membrane behaves like a rigid barrier, which was studied in Refs. [13, 17–19, 23, 31]. We find that after the sharp jump at $\mu = \mu^*$, the ratio λ decreases exponentially with μ to the asymptotic value $2/L$ [Fig. 3.3(a), inset]. Note that both for small and large μ, the binding site is the only site that is being pushed by the filament and the dynamics of bulk sites still follow local detailed balance. The

overall velocity of the membrane is thus generated by the drive present at the single binding site and this is the reason V scales inversely with the system size L.

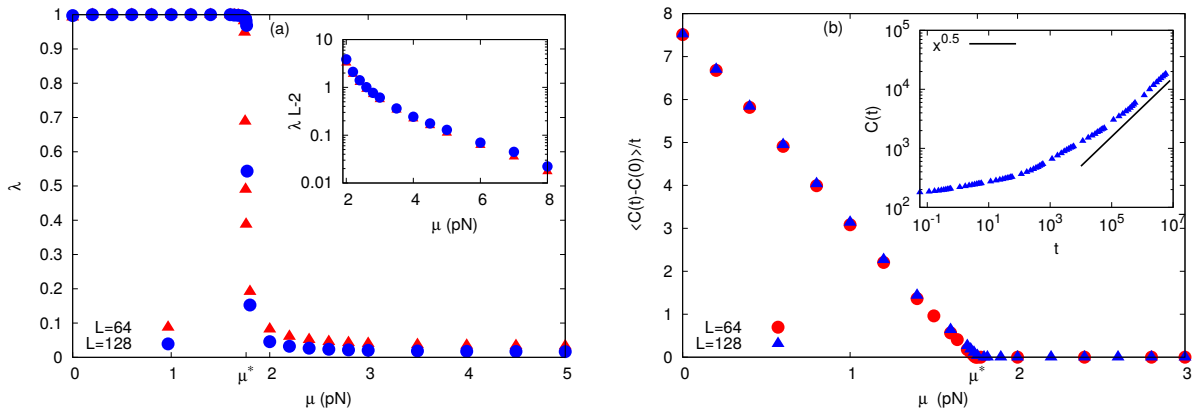

Figure 3.3: The membrane contour length keeps growing for $\mu < \mu^*$ and stabilizes for $\mu > \mu^*$. **(a):** The ratio $\lambda = 1$ for $\mu < \mu^*$ and decreases sharply at μ^* to its asymptotic value $2/L$ for large μ. **Inset:** The saturation of λ at large μ happens exponentially. **(b):** The quantity $\frac{<\mathcal{C}(t)-\mathcal{C}(0)>}{t}$, for large t, decreases with μ and becomes zero above μ^*. **Inset:** Variation of contour length with time at $\mu^* = 1.748pN$. We see that after large enough time, $\mathcal{C}(t)$ grows with time as $t^{0.5}$ with a diffusion constant $D = 37.41 \pm 7.19nm^2/s$. The analytically calculated value of $D = 41.352nm^2/s$ which is close to the numerical value. Here we use $L = 64$. For both panels $\mathcal{S}/L = 1$. Other simulation parameters are as in Table 2.1.

3.3.2 *Absence of steady state for $\mu < \mu^*$*

For $\mu < \mu^*$, when the binding site and bulk site velocities are different, and $\mathcal{C}$ keeps increasing with time, the system does not have a steady state. This seems somewhat surprising and in this subsection we discuss this issue in detail.

Let us define $z = 2h_b - h_{b+1} - h_{b-1}$. Our data in Fig. 3.4(a) show that for $\mu < \mu^*$, the sign of z is always positive and even for $\mu > \mu^*$, the probability to find negative z is negligible. This is expected, since for small μ, the binding site always stays above its neighbors, and for large μ, when the membrane is flat, the binding site is most of the time at the same level with its neighbors, but does not typically fall below that level. We show below that z performs a biased random walker with a reflecting boundary condition at the origin.

First note that z can increase either due to increase of h_b (from bound filament polymerization or thermal fluctuation at the binding site) which happens with rate $e^{-\beta\mu d}(p_0U_0 + 1)$, or due to decrease of $h_{b\pm1}$, which happens with rate 1. This is because our data in Fig. 3.4(b) show that the sites $(b \pm 1)$ almost always have one neighbor (site $b \pm 2$) at a lower height, and another neighbor (site b) at a higher height. From Eq. (3.1) it then follows that the height at the sites $(b \pm 1)$ can increase or decrease without any energy cost and rate of such processes is taken to be 1 [see, for example, Fig. 3.1(b)]. The value of z can decrease because of decrease

in h_b which releases elastic energy and happens with rate $e^{\beta\mu d}(1-p_0)$, or because of increase of $h_{b\pm1}$, which again happens with rate unity, as explained above. Let us define $P(z,t)$ as the probability for z at time t. Then the change in $P(z,t)$ in a small time $\triangle t$ can be written as,

$$\begin{aligned} P(z,t+\triangle t) - P(z,t) = \triangle t[&(1-p_0)e^{\beta\mu d}P(z+2d,t) + 2P(z+d,t) + 2P(z-d,t) \\ &+(1+U_0p_0)e^{-\beta\mu d}P(z-2d,t) - \{(1-p_0)e^{\beta\mu d} + 4 + (1+U_0p_0)e^{-\beta\mu d}\}P(z,t)] \end{aligned} \tag{3.4}$$

Here, we have considered $z > 0$ [supported by data in Fig. 3.4(a)] and put a reflecting boundary at the origin $z = 0$, such that z can never be negative. In the continuum limit, Eq. 3.4 becomes a Fokker-Planck equation for a biased random walker with drift and diffusion given by, respectively, $v = 2d\{(1+U_0p_0)e^{-\beta\mu d} - (1-p_0)e^{\beta\mu d}\}$ and $D = 2d^2\{(1-p_0)e^{\beta\mu d} + (1+U_0p_0)e^{-\beta\mu d} + 1\}$.

It can be easily seen that for small μ, the bias v is positive while for large μ, the bias v is negative. At $\mu = \mu^*$, v becomes zero and the system shows unbiased diffusion with diffusivity D. The value of μ^* can be obtained by equating v to zero and using the expression for p_0 from Eq. 3.3 which gives the resulting equation

$$W_0e^{3\beta\mu^*d} - U_0e^{2\beta\mu^*d} - (U_0^2 - U_0W_0 + U_0)e^{\beta\mu^*d} + U_0 = 0. \tag{3.5}$$

Numerical solution of the above equation gives only one physical solution for μ^*. We find $\mu^* = 1.81pN$, which is close to the value $1.748 \pm 0.004pN$ observed in simulations.

Due to the reflecting boundary condition at the origin, this implies that for $\mu < \mu^*$, the system does not reach a steady state, and $\langle z \rangle$ increases linearly with time, while for $\mu > \mu^*$, there exists a steady state and $\langle z \rangle$ reaches a time-independent value. At $\mu = \mu^*$, we have an unbiased random walker with reflecting boundary at the origin, for which there is no steady state either, but $\langle z \rangle$ in this case grows diffusively with time with a diffusion constant that matches our analytical expression given above [see Fig. 3.3(b), inset].

3.3.3 *Faster membrane dynamics lowers μ^**

So far we have considered the case for $\mathcal{S} = L$ membrane updates in one MC step. What happens when the membrane dynamics is faster or slower than this? Apart from the binding site, all the other $(L-1)$ bulk sites are being driven by only the elastic interaction. For large $\mathcal{S}$, when the bulk sites are updated at a higher rate, the effect of the elastic interaction is felt more strongly. As a result, the point of balance μ^*, where the elastic force and polymerization force become equal, now shifts towards a smaller value of μ. More specifically, for small but nonzero μ, when the bulk sites experience an upward bias towards the binding site, their total displacement in the upward direction per MC step increases, as $\mathcal{S}$ increases. Thus the

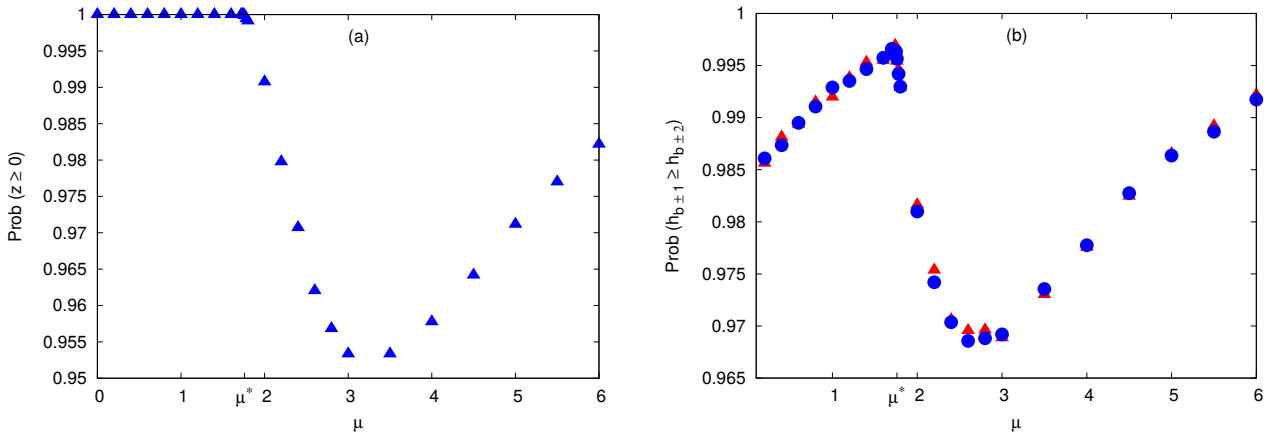

Figure 3.4: Height gradient around the binding site. **(a):** The probability that $z \geq 0$ as a function of μ. We see that the probability is exactly one for $\mu < \mu^*$ and even for $\mu > \mu^*$, it is very close to one. **(b):** Here we show the probability that $h_{b\pm1} \geq h_{b\pm2}$ as a function of μ. The red triangles are for $prob(h_{b+1} \geq h_{b+2})$ while the blue circles are for $prob(h_{b-1} \geq h_{b-2})$. These probabilities are also close to one for entire range of μ. Here, $L = 64$ and $\mathcal{S}/L = 1$. Other simulation parameters are as in Table 2.1.

bulk sites are able to catch up with the binding site at a smaller value of μ. In other words, as $\mathcal{S}$ increases, μ^* decreases. In Fig. 3.5(a) we plot $\mu - V$ data for different $\mathcal{S}/L$ values, and find that the peak of the curve shifts towards left as $\mathcal{S}/L$ increases. For $\mathcal{S}/L >> 1$, the value of μ^* becomes infinitesimally small and for any finite μ, the curve looks monotonic. In the inset of Fig. 3.5(a) we show the variation of μ^* with $\mathcal{S}/L$. Note, however, that the dependence is not very strong and μ^* deceases logarithmically slowly with $\mathcal{S}/L$. We see that over two decades of change of $\mathcal{S}$, the value of μ^* changes only by a factor of half. However, the membrane velocity measured at μ^* shows a more strong dependence on $\mathcal{S}/L$ and grows as a power law with an exponent $\simeq 0.87$ [Fig. 3.5(b)]. We can generalize our calculation in the last subsection for arbitrary values of $\mathcal{S}$ and obtain μ^* as the only one physical solution of the equation

$$\frac{\mathcal{S}}{L}\left(W_0 e^{3\beta\mu^* d} - U_0 e^{2\beta\mu^* d} - U_0 e^{\beta\mu^* d} + U_0\right) - (U_0^2 - U_0 W_0) e^{\beta\mu^* d} = 0. \tag{3.6}$$

The analytical result shown by the continuous line in the inset of Fig. 3.5(a) shows good agreement with numerical data over a wide range of $\mathcal{S}/L$.

Note that our calculation for the contact probability p_0 presented in Eq. 3.3 shows that for small μ and large $\mathcal{S}/L$, the contact probability is very small. This means that the filament is unbound most of the time and grows like a free filament with a net growth rate $d(U_0 - W_0)$, which is independent of μ. Since we measure the membrane velocity as the average displacement of the membrane per Monte Carlo step and we define our Monte Carlo step such that there are $\mathcal{S}$ surface updates and one filament update, our data in Fig. 3.6(a) show that the membrane velocity also approaches this limit as $\mathcal{S}/L$ becomes large. The $\mu - V$ curve in this case therefore becomes flat for small μ and then decreases for large μ, giving

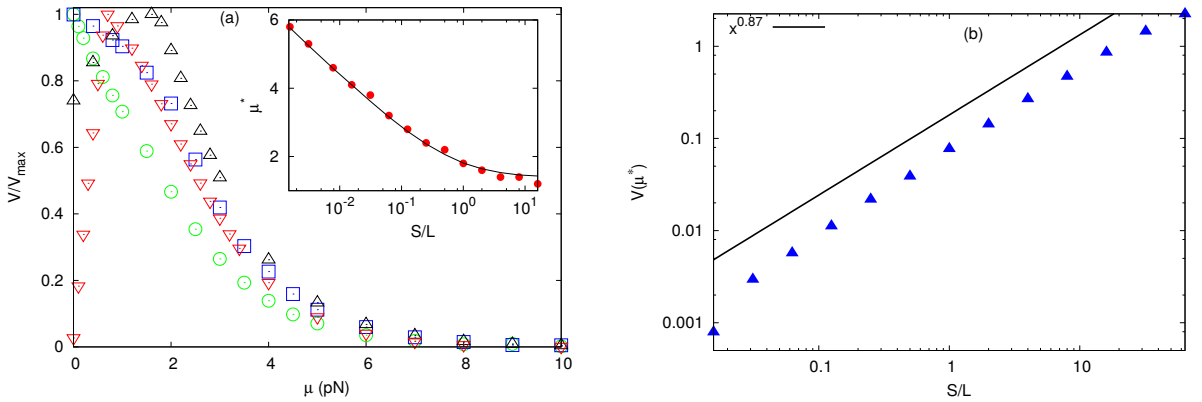

Figure 3.5: Peak position and peak height of $\mu - V$ curve depends on $\mathcal{S}/L$. **(a):** Scaled V as a function of μ for different $\mathcal{S}/L$ values. The scaling factor V_{max} has been used such that the data for different $\mathcal{S}/L$ values can be compared. In this plot the symbol $\circ$ correspond to $\mathcal{S}/L = 2^{-2}$ ($V_{max} \simeq 5.84 \times 10^{-2} nm/s$), the $\square$ correspond to $\mathcal{S}/L = 2^{-1}$ ($V_{max} \simeq 5.84 \times 10^{-2} nm/s$), the $\triangle$ correspond to $\mathcal{S}/L = 1$ ($V_{max} \simeq 7.89 \times 10^{-2} nm/s$) and the ∇ correspond to $\mathcal{S}/L = 2^{6}$ ($V_{max} \simeq 2.23 nm/s$). For smaller values of $\mathcal{S}/L$, the curve is monotonic as the velocity is mostly determined by the binding site. As $\mathcal{S}/L$ increases, the $\mu - V$ curve develops a peak at μ^*. **Inset:** μ^* decreases with $\mathcal{S}/L$. The discrete points from simulations match well with continuous line from Eq. (3.6). We use $L = 64$ here. **(b):** The membrane velocity at μ^* plotted against $\mathcal{S}/L$ shows a power law increase. The solid line represents a function $\sim x^{0.87}$ and goes parallel to our numerical data points. Here we have used $L = 64$. Other simulation parameters are as in Table 2.1.

rise to a concave curve, as shown in Fig. 3.6(a). Thus the $\mu - V$ curve can change its shape from convex to concave depending on the choice of the relative time scale $\mathcal{S}/L$ [30, 31, 62].

In the limit of very large $\mathcal{S}/L$, when the membrane fluctuations occur much more rapidly than the filament polymerization, the membrane reaches a thermal equilibrium between two filament movements. The partition function for the system can be calculated in this case and the average contour length $\langle \mathcal{C} \rangle$ of the membrane can be obtained from there, which has the form $\langle \mathcal{C} \rangle = Ld/(1 - e^{-\beta \mu d})$. In Fig. 3.6(b) we compare it with numerics and find reasonably good agreement for large $\mathcal{S}/L$.

3.3.4 *For large μ the membrane behaves as a rigid obstacle*

When μ is very large, the membrane remains flat most of the time. Whenever there is a filament polymerization, the height of the binding site increases, but due to high elastic energy cost associated with such a configuration, the bulk sites quickly catch up and the membrane is flat again. We find that the membrane behaves like a perfectly rigid barrier in this case. Let p_i be the probability to find a gap of length i between the filament tip and the binding site. For a rigid barrier without any independent movement, this gap can only increase or decrease due to filament polymerization or depolymerization. In Sec. 2.3.1 of Chapter 2, we consider such a case, where we ignore any change in p_i due to the height

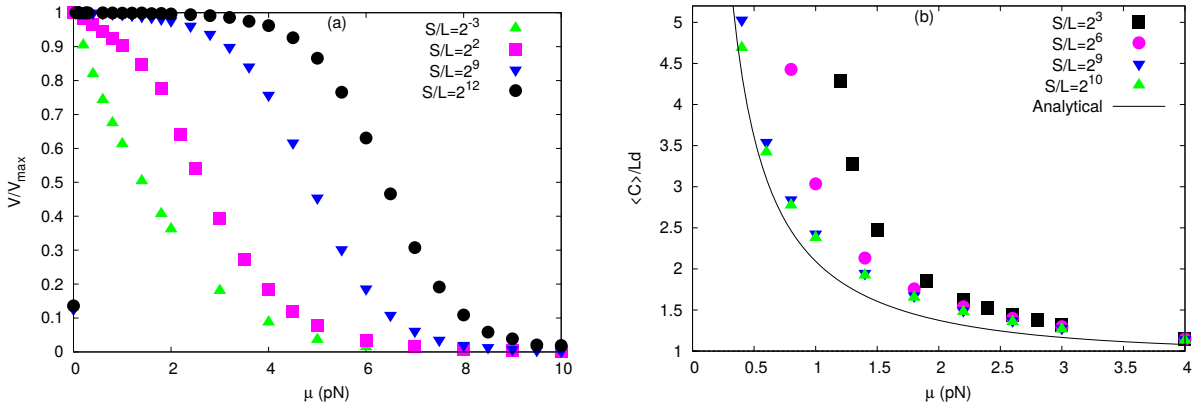

Figure 3.6: Variation of membrane velocity and contour length against μ for different values of $\mathcal{S}/L$. **(a):** The $\mu - V$ curve changes from convex to concave as $\mathcal{S}/L$ is increased. For $\mathcal{S}/L << 1$, the curve is convex while for $\mathcal{S}/L >> 1$, it becomes concave. Here, we have scaled V by V_{max} such that we can compare them in the same scale. The values of V_{max} are $4.67 \times 10^{-1} nm/s$, $4.67 \times 10^{-1}, nm/s$, $3.73 nm/s$, and $3.73 nm/s$, respectively, in the increasing order of $\mathcal{S}/L$. Here, we have used $L = 8$. **(b):** Average contour length of the membrane scaled by Ld as a function of μ for different values of $\mathcal{S}/L$. The continuous line is from analytical calculation in the equilibrium limit, which matches with simulation for very high $\mathcal{S}/L$. Other simulation parameters are as in Table 2.1.

fluctuations and p_i changes only due to the filament dynamics. Thus, in a similar way, we have $p_0 = 1 - W_0/U_0 \simeq 1/2$ (Using the value of U_0 and W_0 from Table 2.1).

In Fig. 3.7(a), we show the variation of p_0 with μ for different $\mathcal{S}/L$ and find that for large μ, the contact probability indeed saturates to $1/2$, the rigid barrier limit. Smaller the value of $\mathcal{S}/L$, faster is the saturation. For small μ, the contact probability can be calculated analytically (see Eq. 3.3) and in Fig. 3.7(a) this has been shown by solid lines, which agree well with the simulations. Our calculation remains valid only for $\mu < \mu^*$ and hence the comparison has been done only in this regime. μ^* becomes too small for very large $\mathcal{S}/L$, and hence not marked in this plot. In the case for $\mathcal{S}/L << 1$, when the membrane dynamics is very slow, the thermal fluctuations of the membrane can be neglected and the contact probability is essentially controlled by the polymerization and depolymerization of the filament. Thus we find that the contact probability approaches $1/2$ even for $\mu < \mu^*$ in this case [shown by red triangles in Fig. 3.7(a)]. However, the system is not in steady state here and the contour length of the membrane keeps increasing with time. In Fig. 3.7(b) we plot the ratio $\lambda =< (|h_{b+1} - h_b| + |h_b - h_{b-1}| + 2d)/\mathcal{C} >$ and show this explicitly.

3.4 RESULTS FOR MULTIPLE FILAMENTS

In the previous section, we have considered the case of single filament. In this section, we will present a brief discussion on multiple filaments. Let us define the filament density as $\rho = N/L$. We find for $\rho \ll 1$, and for uniform distribution for the binding sites, the qualitative

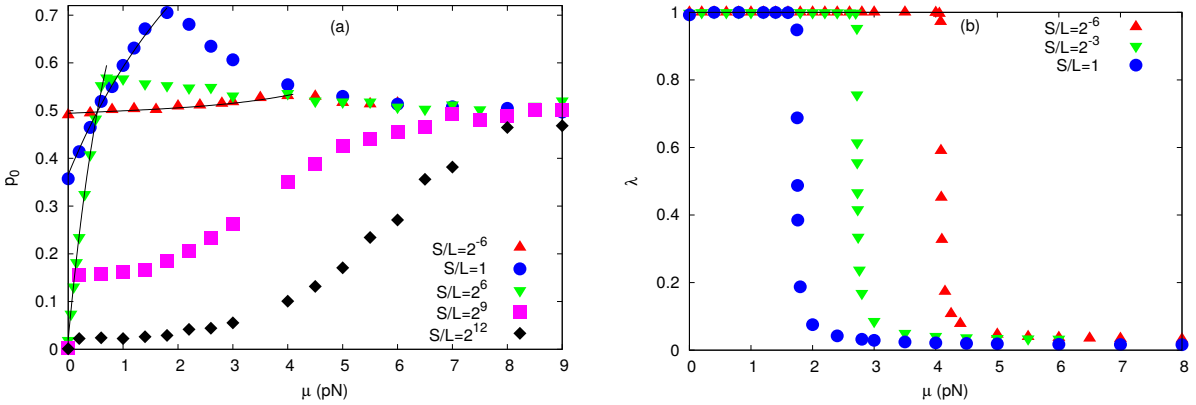

Figure 3.7: For $\mu >> 1$, the membrane behaves as a rigid obstacle. **(a):** The contact probability p_0 for different values of $\mathcal{S}/L$. The continuous lines are from the analytical predictions, which are valid only for $\mu < \mu^*$ and thus compared only upto this region. For large μ, the value of p_0 saturates to $1/2$, which is expected for a rigid barrier. As $\mathcal{S}/L$ decreases, the rigid barrier behavior sets in for smaller μ values. The continuous lines show analytical calculation in $\mu < \mu^*$ regime. **(b):** The variation of λ for different values of $\mathcal{S}/L$. For small μ, the value of λ is unity, which means that the contour length of the membrane diverges with time. For high enough value of μ, λ saturates to $2/L$. We use $L = 64$ for both the plots. Other simulation parameters are as in Table 2.1.

behavior is same as that for single filament. In Fig. 3.8(a), we show the $\mu - V$ curve for multiple filaments for small ρ. Since the membrane velocity results from the polymerization force exerted at the binding sites (motion at all other sites follows local detailed balance, as mentioned in Sec. 3.2), our data show that V scales as ρ. The non-monotonicity of the $\mu - V$ curve means that even for multiple filaments, the system fails to reach a steady state for small μ and the membrane contour length $\mathcal{C}$ keeps increasing with time. We have checked that (data not shown) at $\mu = \mu^*$ the contour length grows diffusively with time and for $\mu > \mu^*$ system reaches a steady state when $\mathcal{C}$ has a finite value. Figure 3.8(b) shows the $\mu - V$ curve for different values of $\mathcal{S}/L$. We note that for $\mathcal{S}/L << 1$, the curve is convex while for $\mathcal{S}/L >> 1$, it becomes concave.

As ρ increases, the elasticity of the membrane induces an effective interaction between the filaments and the single filament picture does not remain valid any more. Our data in Fig. 3.9 show that $V \sim \rho$ scaling is lost and μ^* now depends on ρ. For large ρ, most of the sites are binding sites and are driven by the filaments. Due to elastic interaction, the remaining few bulk sites feel an upward pull and are able to catch up with the binding sites at smaller μ values. Thus μ^* decreases with ρ for large ρ. When $\rho = 1$, the system will reach steady state for all values of μ but for $\rho < 1$, there will always be a nonzero μ^* below which the system does not have a steady state.

In the above discussion, we have assumed that the binding sites are distributed uniformly throughout the membrane. If we consider an inhomogeneous distribution of binding sites, then for small μ, the region of the membrane where the density of binding sites is high,

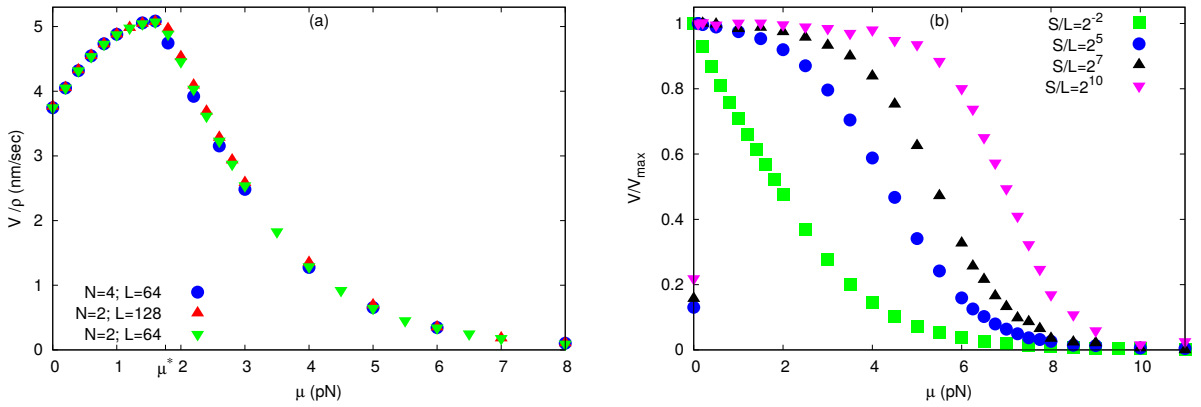

Figure 3.8: $\mu - V$ curve for multiple filaments with $\rho \ll 1$. **(a):** The velocity scales with ρ similar to the single filament case. It also shows a peak at $\mu = \mu^*$ which is independent of ρ. We have used $\mathcal{S}/L = 1$ here. **(b):** Scaled velocity as a function of μ for different time scales which show that the curve changes from convex to concave similar to the single filament case. For $\mathcal{S}/L << 1$, the curve is convex while for $\mathcal{S}/L >> 1$, the curve becomes concave. The values of V_{max} are $0.467nm/s$, $3.71nm/s$, $3.74nm/s$ and $3.75nm/s$ for $\mathcal{S}/L = 2^{-2}, 2^5, 2^7$, and 2^{10}, respectively. Here we have used $N = 4$ and $L = 32$. Other simulation parameters are as in Table 2.1.

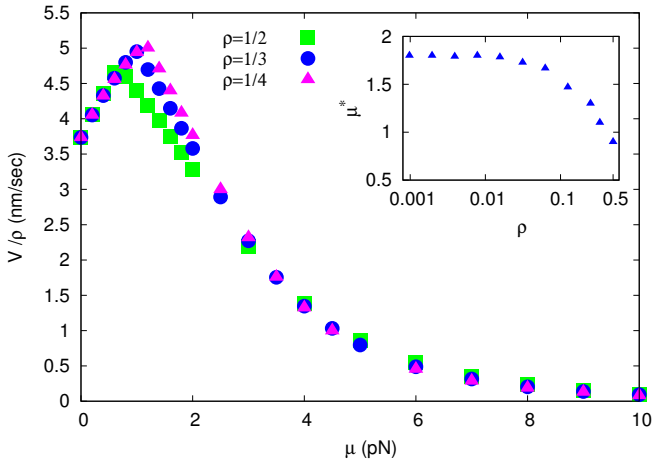

Figure 3.9: Results for multiple filaments with high filament density. In the main plot, we show $\mu - V$ curve for multiple filaments for $\rho \sim 1$. We note that V does not scale with ρ. The peak position μ^* decreases with ρ. The inset shows the variation of μ^* with ρ. We note that for $\rho << 1$, the value of μ^* remains constant and then decreases with ρ for high value of ρ. We use $\mathcal{S}/L = 1$ here. Other simulation parameters are as in Table 2.1.

will have a large local velocity since it is being driven by a large number of filaments. On the other hand, the part of the membrane where binding sites have a low density, will have a much smaller local velocity. In order for the whole system to reach a steady state, the velocity should be same everywhere on the membrane. This means that the polymerization force present in the fastest part of the membrane has to be smaller than the elastic interaction which pushes the slowest part of the membrane where binding site density is lowest. A very large value of μ is required to achieve this balance. Thus μ^* becomes very large in the case

of inhomogeneous distribution of binding sites. We have verified this in our simulations. We distribute the filaments inhomogeneously such that a section of the membrane have filament density $\rho = 1/2$ (denser part) while another section of the membrane have filament density $\rho = 1/8$ (rarer part). We note that for the denser part, the average velocity of a bulk site and a binding site becomes equal at smaller value of $\mu(= 0.5pN)$, but the rarer part of the membrane still moves with the velocity smaller than that of the denser part. Thus, the system is not in the steady state. The system reaches steady state at $\mu^* = 5.80 \pm 0.04pN$, where the velocity of all the sites become equal. This value is much higher than the homogeneously distributed case (see Fig. 3.10).

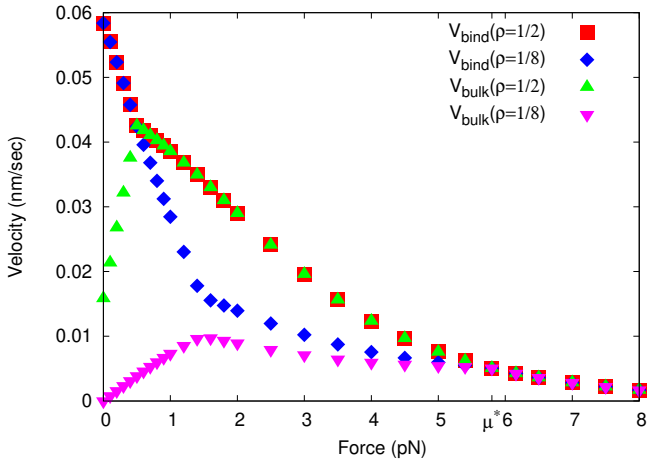

Figure 3.10: Inhomogeneous distribution of filaments. For the denser part of the membrane, $\rho = 1/2$ while for the rarer part, $\rho = 1/8$. We note that for the denser part, $V_{bind} = V_{bulk}$ at $\mu = 0.5pN$, while the rarer part still moves with smaller velocity. The velocity of all the sites become equal at $\mu^* = 5.80 \pm 0.04pN$, which is much higher than the homogeneous distribution of filaments. We use here $N = 20$, $L = 64$ and $\mathcal{S}/L = 1$. Other simulation parameters are as in Table 2.1.

3.5 CONCLUSIONS

In summary, we study in this chapter, the force generation mechanism by a set of parallel filaments growing against an elastic membrane. We describe the elastic membrane using a one dimensional Solid-On-Solid (SOS) model [25, 72–74]. The elastic membrane tends to stay flat and any distortion from this flat state costs energy. We find that the polymerization force wins over the elastic force of the membrane for low values of the membrane tension and the system fails to reach a steady state. This gives rise to a nonmonotonic dependence of membrane velocity on its elasticity. Our detailed numerical simulations of various different quantities, accompanied by analytical calculations and simple scaling arguments provide a comprehensive picture of the behavior of the system in the long time limit. We also highlight the importance of the relative time scale between the dynamics of the membrane and the

filaments to determine the qualitative nature of the dependence of membrane velocity on elasticity. While for fast membrane dynamics, the velocity is a concave function of membrane elasticity, for slow membrane dynamics a convex dependence is observed.

Throughout this chapter, we have assumed the membrane to be homogeneous with same elasticity along the whole membrane. However, in many physical systems there can also be tension gradient along the membrane [75, 76]. Our results for the simple model will pave way for studying more complex models where above mentioned effects are included.

4

ACTIN FILAMENTS GROWING AGAINST AN ELASTIC MEMBRANE: GAUSSIAN MODEL

4.1 INTRODUCTION

In our last chapter, we have studied the force generation by actin filaments growing against an elastic membrane, where we consider the elastic energy to be proportional to the contour length of the membrane [25, 72, 74]. In literatures, another form of elastic interaction is widely used, where the elastic energy is taken to be proportional to the sum of squares of local height gradients [26, 73]. In the present chapter, we would like to study this case. We call it the "Gaussian model". We are interested to find out how the membrane elasticity in this case affects the growth of the filaments and how the polymerization force exerted by the filaments affects the membrane deformations.

In the present case, we find that the membrane velocity decreases monotonically with the membrane elastic constant ν and steady state is reached for all nonzero values of ν, which is different from the gradient model, where we have the absence of steady state for small elasticity. In the present model also, we note that the relative time-scale between the membrane dynamics and the filament dynamics is crucial to determine the qualitative shape of the elasticity-velocity curve. Some of the results discussed above have been published in [70].

4.2 DESCRIPTION OF THE MODEL

The description of the system is same as the gradient model. The system consists of a set of N parallel filaments growing against an elastic membrane as shown in Fig. 3.1. The form of the Hamiltonian in this case is [26, 73]

$$\mathcal{H}_2 = \nu \sum_{i=1}^{L} (h_i - h_{i+1})^2 \tag{4.1}$$

where ν denotes the elastic constant. In this case, energy depends on the square of the local height gradients, and hence the energy cost to extend the membrane by a certain amount also depends on the contour length $\mathcal{C}$. For large $\mathcal{C}$ values, the energy cost also goes up, as expected for an elastic body. We refer this model as "Gaussian model". The dynamics of the system is same as described in the case of gradient model (see Sec. 3.2 of Chapter 3).

In the present model, if the height of the j-th site, h_j changes to $h_j \pm d$, then the change in energy, $\Delta E = 2d\nu[d \pm (2h_j - h_{j+1} - h_{j-1})]$, depends on the local height configuration around the j-th site. This is different from the gradient model, where ΔE is constant. Following the local detailed balance [see Eq. (3.2)] we use in our simulations $R_+ = e^{-\beta\Delta E}$, and $R_- = 1$, while all other movements of the membrane where the energy of the barrier does not change, occur with rate unity.

4.3 RESULTS FOR SINGLE FILAMENT

In this section, we present our results for the single filament and then in the next section, we discuss the case of multiple filaments.

4.3.1 *Membrane velocity decreases with ν*

For $\nu = 0$, there is no difference between gradient model and Gaussian model (Eqs. 3.1 and 4.1). Therefore, as derived in Sec. 3.3.1, the membrane velocity at $\nu = 0$ is given by $V_0 = d(U_0 - W_0)/L$. The membrane contour length $\mathcal{C}$ keeps increasing with time and the system does not have a steady state. However, as soon as ν is nonzero, any polymerization event or independent thermal fluctuation that causes an increase in $\mathcal{C}$, has an energy cost which is higher as $\mathcal{C}$ gets larger. Thus the membrane can not stretch indefinitely and for all $\nu > 0$ the system reaches a steady state. Our data in Fig. 4.1(a) show that for $\nu > 0$, the membrane velocity V decreases as ν increases. For large ν, the decay is exponential (Fig. 4.1(a), top inset) and we also find $V \sim 1/L$ scaling, as seen earlier in Fig. 3.2 for the gradient model.

Note that there is a discontinuity of the $\nu - V$ curve at $\nu = 0$ (see Fig. 4.1(a), main plot). The data in Fig. 4.1(a), bottom inset show that as $\nu \to 0$, the velocity saturates to a value, which is different from the value $V_0 = d(U_0 - W_0)/L$ at $\nu = 0$. This is because at $\nu = 0$, only the binding site of the membrane has nonzero velocity and the bulk sites have zero velocity. But as soon as $\nu \neq 0$, the system has a steady state and the bulk sites must move with the same velocity as the binding site. This sharp jump in the bulk sites velocity causes the discontinuity in the $\nu - V$ curve.

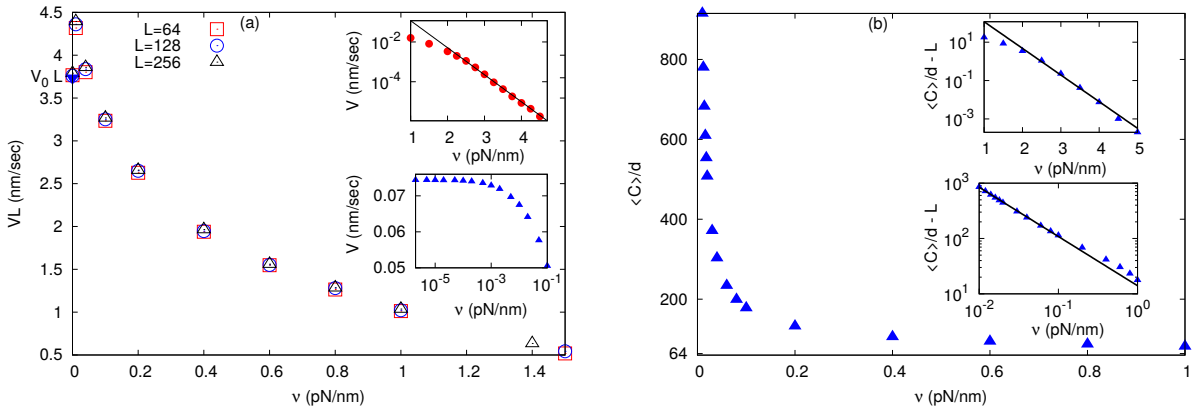

Figure 4.1: Variation of velocity and contour length with ν for Gaussian model. **(a):** The $\nu - V$ curve for single filament shows $1/L$ scaling. The curve is monotonic for all $\nu \neq 0$. **Top inset:** The velocity falls exponentially with decay constant $\simeq 3.13$, which is close to $2\beta d^2$. **Bottom inset:** In the limit of very small ν, the velocity saturates to a value $\sim 0.074nm/sec$, that is distinctly different from $V_0 = 0.058nm/s$ at $\nu = 0$. We use $L = 64$ for the insets and $\mathcal{S}/L = 1$ for all the plots. **(b):** Average contour length of the membrane scaled by d as a function of ν. For very high value of ν, $< \mathcal{C} >$ becomes equal to the system size Ld. **Top inset:** Contour length decreases exponentially for large μ with a decay constant $\simeq 3.2$ which is again close to $2\beta d^2$. **Bottom inset:** For very small ν, contour length falls off with ν as a power law with an exponent $\simeq 0.9$. For all the above plots, we use $L = 64$ and $\mathcal{S}/L = 1$. Other simulation parameters are as in Table 2.1.

In Fig. 4.1(b) we plot the steady state average contour length $\langle \mathcal{C} \rangle$ as a function of ν. We find that (top inset) $\langle \mathcal{C} \rangle$ decreases exponentially for large ν, as found in the gradient model (also see Fig. 3.3). For very small ν, our data (Fig. 4.1(b), bottom inset) show that $\langle \mathcal{C} \rangle$ decreases as a power law with an exponent $\simeq 0.9$. The power law decay can be explained as follows.

For very small ν, the local height gradient of the membrane decreases sharply as a function of the distance from the binding site and we have $y_b > y_{b+1} > y_{b+2}...$, where $y_i = h_i - h_{i+1}$ and b denotes the binding site. The bound filament polymerization and thermal height fluctuations at the binding site may change h_b which actually changes $\mathcal{C}$. It is easy to see that the rate of these processes that increase h_b is $(1 + U_0 p_0) e^{-2\beta\nu d^2(2y_b+1)}$ and that decrease h_b is $(1 - p_0)$. The height fluctuations of the other sites will not change $\mathcal{C}$. In the steady state, $\mathcal{C}$ is time-stationary, the increasing and decreasing rates must be equal, from which it follows that $y_b \sim 1/\nu$. Moreover, in the steady state, the velocity of all membrane sites are equal. The velocity at the binding site is given by $\{(1 + U_0 p_0) e^{-2\beta\nu d^2(2y_b+1)} - (1 - p_0)\}$, and that at the neighboring site $(b + 1)$ is $\{1 - e^{-2\beta\nu d^2(y_b - y_{b+1}+1)}\}$. Once we equate them, it follows that $y_{b+1} \sim 1/\nu$ for small ν. Equating the velocity of the sites $(b + 1)$ and $(b + 2)$, it can be similarly shown that $y_{b+2} \sim 1/\nu$, and thus for any site i, $y_i \sim 1/\nu$ holds. Thus the quantity $(< \mathcal{C} > - Ld = \sum_i |y_i|)$ shows an $1/\nu$ dependence. Our numerical data yields power law exponent 0.9 which is close to this prediction.

4.3.2 *Faster membrane dynamics yields a concave $v - V$ curve*

The relative time-scale between the membrane and filament dynamics is an important parameter for the Gaussian model also. The contact probability p_0 that is crucial to determine the interaction between the filament and the membrane depends strongly on whether the membrane dynamics is faster or slower than the filament dynamics. For very large v, it is expected that $p_0 \simeq 1/2$ since the membrane behaves like a rigid barrier in this limit (also see our discussion in Sec. 3.3.4). However, when v is small, our data in Fig. 4.2(a) show that the variation of p_0 with v is qualitatively determined by the value of $\mathcal{S}/L$. For $\mathcal{S}/L \gg 1$, the thermal fluctuations of the membrane happen so fast that the contact with the filament tip is lost most of the time and p_0 is small. From this small value, p_0 increases to $1/2$ as v becomes large. For $\mathcal{S}/L \ll 1$, the membrane fluctuations become almost negligible and the contact probability is controlled by the (de)polymerization of the (bound) free filament which does not depend on v. Our data for small $\mathcal{S}/L$ support this [Fig. 4.2(a)].

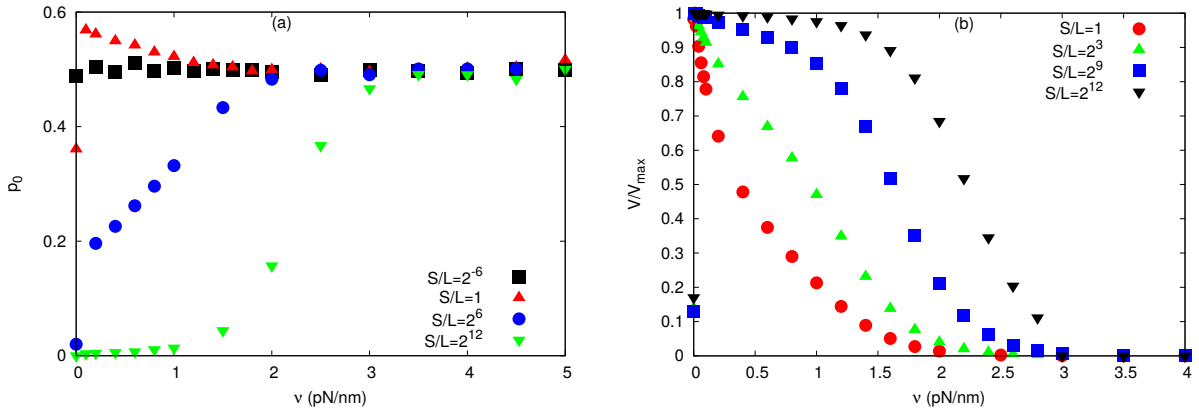

Figure 4.2: Contact probability and velocity as a function of v in a Gaussian model for different values of $\mathcal{S}/L$. **(a):** For $\mathcal{S}/L << 1$, p_0 does not show much variation and its value remains close to $1/2$. For $\mathcal{S}/L \sim 1$, in the small v region, the value of p_0 is higher than $1/2$ which then saturates to its rigid barrier limit for high v. For $\mathcal{S}/L >> 1$, p_0 starts with very small value and then increases with v, then saturates to $1/2$. Higher the value of $\mathcal{S}/L$, slower the tendency to reach $1/2$. We use $L = 8$ here. **(b):** The $v - V$ curve changes from convex to concave as $\mathcal{S}/L$ is increased. The values of V_{max} are $0.475nm/s$, $3.50nm/s$, $3.72nm/s$, and $3.73nm/s$ for $\mathcal{S}/L = 1, 2^3, 2^9$ and 2^{12} respectively. Other simulation parameters are as in Table 2.1.

The behavior of p_0 has a direct influence on the $v - V$ curve and we show in Fig. 4.2(b) that the curve becomes concave from convex as $\mathcal{S}/L$ is increased. When $\mathcal{S}/L \gg 1$, the filament is most of the time unbound for small v and hence the membrane velocity remains constant at $d(U_0 - W_0)/L$, same as that for a free filament. For large v, when p_0 starts increasing again, V decreases. The $v - V$ curve is concave in this case. On the other hand, for very small $\mathcal{S}/L$, the value of p_0 is no longer negligible and it remains nearly $1/2$ throughout the region. In

this case, due to the increase in v, the velocity starts decreasing even in the small v range, which yields a convex curve.

In the limit of very fast membrane dynamics, we can neglect the filament dynamics and assuming equilibrium we can calculate the average elastic energy of the membrane, as done in the previous chapter for gradient model [Fig. 3.6(b)]. We note that for the present case also, the analytical calculation shows good agreement with our numerics for very large $\mathcal{S}/L$ (see Fig. 4.3).

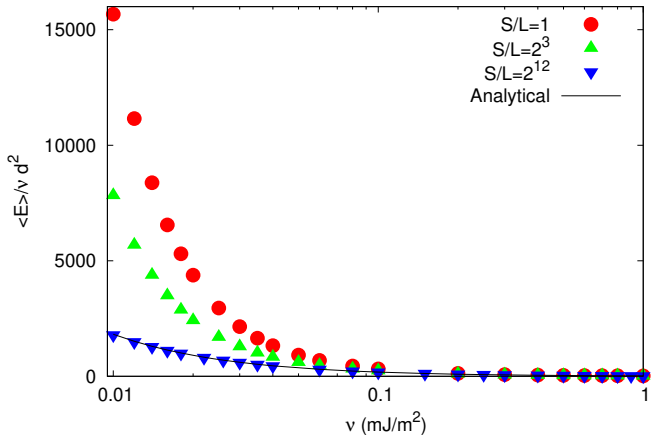

Figure 4.3: Average energy of the membrane scaled by vd^2 as a function of v for different values of $\mathcal{S}/L$. The continuous line is from analytical calculation in the equilibrium limit, which matches with simulation for very high $\mathcal{S}/L$. Other simulation parameters are as in Table 2.1.

4.4 RESULTS FOR MULTIPLE FILAMENTS

The multiple filaments case is qualitatively the same as the single filament case. For low density of filaments ($N/L = \rho \ll 1$), we plot the $v - V$ curve in Fig. 4.4(a). We find that V decreases monotonically with v for nonzero v and scales as ρ. The decay of V is exponential for large v with a decay constant which is same as that in the single filament case. In the limit of large v, the membrane behaves like a rigid barrier and apart from an overall scaling of V by a factor ρ, its dependence on v remains same for single or multiple filaments. The qualitative shape of $v - V$ curve is also found to change with $\mathcal{S}/L$, similar to the single filament case [Fig. 4.4(b)].

One interesting observation that can be made for the multiple filaments case is the merging of membrane protrusions. We study merging of membrane protrusion within our simple model by monitoring the contour length l of the membrane between two binding sites at a distance k apart. When the protrusions created at the two binding sites merge with each other, l becomes equal to k. In Fig. 4.5, we plot $\frac{(l-k)}{k}$ as a function of v for a fixed k for the

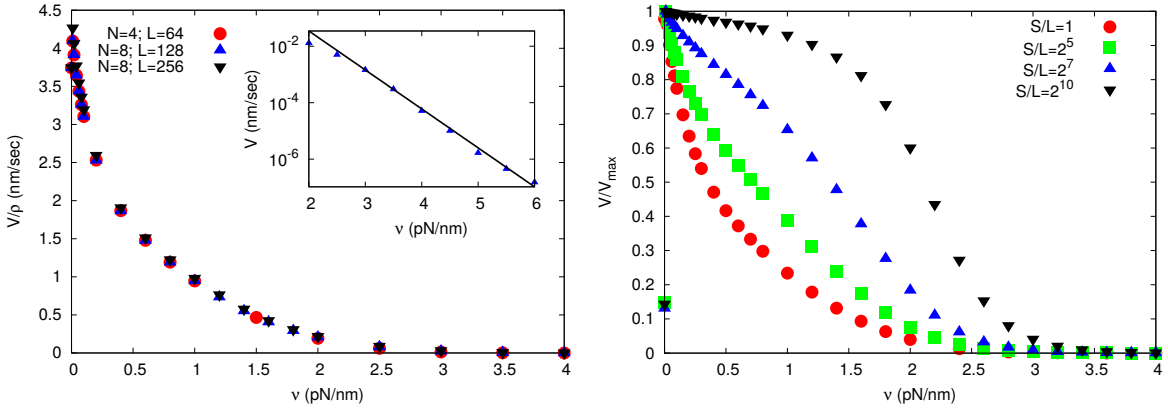

Figure 4.4: Results for multiple filaments. **(a):** The velocity scales with ρ. For large value of ν, the velocity falls exponentially with a decay constant $\simeq 3.18$, which is close to the single filament case. We use $\mathcal{S}/L = 1$ and for the inset, $N = 8; L = 128$. **(b):** The $\nu - V$ curve changes from convex to concave as $\mathcal{S}/L$ is increased. The values of V_{max} are $0.477nm/s$, $3.167nm/s$, $3.616nm/s$, and $3.723nm/s$ for $\mathcal{S}/L = 1, 2^5, 2^7$ and 2^{10} respectively. We use $N = 4; L = 32$ here. Other simulation parameters are as in Table 2.1.

barrier with only two filaments. We find that as ν is increased, the ratio decreases and the decrease is exponential for moderate to large ν values. In Fig. 4.5 inset, we show how the two protrusions merge as ν increases.

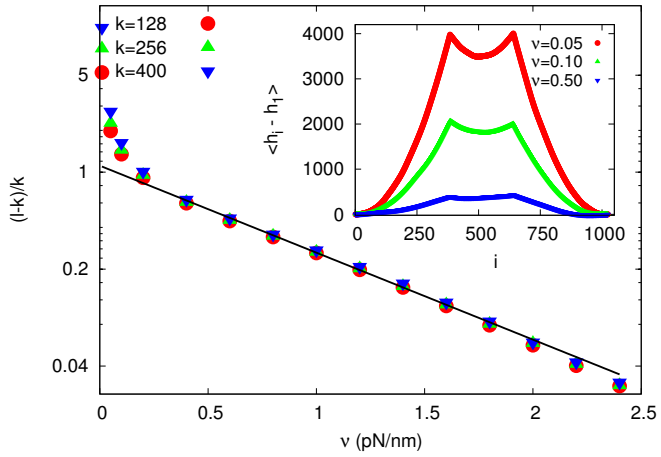

Figure 4.5: Merging of protrusions. We plot the quantity $\frac{(l-k)}{k}$, for the membrane with only two binding sites at a distance k apart, with l being the contour length between the two binding sites. For a given k, this quantity decreases with ν exponentially with a decay constant $\simeq 1.44$, which indicates merging of two protrusions for large ν. Here we use $L = 1024$ and $\mathcal{S}/L = 1$. **Inset:** Two protrusions merge as we increase ν. The average height profile of the membrane is shown for different values of ν. Note that the height of the protrusions also become shorter as ν increases. The ν values appearing in the legends are in the unit of pN/nm. These data are for $k = 256$. We use $L = 1024$ and $\mathcal{S}/L = 1$. Other simulation parameters are as in Table 2.1.

4.5 CONCLUSIONS

In this chapter, we study the force generation mechanism by a set of parallel filaments growing against an elastic membrane, where the elastic energy is proportional to the square of the local height gradients. We find that the membrane velocity monotonically decreases with elasticity and the system always reaches a steady state for all nonzero elasticity. This result is in contrast with the result for the gradient model, where we have absence of steady state even for non zero elasticity. We also highlight the importance of the relative time scale between the dynamics of the membrane and the filaments to determine the qualitative nature of the dependence of membrane velocity on elasticity. While for fast membrane dynamics, the velocity is a concave function of membrane elasticity, for slow membrane dynamics a convex dependence is observed. Therefore, the effect of relative time-scale in this case is same as the gradient model. We also note that two nearby protrusions appear to merge, as the elasticity increases. In earlier studies of a more detailed modelling of cell membrane [24], it was shown that actin filament polymerization gives rise to filopodial protrusions. The protrusion speed depends on elastic properties of the membrane and the membrane distortion also induces an effective attraction between the filopodia and close by filopodia merge together to form a larger (wider) protrusions. In our case, within the simple modelling, we are able to show such an interesting effect.

5

MEMBRANE WITH ELASTIC AND BENDING ENERGY: HELFRICH HAMILTONIAN MODEL

5.1 INTRODUCTION

In our last two chapters (Chapter 3 and 4), we study the force generation mechanism by actin filaments growing against a membrane considering its elastic energy while neglect its bending energy. However, the cell membrane also possesses bending rigidity, that has been measured in [42–46]. In this chapter, we study the force generation mechanism by actin filaments growing against a membrane by explicitly considering its bending rigidity along with its elastic tension [24, 27, 28]. We describe the energy of the barrier by the Helfrich Hamiltonian [47], that contains both the elastic as well as the bending energy. The elastic energy is considered to be proportional to the square of height gradients, similar to the Gaussian model, while the bending energy is considered to be proportional to the square of the Laplacian of height. We are interested to know how the introduction of the bending rigidity affects the force generation process in this case.

Pushed by the growing filaments, the membrane develops a net velocity along the direction of filament growth. For moderate or high values of bending rigidity κ, the membrane velocity V shows interesting variation as a function of membrane tension σ. Starting from a non-zero value at $\sigma = 0$, the velocity first decreases with σ, reaches a minimum, then increases again, reaches a peak, and finally decreases to zero as σ becomes very large. This dependence is highly unusual, since one would normally expect V to show a monotonic decrease with σ because as σ increases it ought to become more difficult to push the membrane. We show that the counter-intuitive behavior results from an interplay between the elastic and bending energy scales of the system. With increasing σ, elastic energy cost for creating a local protrusion in the membrane increases monotonically, as expected, but the bending energy cost shows a peak, which in turn gives rise to a peak in the total energy cost. In other words, there is a range of σ values for which it becomes easier for the system to create a membrane protrusion as σ is increased with κ held fixed. The membrane velocity increases in this range as a result.

To understand the mechanism behind the peak in bending energy cost we examine the shape of the membrane and show that a qualitative change in the shape is responsible for this effect. In the limit when both σ and κ are large, the membrane height varies slowly in space and one can neglect higher order derivative of height and assume height profile of a protrusion is almost linear, as shown in Fig. 5.1(c) and 5.1(d). For such a local shape of the membrane, the bending energy has a non-zero value at the binding site, where the filament is in contact with the membrane. Everywhere else on the membrane the bending energy is negligible. As σ decreases slightly but still remaining large, the shape of the membrane remains qualitatively same, but height gradient magnitude now increases and the bending energy becomes significantly large at the binding site. To minimize this energy, as σ is lowered further, the membrane shape finally changes qualitatively, and becomes as shown in Fig. 5.1(a) and 5.1(b), where the peak gets rounded and height profile also does not remain linear anymore. While the bending energy now is non-zero even away from the binding site, its variation across the membrane happens more gradually. The bending energy cost to create a local protrusion, which is proportional to the fourth derivative of height, decreases for such a configuration, as σ is lowered.

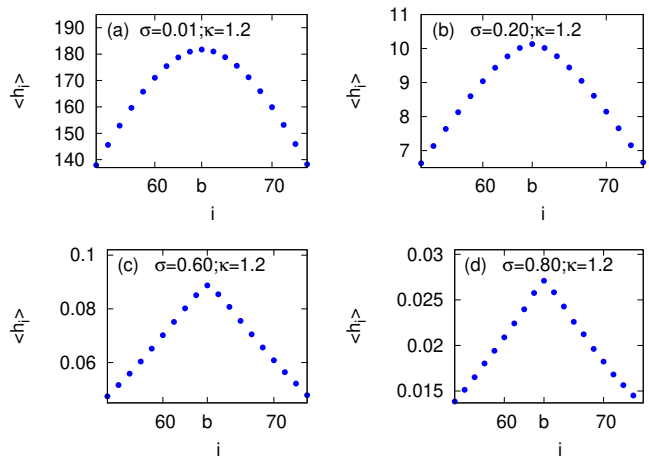

Figure 5.1: Shape of the membrane for different κ and σ. We note that for small σ but large κ (a and b), the shape of the membrane is such that the height gradient closer to $i = b$ (where the filament is driving the membrane) has smaller magnitude. On the other hand, for both large κ and σ (c and d), the shape of the membrane is linear, where the height gradient at all the sites are constant, with a peak in height at the site $i = b$.

This chapter is organized as follows. In Sec. 5.2, we describe our models. Our results for the single filament is presented in Sec. 5.3 and the results for the multiple filaments are described in Sec. 5.4 and conclusions are in Sec. 5.5.

The present system consists of a set of N parallel filaments growing against a membrane of size L, whose energy is described by the Halfrich Hamiltonian of the form,

$$\mathcal{H} = \sigma \sum_{i=1}^{L} (h_i - h_{i-1})^2 + \kappa \sum_{i=1}^{L} (h_{i-1} - 2h_i + h_{i+1})^2 \tag{5.1}$$

where $\{h_i\}$ denotes the height profile of the membrane, σ is the elastic tension and κ is the bending rigidity. The first term denotes the elastic energy which is proportional to the square of gradient of height. The second term, which proportional to the square of the Laplacian of height, describes its bending energy. A similar form has been used in [27], where the growth of branched actin network is studied in order to investigate the effect of molecular transport on the force-velocity relation. Here, we do not apply any external force, rather we vary σ and κ in order to investigate the effect of these quantities on the force generation process.

The dynamics of the system is same as described in Chapter 3 and Chapter 4. The filaments grow and push the membrane while the membrane undergoes independent thermal fluctuations in its local height and tends to minimize its energy. The local height of the membrane can change with rates R_+ and R_- which satisfies the condition given in Eq. 3.2. We use $R_+ = e^{-\beta \Delta E}$ and $R_- = 1$. For $\Delta E = 0$, both the rates are taken to be unity.

The expression for ΔE at the i-th site can be written by using Eq. 5.1 as,

$$\Delta E_i^{\pm} = \sigma\{2d^2 \mp 2d(h_{i-1} - 2h_i + h_{i+1})\} + \kappa\{6d^2 \pm 2d(h_{i-2} - 4h_{i-1} + 6h_i - 4h_{i+1} + h_{i+2})\}$$

or,

$$\Delta E_i^{\pm} = \sigma\{2d^2 \mp 2dh_i''\} + \kappa\{6d^2 \pm 2dh_i''''\} = \Delta S_i^{\pm} + \Delta B_i^{\pm} \tag{5.2}$$

where, h_i'' and h_i'''' are second and fourth derivatives of height at the i-th site; $\Delta S_i^{\pm}$ and $\Delta B_i^{\pm}$ are the elastic and bending energy costs respectively. The sign $+$ $(-)$ corresponds to the energy cost when the height of i-th site, i.e., h_i increases (decreases) by one unit. We note that the elastic energy cost is proportional to the second derivative of height (h_i'') and the bending energy cost is proportional to the fourth derivative of height (h_i'''') (see Eq. 5.2). The simulation technique used here is also the same as the previous models.

In this section, we present our results for the single filament case. These results are quite general and also valid for multiple filaments with $N << L$. In our later sections, we will also discuss the case of multiple filaments.

5.3.1 *Non-monotonic variation in bending energy cost*

In sec. 5.1, we show that the qualitative shape of the membrane changes as the value of σ is changed, keeping κ at some moderate or large value. This effect gives rise to non-monotonic variation in fourth derivative of height at the binding site (h_b''''). Since the bending energy cost in order to push the membrane (ΔB_b^+), is related to h_b'''' by Eq. 5.2, ΔB_b^+ also shows non-monotonic variation with σ. We show these results in Fig. 5.2.

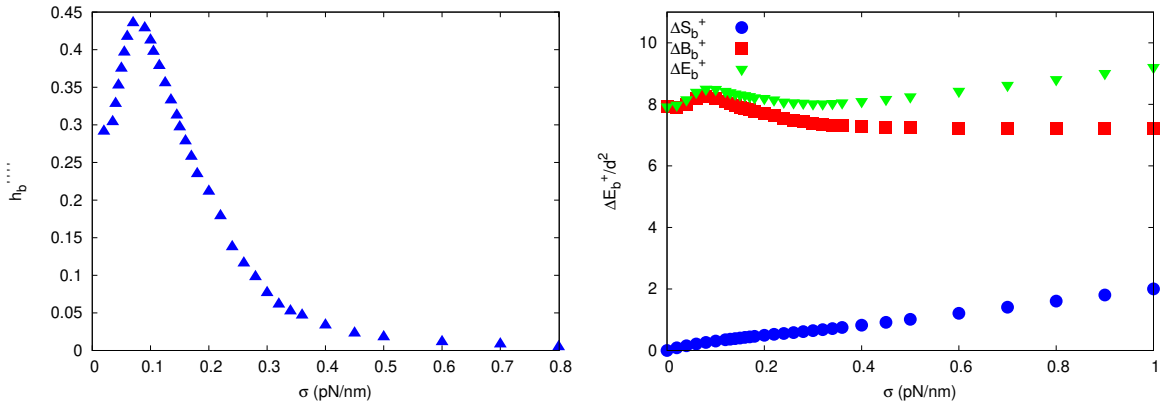

Figure 5.2: Energy cost of movement at the binding site. **(a):** The value of h_b'''' varies non-monotonically with σ for large κ. **(b):** For large κ, ΔE_b^+, which is the energy cost when the binding site increases by one unit, varies non-monotonically with σ. In the small σ region, the variation in ΔE_b^+ is mainly due to the variation in the bending energy cost ΔB_b^+, as the elastic energy cost is negligible. For large σ, on the other hand, the variation in ΔE_b^+ is mainly dominated by elastic energy cost ΔS_b^+, as the bending energy cost saturates for large σ. We use $L = 64$, $\kappa = 1.2pN$ and $\mathcal{S}/L = 1$ here. Other simulation parameters are as in Table 2.1.

The non-monotonic variation in h_b'''' is quite surprising, as one may expect the height derivatives to decrease with σ. This is because the height gradients are expected to decrease with σ in order to minimize the elastic energy, which means all the higher derivatives at the binding site should also decrease with σ, but we note that h_b'''' increases with σ in the small σ region. Here, we explain this interesting behaviour in detail. For large σ and κ, the shape of the membrane is such that all the derivatives (h_i', h_i'', etc.) are zero. When σ is decreased keeping κ large, it will develop small gradients in the system, but the shape will be such that the gradients (h_i') are same throughout the system with a peak in height at the site $i = b$,

which costs less energy [see Fig 5.1(c) and 5.1(d)]. In this case, the h''_b will be negative and will increase (in magnitude) as σ is decreased, while for other sites, h''_i will be zero [See Fig. 5.3(a)]. Now, if we assume a continuum surface of this kind, it is clear that the curvature of h''_i at $i = b$, which is nothing but h''''_b, will increase as σ is decreased. However, in the small σ region, the shape of the surface will deviate from the previous structure, and will take a shape where the gradients h'_i near the binding site will be less (in magnitude) than the gradient far from it [see Fig. 5.1(a) and 5.1(b)]. In such a situation, when σ is decreased, h''_i at the binding site will increase (in magnitude) slower that h''_i at some neighbourhood of binding site [see Fig. 5.3(b)]. Thus, h''''_b, which is the curvature of h''_i at $i = b$, will decrease as σ decreases in this case. In between, there will be a maximum of h''''_b. This explains why h''''_b will behave non-monotonically with σ for large κ.

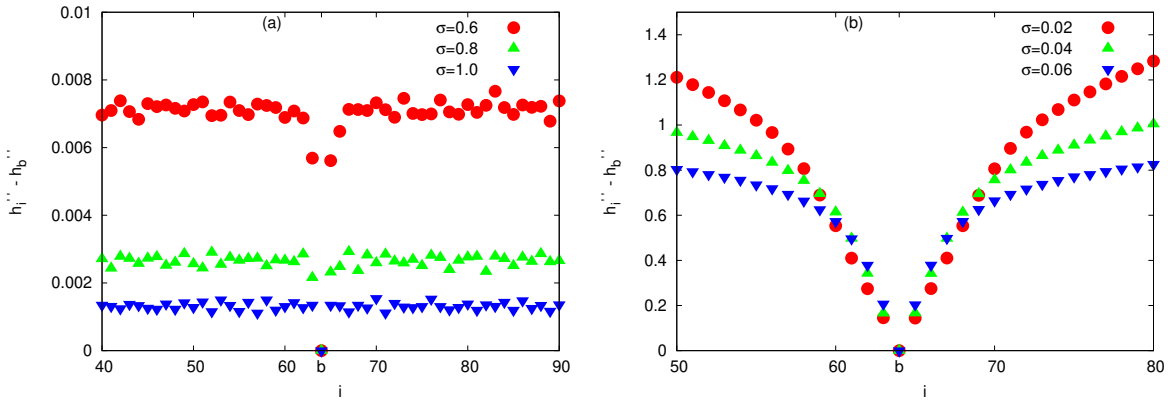

Figure 5.3: Variation of h''_i with i for different values of σ and large κ. In order to compare the curvatures of h''_i for different σ at the binding site, we subtract h''_b from it. **(a):** The quantity $h''_i - h''_b$ for different values of large σ. We note that when σ decreases, the curvature of h''_i at the binding site increases. Thus h''''_b will increase as σ decreases in this region. The values of h''_b for $\sigma = 0.6$, 0.8 and 1.0 pN are 6.97×10^{-3}, 2.60×10^{-3} and 1.30×10^{-3} (in units of d) respectively. **(b):** The quantity $h''_i - h''_b$ for different values of small σ. We note that the curvature of h''_i at $i = b$ decreases as σ decreases. Thus, in this region, h''''_b will decrease as σ will decrease. The values of h''_b for $\sigma = 0.02$, 0.04 and 0.06 pN are 1.17, 0.92 and 0.76 (in units of d) respectively. We use $L = 64$ ans $\mathcal{S}/L = 1$ here. Other simulation parameters are as in Table 2.1.

We also note that in Fig. 5.2, the bending energy cost saturates for large σ, since for such a large value of σ, all the height derivatives at h_b (h''_b, h''''_b) become negligible and bending energy cost becomes constant (see Eq. 5.2). In this region, the variation in the ΔE^+_b is mainly dominated by the variation is elastic energy cost, which increases linearly as $\sim 2d^2\sigma$. In the small σ region, on the other hand, the variation in total energy cost ΔE^+_b is mostly dominated by the bending energy cost. This is because κ is large and elastic energy cost is negligible for small σ. The bending energy cost itself varies non-monotonically, which gives rise to non-monotonic variation in ΔE^+_b in this region. Thus, we note that there is a range of σ value, for which the energy cost decreases when the value of σ increases. This rich interplay

between the elastic and bending energy scales gives rise to non-monotonic variation in the elasticity-velocity curves that we discuss in the next section.

5.3.2 *Membrane velocity varies non-monotonically with σ*

In our previous section, we note that there is an interplay between the elastic and bending energy scales in the system. For small σ, the variation in the bending energy cost ΔB_b^+ dominates while for large σ, the variation in the elastic energy cost ΔS_b^+ dominates. This effect has a direct consequence on the non-monotonic variation in the membrane velocity V. We measure V as a function of the elasticity (σ) for a given value of bending rigidity (κ). We note that for small κ, the velocity falls monotonically with σ and $\sigma - V$ curves are convex. However, for κ not too small, the velocity shows interesting non-monotonic variation with σ [Fig. 5.4(a)]. We note that the velocity first decreases with σ, then increases and reaches a peak at $\sigma = \sigma^*$ and finally decreases again with σ (Fig. 5.4(a), top right inset). The peak position of the $\sigma - V$ curve shifts towards small σ, as the value of κ increases (Fig. 5.4(a), top left inset). Below, we explain these results.

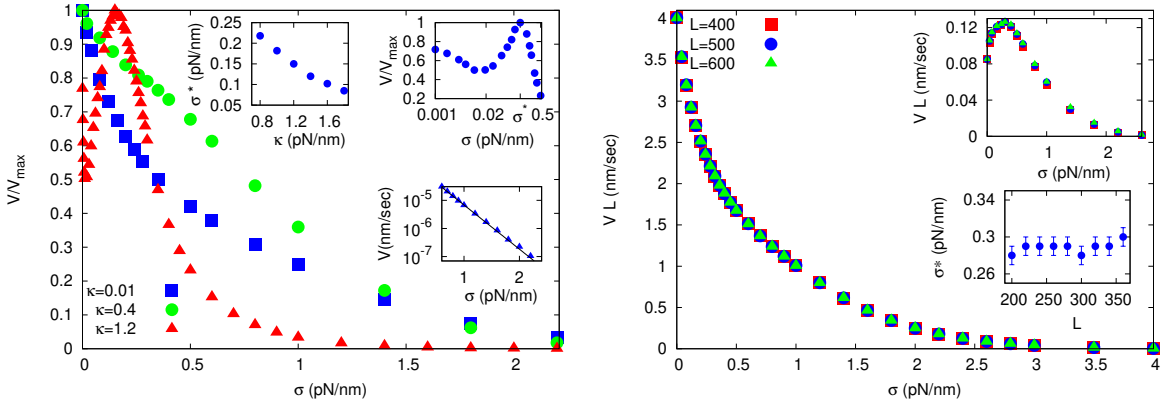

Figure 5.4: $\sigma - V$ curve for different values of κ and L. **(a):** For small value of κ, the velocity falls monotonically with σ and the $\sigma - V$ curves are convex. For large value of κ, the curve becomes non-monotonic, with a peak at $\sigma = \sigma^*$. **Top left inset:** The value of σ^* decreases with κ. **Top right inset:** We zoom small σ region and note that V first decreases, reaches a minima, then increases and reaches a peak value at $\sigma = \sigma^*$, then decreases again with σ. **Bottom inset:** For very large σ, velocity falls exponentially with decay factor 3.6 which is close to the analytically predicted value $2\beta d^2$. For top right and bottom insets, we use $\kappa = 1.2pN$. For all the plots, we use $L = 64$ and $\mathcal{S}/L = 1$. **(b):** For small value of $\kappa(= 0.01pN)$, the velocity scales as $1/L$. **Top inset:** For large value of $\kappa(= 0.8pN)$ also, the velocity scales with $1/L$. **Bottom inset:** The value of σ^* remains independent of L. Here, we use $\mathcal{S}/L = 1$. Other simulation parameters are as in Table 2.1.

The expression for the velocity at the binding site can be written as,

$$V_b = U_0 p_0 e^{-\beta \Delta E_b^+} + e^{-\beta \Delta E_b^+} - (1 - p_0) e^{-\beta \Delta E_b^-} \tag{5.3}$$

where p_0 is the contact probability of the filament tip with the membrane. The first term in Eq. 5.3 corresponds to the bound filament polymerization, the second and third terms are for independent upward and downward movement of the binding site respectively. As, the downward movement happens only when there is no filament in contact with the membrane, a factor $(1 - p_0)$ is multiplied with the downward movement. For large κ, both the $\Delta E_b^{\pm}$ are positive as the height derivatives (h_b'', h_b'''' etc.) are smaller in comparison to other terms (see Eq. 5.2). Thus, for both the upward and downward movements, the energy is increasing, and each process will occur with rate $R_+ = e^{-\Delta E_b^{\pm}}$ in this region. We note that the value of p_0 is $\simeq 0.5$ for any σ if $\mathcal{S}/L$ is not too large (Fig. 5.5(a), inset). This is because an introduction of κ makes the membrane rigid enough, and we have shown in our chapter 3 that for a rigid barrier, $p_0 = 1 - W_0/U_0 \simeq 0.5$ [70]. Note that the expression for average velocity V is the same as V_b, as the system is in the steady state, which means the velocity of all the sites are same. For large κ and small σ, we can neglect the elastic energy cost. Using the value of $\Delta E_b^{\pm}$ and neglecting the terms containing σ, the expression for V turns out to be,

$$V \simeq e^{-6\beta d^2\kappa}\{(U_0+1)p_0 e^{-2\beta d\kappa h_b''''} - 2(1-p_0)Sinh(2\beta d\kappa h_b'''')\}$$

In the above expression, only h_b'''' shows a variation with σ and all other terms are constant. Since $Sinh(x)$ is a monotonically increasing function of x, an increase in h_b'''' will cause a decrease in V and vice versa. Since, h_b'''' increases first and then decreases in the small σ region, V will first decrease and reach a minima, then will increase again. Thus, we note that there is a range of σ for which the velocity of the membrane increases with σ. When σ becomes large, the terms in Eq. 5.3, that contain elastic tension is no longer negligible. In this case, however, the terms containing height derivatives at h_b (h_b'', h_b'''' etc.) becomes negligible and can be neglected in the expression of V. The V (Eq. 5.3) then will have the form,

$$V \simeq (U_0+1)p_0 e^{-6\beta d^2\kappa} e^{-2\beta d^2\sigma}$$

Thus, in this region, V will fall exponentially as a function of σ. We indeed note an exponential fall of velocity in this region. The exponential decay factor in this case is $2\beta d^2 \simeq 3.52$ which is close to the numerically observed value 3.6 (Fig. 5.4(a), bottom inset). Thus, we explain above, why the velocity of the membrane will have non-monotonic variation with σ for large κ. We also note that the peak in the $\sigma - V$ curve corresponds to the region where the height derivatives (h_b'', h_b'''' etc.) becomes negligible. In this region, the bending energy cost saturates and the elastic energy cost increases linearly with σ, which causes the velocity to fall exponentially with σ. Larger the value of κ, smaller will be the value of σ, where the height derivatives become negligible. This explains why the value of σ^* will decrease with κ (Fig. 5.4(a), top left inset). For small κ, the energy cost $\Delta E_b^{\pm}$ does not show any non-

monotonic variation, rather it increases monotonically with σ (data not shown). In a similar way as above, we can explain that in this case V will also fall monotonically with σ.

Next, we measure $\sigma - V$ curves for different values of L. We note that $\sigma - V$ curves collapse for different L if we scale velocity by $1/L$, for both the small and large κ [Fig. 5.4(b)]. The explanation for this $1/L$ scaling is same as for the gradient model or the Gaussian model. Since, velocity scales with $1/L$, it is expected that the value of σ^* (for large κ) will also be independent of L. We plot σ^* as a function of L in Fig. 5.4(b), bottom inset and explicitly show this.

5.3.3 *Faster membrane dynamics lowers σ^**

We plot $\sigma - V$ curves for different values of $\mathcal{S}/L$ in Fig. 5.5. We note that for small κ, the $\sigma - V$ curves become concave when $\mathcal{S}/L$ becomes very large [Fig. 5.5(a)]. We also note that the p_0 also becomes very small in the small σ region for faster barrier dynamics (Fig. 5.5(a), inset). The explanation for this effect is similar to the gradient or the Gaussian model. For large κ, on the other hand, we note that the shape of the $\sigma - V$ curves remain non-monotonic [Fig. 5.5(b)]. The peak position of the velocity shifts towards smaller σ with $\mathcal{S}/L$ (Fig. 5.5(b), inset). We can explain the shift of the peak position of velocity (or σ^*) with $\mathcal{S}/L$ in the following way. In our previous section, we explain that the peak in the velocity arises at some value of $\sigma = \sigma^*$, at which the height derivatives (h_b'', h_b'''' etc.) become negligible. For smaller value of $\mathcal{S}/L$, the membrane sites can not fluctuate much. Thus, once the filament pushes the binding site, the height gradient at the binding site persists for much longer time. Thus the average value of height gradient will be higher in this case for a given σ. Thus, the value of σ at which the height derivatives become negligible, will also increase, which increases σ^*. On the other hand, for large $\mathcal{S}/L$, the bulk sites quickly catch up with the binding site and thus the height gradient at the binding site quickly disappears. Thus, the value of σ^* will be smaller in this case. Thus, the value of σ^* will decrease with $\mathcal{S}/L$.

5.3.4 *$\kappa - V$ curves are monotonic for any σ*

In our earlier sections, we measure the velocity of the membrane as a function of σ, with the value of κ held fixed. In this section, we measure velocity as a function of κ keeping the value of σ fixed. We note that the velocity falls monotonically with κ, even for large σ [see Fig. 5.6(a)]. In this case, we note that the energy cost at the binding site, i.e., ΔE_b^+ increases monotonically with κ even for large σ [Fig. 5.6(b)]. Thus, we do not find any non-monotonicity in velocity here. This observation can be explained as follows. For large σ, a small height gradient will cause very high elastic energy, since each site of the membrane

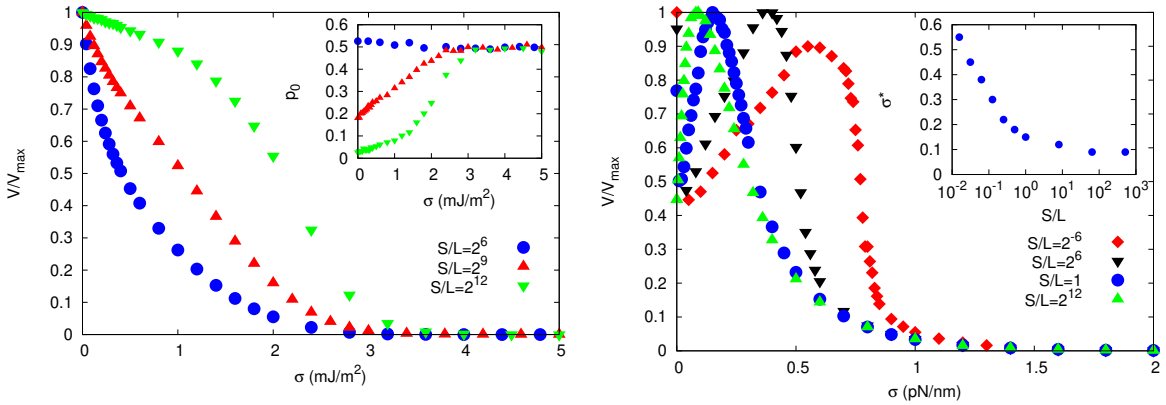

Figure 5.5: $\sigma - V$ curves for different values of $\mathcal{S}/L$. **(a):** $\sigma - V$ curves for small κ and different $\mathcal{S}/L$. For small $\mathcal{S}/L$, the curves are convex, while for $\mathcal{S}/L >> 1$, the curves become concave. **Inset:** The contact probability p_0 is close to 0.5, when the value of $\mathcal{S}/L$ is not too large, however, for very large $\mathcal{S}/L$, p_0 becomes negligible in the small σ. **(b):** $\sigma - V$ curves for large κ and different $\mathcal{S}/L$. The curves are non-monotonic, but the peak position (σ^*) shifts towards smaller σ as $\mathcal{S}/L$ increases. **Inset:** The value of σ^* decreases with $\mathcal{S}/L$. We use $L = 64$ here.

will have an elastic energy. Thus, for large σ, the height derivatives (h_b', h_b'' etc.) at the binding site become negligible even for very small κ. Thus, the variation in ΔE_b^+ is only due to the variation in bending energy cost, while the elastic energy cost saturates at the beginning and will not show any variation with κ. For small σ, the elastic energy cost will be negligible and the variation in the bending energy cost will dominate. Thus, for any value of σ, the variation in the beading energy cost will dominate over the elastic energy cost. Thus, ΔE_b^+ will increase monotonically with κ and the velocity will decrease with κ. We also note that velocity scales as $1/L$ similar to the previous case (Fig. 5.6(a), inset).

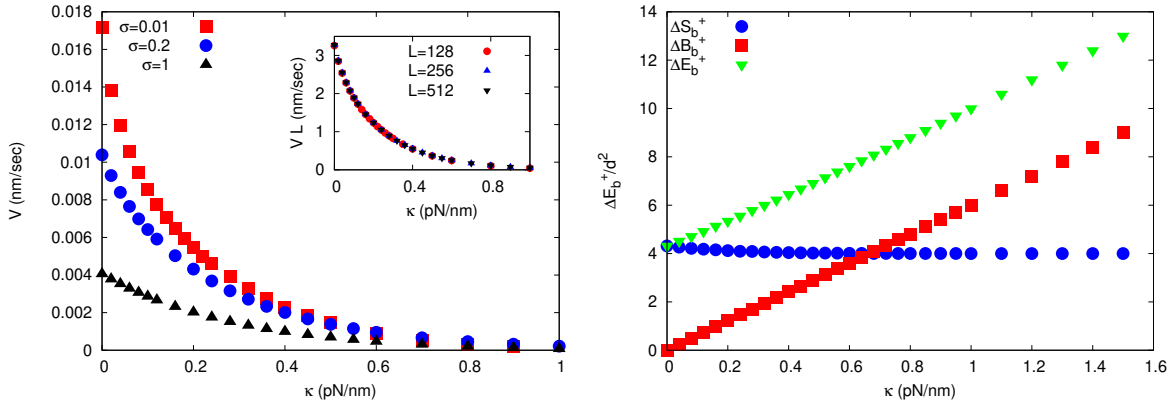

Figure 5.6: $\kappa - V$ curves for different values of σ. **(a):** The $\kappa - V$ curves are monotonic for any value of σ. Here, we use $L = 256$. **Inset:** The velocity scales as $1/L$, similar to the $\sigma - V$ curves. **(b):** ΔE_b^+ for large σ ($= 2pN$) as a function of κ. We note that ΔE_b^+ increases monotonically with κ. For all the plots, we use $\mathcal{S}/L = 1$. Other simulation parameters are as in Table 2.1.

In all the above cases, we take the membrane size $L >> 1$. However, for small L, we note that there are finite size effects. For small value of L, the $\sigma - V$ curves or $\kappa - V$ curves do not scale with $1/L$ (data not shown). The value of σ^* is also found to increase with L and then saturates for very large L (data not shown).

5.4 RESULTS FOR MULTIPLE FILAMENTS

So far, we have considered the case of single filament. In this section we will present a brief discussion on multiple filaments. We define the filament density as $\rho = N/L$. We first discuss the case of small filament density, i.e., $\rho << 1$. Then we will also discuss the case of $\rho \sim 1$.

5.4.1 *For $N \ll L$, the qualitative behaviour remains same as the single filament*

For $\rho \ll 1$, we note that the qualitative behavior of the system remains same as that for the single filament case. In Fig. 5.7(a), we plot the $\sigma - V$ curves for multiple filaments with small ρ for a given value of κ. We note that similar to the single filament case, $\sigma - V$ curve is monotonic for small κ while it shows non-monotonic variation for large κ, with a peak value of V at $\sigma = \sigma^*$. The value of σ^* is also found to decrease with κ (Fig. 5.7(a), inset). We note that V scales as ρ for both the small as well as large κ [Fig. 5.7(b)]. Thus, the value of σ^* should also be independent of ρ. We plot σ^* as a function of ρ in Fig. 5.7(b), bottom inset and explicitly show this. We also note that for small κ, the $\sigma - V$ curve changes from convex to concave for $\mathcal{S}/L >> 1$ (data not shown). The $\kappa - V$ curves are monotonic for any σ, similar to the single filament case (data not shown).

5.4.2 *For $N \sim L$, σ^* depends explicitly upon N and L*

In the previous section, we discuss the case of multiple filaments with very small filament density, such that there are no interaction between the filaments. However, as ρ increases, the filaments are no longer non-interacting and the single filament picture does not remain valid in this case. Our data in Fig. 5.8 show that $V \sim \rho$ scaling is lost and σ^* is no longer independent of ρ. We note that σ^* decreases with ρ for a given L. For a given ρ, σ^* increases with L (or N). Thus, σ^* is not only a function of ρ rather explicitly depends upon N or L also. We explain this effect below. For a given L, when we increase N (or ρ), the filaments are very close to each other. In such a situation, a bulk site will feel more upward pull due to the presence of binding sites very close to it. Thus, the membrane will become flat and the magnitude of height gradients will decrease. Thus, for a given σ, higher ρ will have smaller value of height derivatives (h_b'', h_b'''' etc.). Thus, σ^*, at which the height derivatives become

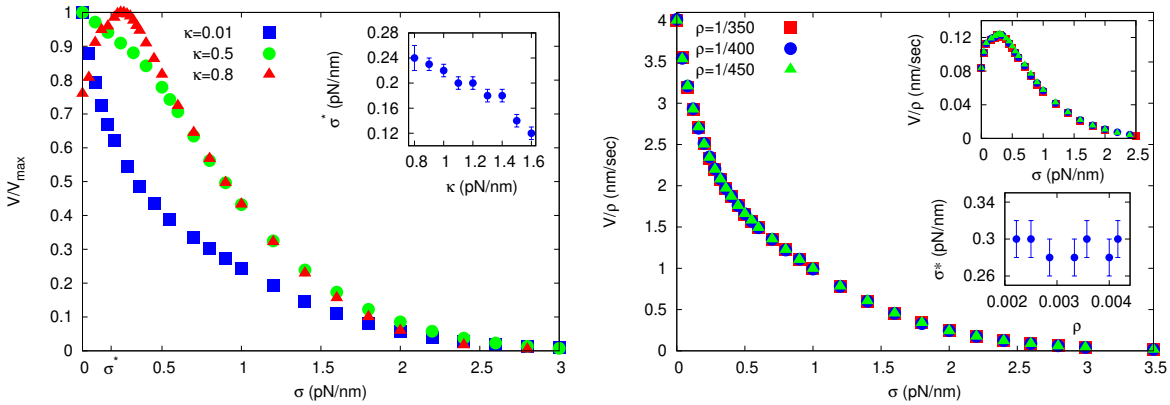

Figure 5.7: Results for multiple filaments with $\rho << 1$. **(a):** $\sigma - V$ curves for different values of κ. The velocity falls monotonically for small κ, while vary non-monotonically for large κ, with a peak at $\sigma = \sigma^*$. **Inset:** The value of σ^* decreases with κ. Here, we use $\rho = 1/128$. **(b):** $\sigma - V$ curves for different ρ and small κ ($= 0.01pN$). We note that velocity scales with ρ. **Top inset:** $\sigma - V$ curves, for different ρ for large κ ($= 0.8pN$). In this case also, V scales with ρ. **Bottom inset:** σ^* remains independent of ρ. We use $\mathcal{S}/L = 1$ here. Other simulation parameters are as in Table 2.1.

negligible, will decrease with ρ for a given L. We show this explicitly in Fig. 5.8(b). On the other hand, for a given ρ, when N (or L) is increased, the height derivative increases [Fig. 5.8(b)]. Thus, the height derivatives become negligible at higher value of σ, which increases σ^*.

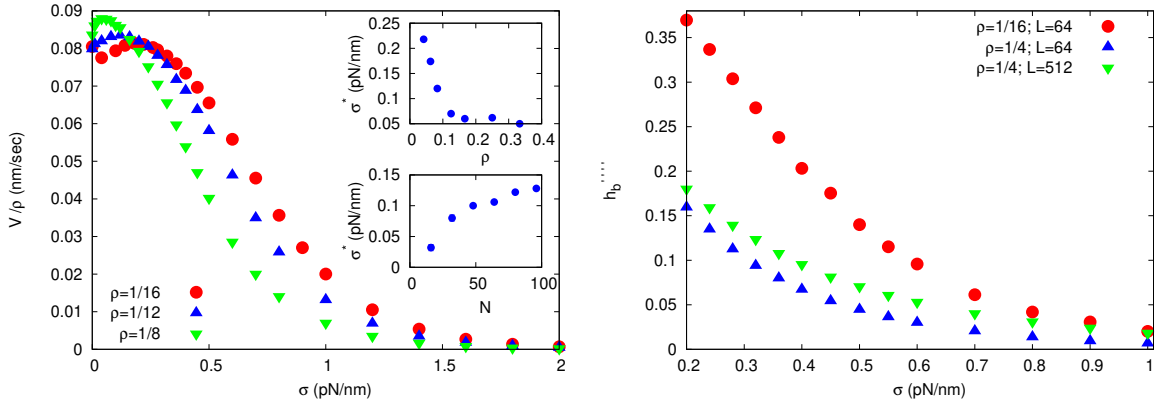

Figure 5.8: Results for multiple filaments with $\rho \sim 1$. **(a):** $\sigma - V$ curves for different values of ρ for a given large κ ($= 0.8pN$). The velocity does not scale with ρ. **Top inset:** The value of σ^* decreases with ρ. **Bottom inset:** For a given ρ ($= 1/4$), the σ^* increases with N (or L). Thus, σ^* explicitly depends upon ρ as well as N (or L). **(b):** h_b'''' as a function of σ for different values of ρ and L. We note that the value of h_b'''' is higher if ρ is smaller (for a given L) or if L is larger (for a given ρ). Thus, the value of σ, at which h_b'''' will be negligible, will be smaller for either larger ρ (for a given L) or smaller L (for a given ρ). We use $\mathcal{S}/L = 1$ here. Other simulation parameters are as in Table 2.1.

In this chapter, we study the force generation by parallel actin filaments growing against a membrane whose energy is described by the Helfrich Hamiltonian. The Hamiltonian contains an elastic energy term, being proportional to the square of height gradients and a bending energy term which is proportional to the square of the Laplacian of height. We note that the shape of the membrane changes qualitatively when we change the value of elasticity (σ) keeping the bending rigidity (κ) fixed. This effect gives rise to a non-monotonic variation in the bending energy cost in order to push the membrane. We also note that there is a rich interplay between the elastic and bending energy scales in the system, as a consequence, the elasticity-velocity curves show non-monotonic variation for moderate or large value of κ. The velocity first decreases with σ and reaches a minima, then increases with σ and reaches a peak at $\sigma = \sigma^*$ and then again decreases with σ for large σ values. We also note that the peak position of the curve (σ^*) shifts towards the smaller elasticity as the bending rigidity is increased. The value of σ^* is found to be independent of membrane size (L) for single filament. For multiple filaments with small filament density, σ^* is independent of the filament density, however, for large filament density, σ^* explicitly depends upon the filament density as well as the size of the membrane. For small κ, the shape of $\sigma - V$ curve changes from convex to concave when the membrane dynamics becomes faster. For large κ, however, the $\sigma - V$ curve remains non-monotonic even for faster membrane dynamics. The value of σ^* decreases as the membrane dynamics becomes faster in this case. We also note that $\kappa - V$ curves are monotonic for any value of σ, and we do not observe any non-monotonicity here.

In our previous chapters (Chapter 3 and 4), a similar model has been studied, where the energy of the membrane is described by only its elastic energy and bending energy has been neglected. We note that for the Gaussian model, the velocity falls monotonically with the elastic tension for any non-zero value of elastic tension. For the present case, introduction of bending rigidity changes the qualitative nature of the results. The non-monotonic variation of velocity is also seen for the gradient model, but the origin of this effect is different from the present case. For the gradient model, the non-monotonicity arises due to the competition between the elastic force of the membrane and the polymerization force of the filament, with a peak in velocity where the two forces become equal. For the present case, however, it arises due to the interplay between the elastic and bending energy scales. Unlike gradient model, where the system does not have a steady state for small elastic tension, here we have steady state throughout for any non-zero σ or κ.

Finally, within simple modelling of force generation by parallel actin filaments against a membrane, we are able to show many interesting effects by varying its bending rigidity and elastic tension. There are a number of experiments, where the effect of elastic tension on the

force generation mechanism have been studied [39–41]. There are some experiments, where the bending rigidity of the cell membrane have been measured [42–46], but the effect of bending rigidity on the force generation mechanism have not been addressed. Our simple study may open up the possibility to observe some of these effects in experiments.

6

COMPARISON BETWEEN TWO TYPES OF FILAMENT-BARRIER INTERACTIONS

6.1 INTRODUCTION

In our earlier chapters (Chapters 2 to 5), we have studied force generation by actin filaments growing against a barrier, considering its shape fluctuations, its elastic properties, bending rigidity etc. In all these models, the filament-barrier interactions are such that a filament can always grow and push the barrier even if it is in contact with the barrier. Such models are also studied in [17–19, 23, 65, 77]. There are another class of models, where it is assumed that a filament can only grow when there is sufficient gap between the filament tip and the barrier [13, 25, 31, 48, 49]. While the models discussed above vary in many aspects, the interaction between the growing end of the filament and the barrier can be roughly classified in the above two types. Although the difference between the two mechanisms seems to be microscopic and rather a matter of modelling details, we find that the force generation properties are significantly different in the two cases. Interestingly, this difference persists even in absence of shape fluctuations of the barrier, when the barrier is modelled like a rigid wall. In this chapter, we will discussed some important qualitative differences between these two types of filament-barrier interactions, which has not been addressed in earlier literatures, to the best of our knowledge.

For ease of nomenclature, we denote the two cases by type A and type B, where type A stands for those models where filaments can actively push the barrier and grow, and type B represents those models where the filaments can grow only if there is sufficient gap between the filament tip and the barrier to insert one monomer. We demonstrate the difference between type A and B models for three different types of barrier: A rigid wall-like barrier, a barrier with Kardar-Parisi-Zhang dynamics which is studied in Chapter 2 and an elastic barrier which is studied in Chapter 3. We note that the main differences between type A and B models are manifested in the way various properties depend on the relative time-scale $\mathcal{S}$ between the filament and barrier dynamics.

For a rigid barrier with a type A interaction with the filaments, we find the shape of force-velocity curve is always concave when there are multiple filaments present in the system. On the other hand, for a single filament, the force velocity curve is convex (concave) when the thermal fluctuations of the rigid barrier position are much slower (faster) than the filament dynamics. For type B interaction, the force-velocity curve for multiple filaments shows convex (concave) shape for slower (faster) barrier dynamics, but for a single filament the shape does not depend on the time-scale. Even at zero force, the velocity V_0 of the barrier for the two types show different behavior. While for type A interaction, V_0 is independent of the time-scale of barrier dynamics, for type B interaction, V_0 increases as the barrier dynamics becomes faster. The stall force F_s decreases for type A as the barrier dynamics becomes faster, but remains constant for type B. As the number of filaments in the system becomes larger, F_s also increases. Our analytical calculations show that for type B, stall force scales linearly with the number of filaments, while for type A, there is a logarithmic correction to linear scaling. For the KPZ barrier with type A interaction (Chapter 2), F_s decreases as the barrier dynamics becomes faster, but remains constant for type B. For an elastic barrier with type A interactions (Chapter 3), we note that μ^* decreases with $\mathcal{S}/L$ and for very slow barrier dynamics, it yields a monotonically decreasing convex $\mu - V$ curve. For type B, on the other hand, μ^* remains same for a wide range of the barrier movement time-scale and the shape of the $\mu - V$ curve remains non-monotonic. However, in the limit when the barrier motion becomes very fast, both the models show concave $\mu - V$ curves. Some of the results discussed above have been published in [78].

This chapter is organized as follows. In Sec. 6.2 we present our results for the rigid barrier model, in Sec. 6.3 we discuss KPZ barrier model, in Sec. 6.4 we discuss elastic barrier model and finally present our conclusions in Sec. 6.5.

6.2 RIGID BARRIER MODEL

In this model, the barrier is described as a one dimensional rigid and movable wall. Under the action of an external force F, the wall tends to move downward. Thermal fluctuations can also move the barrier in the upward direction, but such movements come with an energy cost. Let R_+ and R_- be the upward and downward movement rates for the barrier by a discrete amount d [Fig. 6.1(b)]. These rates satisfy local detailed balance, and we choose $R_+ = e^{-\beta F d}$ and $R_- = 1$. Any downward movement of the barrier that brings it below any filament tip, is forbidden.

The filaments are modelled as rigid rod-like objects, same as previous chapters. For simplicity, we throughout assume the length of the monomer is same as d, the step of barrier movement. For type A mechanism, a bound filament can grow by pushing the barrier up-

ward by an amount d and thereby performing work Fd against the external force [Fig. 6.1(c)]. The rate of such a process is $U_0 e^{-\beta F d}$. For type B mechanism, on the other hand, the bound filament polymerization is not allowed and one must wait until thermal motion takes the barrier upward and a gap of length d is created between the filament tip and the barrier. Fig. 6.1 summarizes our model schematically.

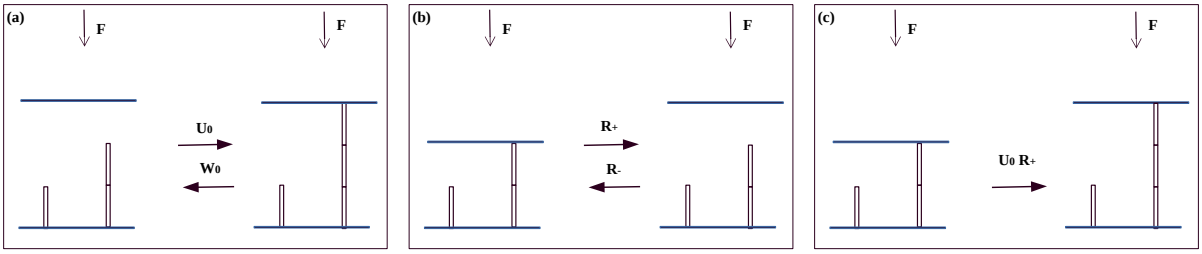

Figure 6.1: Schematic representation of rigid barrier model. **(a):** A free filament polymerizes (depolymerizes) with rate U_0 (W_0). **(b):** The barrier height undergoes thermal fluctuations. In presence of the external force F, the forward process which increases the height is energetically costly and happens with rate R_+ while the reverse process that decreases the height is energetically favourable and happens with rate R_-. **(c):** A bound filament pushes the barrier by an amount d that costs energy and occurs with rate $U_0 R_+$. This movement is allowed only for type A.

We perform simulations using kinetic Monte Carlo (MC) technique as described in our earlier chapters. The relative time-scale between the filament dynamics and the barrier dynamics is quantified by a parameter $\mathcal{S}$. For a system having N number of filaments, each Monte Carlo time-step consists of N filament updates and $\mathcal{S}$ independent barrier updates. Starting from an initial condition of all filaments of length d (*i.e.* each filament consists of only one monomer) and the barrier is also at a height d, in contact with all filament tips, the system undergoes time-evolution and after a large number of Monte Carlo steps, when the system reaches steady state, we perform our measurements. The various simulation parameters are given in Table 2.1.

In the rest of this section, we present our results focussing on the major differences observed between type A and B models. We first present the results for single filament. Then we discuss the multiple filaments case. A rigid barrier with both the type A and B interactions have been widely studied in [13, 17, 19, 23, 31, 48, 49], but the effect of relative time scale between the filament and the barrier dynamics is not addressed in most of the cases. We find that the relative time scale plays an important role, and brings out the difference between type A and B models.

6.2.1 *Variation of V_0 with $\mathcal{S}$ for single filament*

The velocity of the barrier is measured as its average displacement per MC step. In the absence of any external force, the barrier velocity is denoted as V_0. The contact probability

p_0 can be calculated in a similar way as done in earlier chapters. Let p_i be the probability that there is a gap of size i between the barrier and the filament tip. The contact probability p_0 thus corresponds to $i = 0$. The master equation for p_i can be written as

$$\frac{dp_i}{dt} = (U_0 + \mathcal{S})p_{i+1} + (W_0 + \mathcal{S}e^{-\beta Fd})p_{i-1} - (U_0 + \mathcal{S} + W_0 + \mathcal{S}e^{-\beta Fd})p_i; \quad for\ i > 0$$

and

$$\frac{dp_0}{dt} = (U_0 + \mathcal{S})p_1 - (W_0 + \mathcal{S}e^{-\beta Fd})p_0; \quad for\ i = 0$$

where all symbols have their usual meaning. The above equations are valid for both the types A and B, as the bound filament polymerization does not change p_i. In the steady state, one has the recursion relation $p_i = (\frac{\mathcal{S}e^{-\beta Fd}+W_0}{\mathcal{S}+U_0})^i p_0$; which by applying normalization condition gives the expression for the contact probability,

$$p_0 = \frac{U_0 - W_0 + \mathcal{S}(1 - e^{-\beta Fd})}{U_0 + \mathcal{S}} \tag{6.1}$$

which holds for both type A and type B dynamics.

Eq. 6.1 can also be derived in a slightly different way. We present this alternative derivation here. Since the barrier is being driven by the growing filament, its velocity must be same as the growth velocity of the filament. The velocity of the filament, for type A is simply $\{U_0 p_0 e^{-\beta Fd} + U_0(1 - p_0) - W_0\}$, while the velocity of the barrier has the form $\{U_0 p_0 e^{-\beta Fd} + \mathcal{S}e^{-\beta Fd} - \mathcal{S}(1 - p_0)\}$. Equating these two for type A, gives the same expression for p_0 as in Eq. 6.1. For type B, the velocity of the filament is simply $\{U_0(1 - p_0) - W_0\}$, while the velocity of the barrier is $\{\mathcal{S}e^{-\beta Fd} - \mathcal{S}(1 - p_0)\}$. Equating these two also gives the same result for p_0 as in Eq. 6.1.

For $F = 0$, using Eq. 6.1, we have $p_0 = (U_0 - W_0)/(U_0 + \mathcal{S})$. Now, for type A model, V_0 can be written as a sum of three terms:

$$V_0 = d\{p_0 U_0 + \mathcal{S} - \mathcal{S}(1 - p_0)\} \tag{6.2}$$

Here, the first term corresponds to the velocity imparted by bound filament polymerization, which occurs with rate U_0 for $F = 0$. The second and third terms are for upward and downward thermal fluctuations of the barrier, which take place on an average $\mathcal{S}$ times in one MC step. The factor $(1 - p_0)$ ensures that the filament is not bound to the barrier, blocking its downward movement. Substituting the expression for p_0, we get the velocity of the barrier for type A model as $V_0 = d(U_0 - W_0)$ which is independent of $\mathcal{S}$ [70]. The value of V_0 in this case is simply the maximum velocity of the filament, since the bound filament is able to grow freely in the absence of any opposing force. For type B case, bound filament polymerization

is not allowed and hence the first term in the expression for V_0 will not be there, which gives $V_0 = \frac{d(U_0 - W_0)}{1 + \frac{U_0}{\mathcal{S}}}$, which depends on $\mathcal{S}$. The filament in this case still feels the presence of the barrier and as $\mathcal{S}$ increases, free space is created more often above the filament tip which increases growth speed and hence V_0. In the limit of very large $\mathcal{S}$, we have same V_0 for type A and B. We compare these results with the numerics in Fig. 6.2 which shows very good agreement.

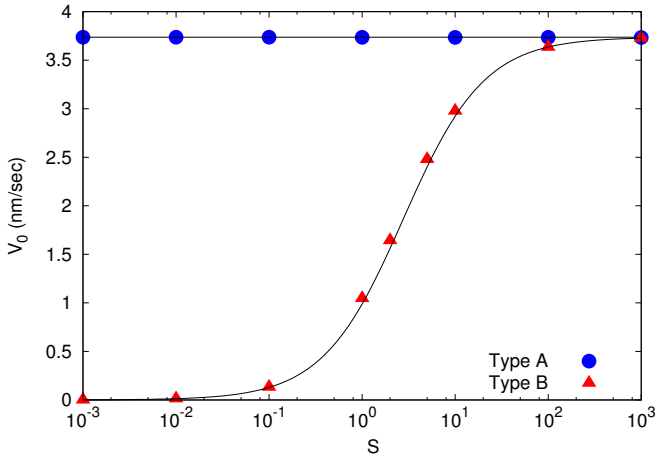

Figure 6.2: V_0 as a function of $\mathcal{S}$ for rigid barrier. For type A, V_0 remains constant at the value $d(U_0 - W_0)$ for a wide range of $\mathcal{S}$. For type B, V_0 increases with $\mathcal{S}$ and then saturates to a value $d(U_0 - W_0)$. The continuous lines show the analytical predictions and discrete points are from numerical simulations. Simulation parameters are as in Table 2.1.

6.2.2 *Force-velocity curves with different $\mathcal{S}$ for single filament*

In presence of non-zero external force F, the velocity of the barrier is expected to decrease with F. In Fig. 6.3 we plot the force-velocity curve for type A and type B models for different values of $\mathcal{S}$. For the ease of comparison, we have plotted both curves using rescaled velocity V/V_0 and rescaled force F/F_s. The left panel is for type A and this plot shows that the force-velocity curve is convex for $\mathcal{S} \ll 1$ and becomes concave for large $\mathcal{S}$ [31]. However, for type B model, our data in Fig. 6.3(b) show that the force-velocity curve does not change shape with $\mathcal{S}$. In fact all the curves for different values of $\mathcal{S}$ fall on top of each other. We explain this observation below by analytically calculating V as a function of F.

For type A systems, the Eq. 6.2 changes to $V(F) = d\{p_0 U_0 e^{-\beta F d} + \mathcal{S} e^{-\beta F d} - \mathcal{S}(1 - p_0)\}$ in presence of external force F. Using the expression for p_0 from Eq. 6.1 we get

$$V(F) = d\left[\frac{(U_0 e^{-\beta F d} + \mathcal{S})\{U_0 - W_0 + \mathcal{S}(1 - e^{-\beta F d})\}}{(U_0 + \mathcal{S})} - \mathcal{S}(1 - e^{-\beta F d})\right] \tag{6.3}$$

In the limit of $\mathcal{S} \ll 1$, above equation becomes $V(F) \simeq d(U_0 - W_0)e^{-\beta F d}$. Thus, for $\mathcal{S} \ll 1$, the velocity drops exponentially with force which gives rise to a convex shape. On the other hand, in the limit of small F the right hand side of Eq. 6.3 becomes $d(U_0 - W_0)\left(1 - \frac{U_0 \beta d}{U_0 + \mathcal{S}} F\right)$ and for $\mathcal{S} \gg 1$ we have $V \simeq d(U_0 - W_0)$, which is independent of F. Thus for large $\mathcal{S}$ the velocity remains almost constant for small force and decreases for large force, which indicates a concave curve.

For type B, since filaments cannot push the barrier, velocity has the form $V(F) = d\{\mathcal{S}e^{-\beta F d} - \mathcal{S}(1 - p_0)\}$, which after putting the value of p_0 becomes,

$$V(F) = \frac{d\{(U_0 - W_0) - U_0(1 - e^{-\beta F d})\}}{1 + \frac{U_0}{\mathcal{S}}} \tag{6.4}$$

and if we scale the velocity by V_0, then we have, $\frac{V(F)}{V_0} = \frac{U_0 e^{-\beta F d} - W_0}{U_0 - W_0}$ which is independent of $\mathcal{S}$. Thus, the shape of the force-velocity curve does not depend on $\mathcal{S}$ in this case. The analytical calculations for $V(F)$ agree well with the numerics in Fig. 6.3.

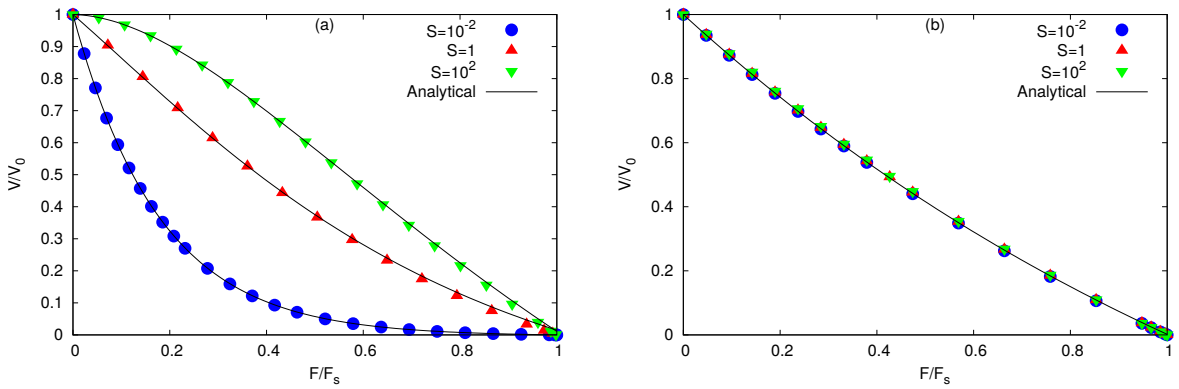

Figure 6.3: $F - V$ curves for different values of $\mathcal{S}$ for rigid barrier. **(a)** Type A: We plot the velocity of the barrier as a function of the scaled force F/F_s. We note that the force-velocity curve changes its nature with $\mathcal{S}$. For $\mathcal{S} << 1$, the curve is convex which changes to concave for $\mathcal{S} >> 1$. **(b)** Type B: We plot the scaled velocity V/V_0 as a function of F. In this case, unlike type A, the shape of the force velocity curve is independent of $\mathcal{S}$. Simulation parameters are as in Table 2.1.

6.2.3 *Stall force as a function of $\mathcal{S}$ for single filament*

The analytical expression for F_s for type A can be obtained by simply putting the left hand side of Eq. 6.3 zero and solving for F. This gives a quadratic equation

$$U_0 \mathcal{S} x^2 - U_0(U_0 - W_0 + 2\mathcal{S})x + \mathcal{S}W_0 = 0$$

where $x = e^{-\beta F_s d}$. This allows only one physical solution for x and we get

$$F_s = -\frac{1}{\beta d} ln \left[\left(\frac{U_0 - W_0 + 2\mathcal{S}}{2\mathcal{S}} \right) \left(1 - \sqrt{1 - \frac{4U_0 W_0 \mathcal{S}^2}{U_0^2 (U_0 - W_0 + 2\mathcal{S})^2}} \right) \right] \tag{6.5}$$

In Fig. 6.4 we verify this against numerical data. As seen in this plot, the stall force decreases with $\mathcal{S}$ and saturates to a non-zero value for large $\mathcal{S}$. For type B model, on the other hand, the stall force is independent of $\mathcal{S}$, as seen from putting the left hand side of Eq. 6.4 zero and finding $F_s = \frac{1}{\beta d} ln \frac{U_0}{W_0}$. The expression for F_s in this case also matches well with the numerics (Fig. 6.4).

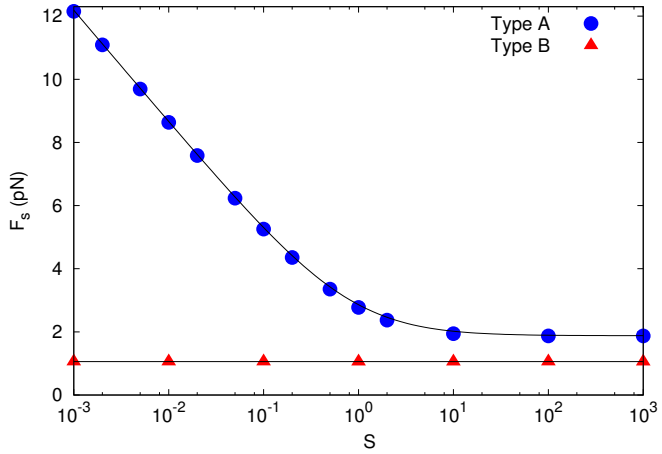

Figure 6.4: F_s as a function of $\mathcal{S}$ for rigid barrier. For type A, F_s decreases as the barrier dynamics becomes faster. For very large $\mathcal{S}$, F_s is found to saturate to a value 1.87 which is close to the analytical prediction of $F_s(\mathcal{S} \to \infty) = -\frac{1}{\beta d} \ln \left(1 - \sqrt{1 - \frac{W_0}{U_0}}\right) \simeq 1.873$. For type B, F_s remains constant over a wide range of $\mathcal{S}$. Simulation parameters are as in Table 2.1.

6.2.4 *Results for multiple filaments*

So far in this section, we have discussed the difference between type A and B dynamics for the case of a single filament in the system. Here, we present our results for multiple filaments. Interestingly, in some cases we find opposite behavior compared to the single filament case. In Fig. 6.5 we show force-velocity curves for different $\mathcal{S}$ values for type A and B dynamics. While for type A model, force-velocity variation depends on $\mathcal{S}$, the shape of the curve remains concave-like for a wide range of $\mathcal{S}$ that we have examined. On the other hand, the data for type B model [in Fig. 6.5(b)] show that $F - V$ characteristic changes from convex to concave as $\mathcal{S}$ value increases. This behavior is opposite to what we had observed for the single filament case (see the data in Fig. 6.3), where type A model showed convex to

concave transition as $\mathcal{S}$ is varied and type B model showed no dependence of $F-V$ shape on $\mathcal{S}$. We explain this result below.

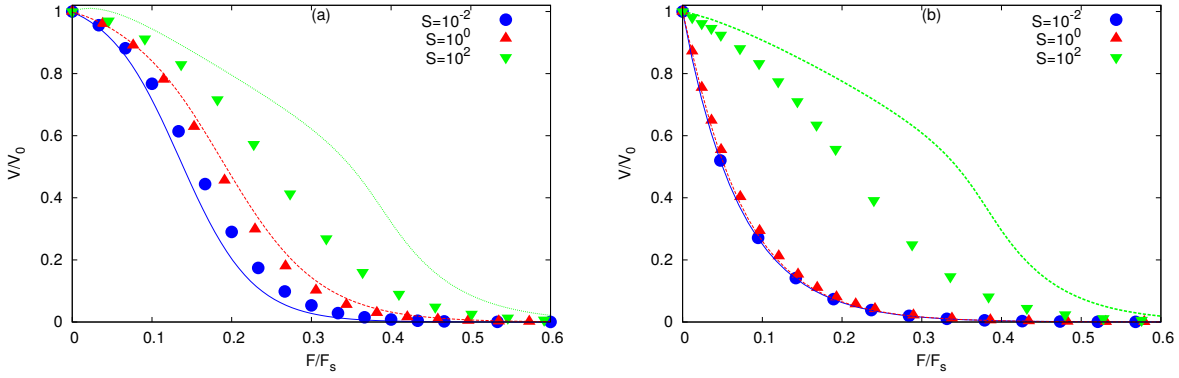

Figure 6.5: Force velocity curves for multiple filaments with rigid barrier. **(a)** Type A: The force velocity curve is concave for any value of $\mathcal{S}$. **(b)** type B: Force velocity curve is convex for small $\mathcal{S}$ while it changes to concave for large $\mathcal{S}$. Our analytical predictions are shown by continuous lines and they match well for small $\mathcal{S}$. We use $N = 20$ here. Other simulation parameters are as in Table 2.1.

In order to explain the above results analytically, we need to first calculate the contact probability p_0 as done for the single filament case. For multiple filament case with type A interaction, when a bound filament polymerizes, it will change p_i and thus have its corresponding loss or gain terms in the time evolution equation for p_i. For type B, on the other hand, a bound filament can not polymerize. Thus, unlike single filament case, in this case, type A and B will have different time evolution equations for p_i. The value of p_0 also turns out to be different for type A and B in this case. The time-evolution equations for p_i for type A interaction can be written as,

$$\frac{dp_0}{dt} = \{U_0 + \mathcal{S}(1-p_0)^{N-1}\}p_1 - \{(N-1)U_0 p_0 e^{-\beta F d} + W_0 + \mathcal{S}e^{-\beta F d}\}p_0, \tag{6.6}$$

$$\begin{aligned}\frac{dp_i}{dt} &= \{(N-1)U_0 p_0 e^{-\beta F d} + W_0 + \mathcal{S}e^{-\beta F d}\}p_{i-1} + \{U_0 + \mathcal{S}(1-p_0)^{N-1}\}p_{i+1} \\ &- \{(N-1)U_0 p_0 e^{-\beta F d} + W_0 + \mathcal{S}e^{-\beta F d} + U_0 + \mathcal{S}(1-p_0)^{N-1}\}p_i; \quad \text{for } i \geq 1.\end{aligned} \tag{6.7}$$

Solving the Eqs. 6.6 and 6.7 in steady state, we obtain the recursion relation

$$p_i = \left(\frac{(N-1)U_0 p_0 e^{-\beta F d} + W_0 + \mathcal{S}e^{-\beta F d}}{U_0 + \mathcal{S}(1-p_0)^{N-1}}\right)^i p_0;\ i = 1, 2, \ldots \tag{6.8}$$

Using the normalization relation, $\sum p_i = 1$ we get

$$\frac{\{(N-1)U_0 p_0 + \mathcal{S}\}e^{-\beta F d} + W_0}{U_0 + \mathcal{S}(1-p_0)^{N-1}} + (p_0 - 1) = 0 \tag{6.9}$$

where p_0 is the contact probability. We can solve the above equation numerically and obtain p_0 as a function of $\mathcal{S}$ and F. We compare this result with simulation in Fig. 6.6(a) and find reasonable agreement.

For type B interaction, the time evolution equation will have the form,

$$\frac{dp_0}{dt} = \{U_0 + \mathcal{S}(1-p_0)^{N-1}\}p_1 - \{W_0 + \mathcal{S}e^{-\beta F d}\}p_0, \tag{6.10}$$

$$\frac{dp_i}{dt} = \{\mathcal{S}e^{-\beta F d} + W_0\}p_{i-1} + \{U_0 + \mathcal{S}(1-p_0)^{N-1}\}p_{i+1} - \{\mathcal{S}e^{-\beta F d} + W_0 + U_0 + \mathcal{S}(1-p_0)^{N-1}\}p_i; \quad \text{for } i \geq 1. \tag{6.11}$$

In the same way, we obtain the recursion relation

$$p_i = \left(\frac{\mathcal{S}e^{-\beta F d} + W_0}{U_0 + \mathcal{S}(1-p_0)^{N-1}}\right)^i p_0; \; i = 1, 2, \ldots \tag{6.12}$$

Using the normalization relation, $\sum p_i = 1$ we get

$$\frac{\mathcal{S}e^{-\beta F d} + W_0}{U_0 + \mathcal{S}(1-p_0)^{N-1}} + (p_0 - 1) = 0 \tag{6.13}$$

where p_0 is the contact probability. Solving the equation numerically we can obtain p_0 for any general value of $\mathcal{S}$ and F [see Fig. 6.6(b)].

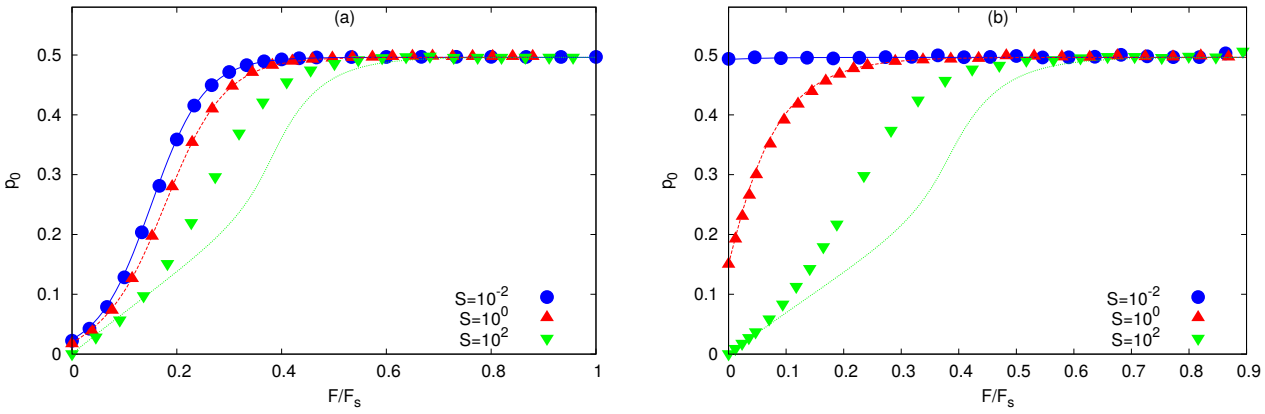

Figure 6.6: Contact probability (p_0) as a function of F for rigid barrier with multiple filaments. **(a)** Type A: For small F, p_0 remains close to zero while for large F, it increases with F and saturates to $1/2$. **(b)** Type B: Unlike type A, at $F = 0$, the value of p_0 increases as $\mathcal{S}$ decreases. For high value of $\mathcal{S}$, p_0 starts from small value and then increase with F which finally saturates to $1/2$. Points are simulation results and lines are analytical predictions. We use $N = 20$ here. Other simulation parameters are as in Table 2.1.

For type A dynamics, the expression for the barrier velocity can be written as

$$V(F) = d[Np_0U_0e^{-\beta F d} + \mathcal{S}\{e^{-\beta F d} - (1-p_0)^N\}] \tag{6.14}$$

The terms in Eq. 6.14 have similar explanations as given in Sec. 6.2.2. The last term corresponds to the situation when no filament is bound to the barrier, which is required for downward movement of the barrier. After substituting for p_0, we compare the resulting expression for $V(F)$ against simulations in Fig. 6.5(a). We find that for $\mathcal{S} \lesssim 1$ the agreement is reasonably good but for $\mathcal{S} \gg 1$, there is deviation between the two results. In our analytical calculation, we have used the assumption that the filaments are independent. This is not strictly true, since the barrier induces an effective coupling between the filaments and for large $\mathcal{S}$ the effect of this coupling can not be neglected any more. This is the reason of the mismatch between analytical and simulation results for large $\mathcal{S}$.

Note that in Eq. 6.14 the first term dominates in the limit of small $\mathcal{S}$ and unlike in the single filament case, when $p_0 \simeq (1 - W_0/U_0) \simeq 1/2$ in that limit, the contact probability for the multiple filament case increases with F (see Eq. 6.9). Thus even for small $\mathcal{S}$ when barrier dynamics can be almost ignored, the force-velocity curve is not a simple exponential (or convex). In fact few simple algebraic steps from Eqs. 6.14 and 6.9 show that $V(F)$ stays almost constant for small F and decreases rapidly as F increases. In other words, the force-velocity curve is concave. In other words, the difference in the behavior of the contact probability is responsible for the difference with the single filament case.

For type B, since there is no bound filament polymerization, and only the last two terms in Eq. 6.14 survive. We compare the analytical results with numerics which show good agreement for small $\mathcal{S}$. The contact probability p_0 in this case shows a weaker dependence on F and for a wide range of F, it remains close to $1/2$ (see Fig. 6.6). Then the last term is a constant and $V(F)$ becomes almost exponential and hence convex. As $\mathcal{S}$ increases, p_0 shows stronger F-dependence, and the F-dependence of the last term cannot be ignored any more. The curve thus deviates from exponential and actually becomes concave.

The stall force F_s for multiple filament case also show different behavior for type A and B. For type A model, F_s decreases with $\mathcal{S}$ while for type B, it remains constant (see Fig. 6.7). Similar behavior was observed for the single filament case. From the expression of $V(F)$, we can calculate F_s analytically. For large F, where stalling happens, p_0 is close to $(1 - W_0/U_0) \simeq 1/2$ for all values of $\mathcal{S}$ (see Eq. 6.9). Equating $V(F_s)$ to zero gives, for type A case

$$F_s = \frac{1}{\beta d}\left\{N \ln\left(\frac{U_0}{W_0}\right) + \ln\left(1 + \frac{N(U_0 - W_0)}{\mathcal{S}}\right)\right\} \tag{6.15}$$

which explicitly depends upon $\mathcal{S}$.

For type B, the expression for F_s turns out to be,

$$F_s = \frac{N}{\beta d} \ln\left(\frac{U_0}{W_0}\right) \tag{6.16}$$

which is independent of $\mathcal{S}$. We plot F_s as a function of $\mathcal{S}$ for both the cases and compare our analytical results with numerics. Our analytical expression show good agreement. We also note that the saturation value of F_s for type A is close to that for type B as $\mathcal{S} >> 1$. Thus, similar to the single filament case, in this case also, for $\mathcal{S} >> 1$, both the models show the same behaviour.

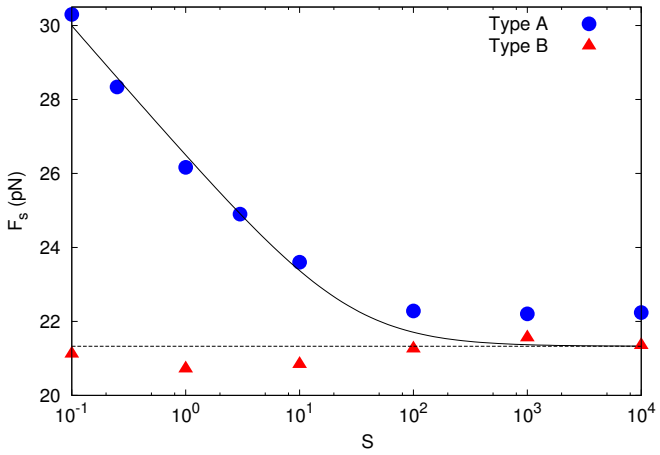

Figure 6.7: F_s as a function of $\mathcal{S}$ for multiple filaments with rigid barrier. We note that for type A, F_s decreases with $\mathcal{S}$ while for type B, F_s remains constant with $\mathcal{S}$. Lines are analytical predications that matches well with the numerical data. We use $N = 20$ here. Other simulation parameters are as in Table 2.1.

From Eqs. 6.15 and 6.16 we also see that the scaling of stall force on the number of filaments is different for type A and B models. While for type B, stall force scales linearly with N, for type A there is an additional logarithmic correction. Note that for a rigid barrier, there is no shape fluctuation and the entire barrier moves as a whole. This means for type A model, whenever a bound filament polymerizes, pushing the barrier up, all other bound filaments immediately becomes free. Thus an effective interaction is induced among the filaments. For type B model however, there is no bound filament polymerization and this effect is not there. In this case the stall force increases proportionately as N is increased. An absence of linear scaling between F_s and N has also been reported in earlier studies [19, 29] and was explained by using effects like ATP hydrolysis of actin monomers. Here, we have shown similar effects but from a different origin. We plot F_s/N as a function of N for different values of $\mathcal{S}$ and compare with our analytical expressions in Fig. 6.8. The main plot is for type A while the inset is for type B. We note that for type A, the curve for larger $\mathcal{S}$ is always below the curve for smaller $\mathcal{S}$, which is consistent with our earlier observation (Fig. 6.7) that stall force decreases with $\mathcal{S}$. For type B, on the other hand, all the curves fall on top of each other, because in this case, F_s is independent of $\mathcal{S}$. We also note that, in the limit $\mathcal{S} >> 1$, curves for type A and B become similar.

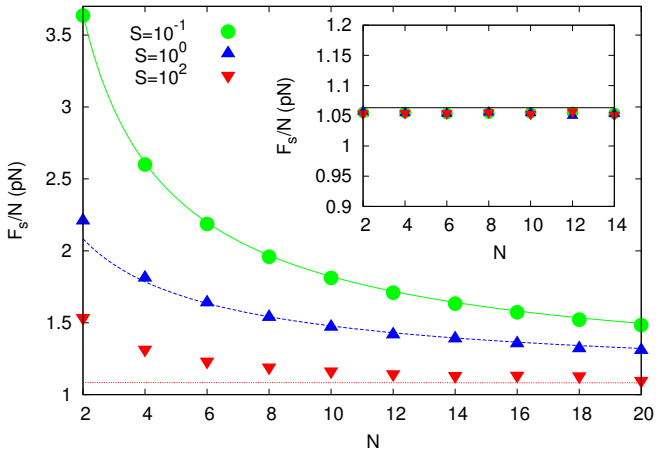

Figure 6.8: F_s/N as a function of N for rigid barrier. Main plot is for type A and the inset is for type B. For type A, The variation of F_s with N deviates from linearity and also depends on $\mathcal{S}$. For $\mathcal{S} >> 1$, the deviation is smaller. For type B, F_s/N remains constant with N and the variation is independent of $\mathcal{S}$. Our analytical predictions matches well with the numerics. Simulation parameters are as in Table 2.1.

6.3 KPZ BARRIER MODEL

In Chapter 2, we had studied KPZ-barrier with type A interaction. In this section, we will study the comparison between type A and B interactions for the same model. In the earlier case (Chapter 2), we allow the filaments to push the barrier locally (pushing against a valley) as well as globally, while the independent fluctuations are restricted to be local movements (hill-valley flipping) only. For type B interaction, the bound filament polymerization is absent and since the independent fluctuations are only local, it will give rise to large differences in the description of these two models. Thus, in order to ensure the other differences remains minimal, in the present case, we ignore any global movement of the barrier for type A interaction. Thus, for type A interaction, the dynamics shown in Fig. 2.1(a), 2.1(c) and 2.1(d) are allowed while for type B interaction, only the dynamics 2.1(c) and 2.1(d) are allowed. The simulation technique is same as described in Chapter 2. We only discuss the results for single filament here. For multiple filaments also, we note the same qualitative behaviour (data not shown).

We find that the barrier velocity is systematically higher for type A compared to type B model, as expected. However, in this case the main qualitative difference between the two models is observed only in the dependence of stall force F_s on $\mathcal{S}$. In Fig. 6.9 we show that for type A stall force decreases with $\mathcal{S}$ and for type B it stays constant. This is consistent with the data shown in Fig. 6.4 for rigid barrier. For KPZ barrier, many other quantities like V_0, force-velocity curve, while quantitatively different for type A and B models, show similar qualitative behavior. The reason can be explained in the following way. Although bound

filament polymerization is allowed for type A model, this process happens only when there is a valley present at the binding site. The probability for such an occurrence is low. Most of the time the binding site sits on a local hill and when in contact with a filament, that hill cannot even flip to a valley. Thus even though type A model allows bound filament polymerization, most of the time this polymerization does not take place and the mechanism then becomes effectively similar to type B.

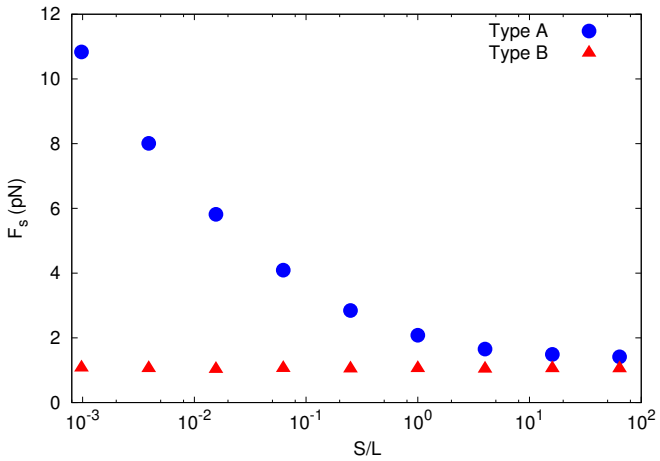

Figure 6.9: F_s as a function of $\mathcal{S}/L$. We note that for type A, the stall force decreases with $\mathcal{S}/L$. For type B, the stall force remains constant with $\mathcal{S}/L$ over a wide range of $\mathcal{S}/L$. For very large $\mathcal{S}/L$, F_s for both the cases saturates to the same value. Here we use $L = 64$, $N = 1$. Other simulation parameters are as in Table 2.1.

6.4 ELASTIC BARRIER MODEL

In this section, we discuss the difference between type A and B dynamics for an elastic barrier model which is studied in chapter 3 (Gradient Model). The dynamics and the simulation techniques are same as described in chapter 3. For type A interactions, all the movements shown in Fig. 3.1 are allowed while for type B interaction, the dynamics shown in Fig. 3.1(c) is not allowed. We only present the results for single filament here and note that for multiple filaments also, the qualitative nature of the results remain same.

6.4.1 *Variation of V_0 with $\mathcal{S}/L$*

For $\mu = 0$, there is no energy cost for creating local protrusions or height gradient on the membrane. Apart from the binding sites, all $(L-1)$ membrane sites undergo equilibrium thermal fluctuations in this case and the time-averaged local velocity of the membrane is zero at all these sites. Only the binding site feels the presence of the growing filament: for type A interaction, the filament pushes at the binding site and gives it a non-zero velocity

while for type B interaction, the filament blocks downward movement of the binding site and thus imparts a velocity to the membrane. Following similar steps as done in the rigid barrier case, it is easy to show that for type A model, $V_0 = d(U_0 - W_0)/L$, which does not depend on $\mathcal{S}$, and for type B model $V_0 = \frac{d}{L}\frac{(U_0 - W_0)}{1+\frac{U_0}{(\mathcal{S}/L)}}$, which has an explicit dependence on $\mathcal{S}$. This behaviour is same as the rigid barrier case with $\mathcal{S}$ replaced by $\mathcal{S}/L$ in this case. In Fig. 6.10 we show the comparison with simulation data.

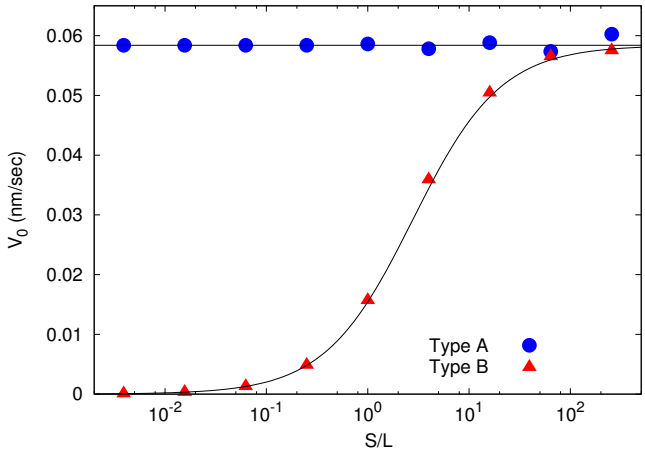

Figure 6.10: Velocity at $\mu = 0$ as a function of $\mathcal{S}/L$ for elastic barrier. For type A, we note that the velocity for $\mu = 0$ remains constant with $\mathcal{S}/L$. The value is $V_0 = d(U_0 - W_0)/L$. For type B, unlike type A, velocity increases with $\mathcal{S}/L$ and saturates to a value $d(U_0 - W_0)/L$, same as the velocity for type A. We use $L = 64$ for both the cases. Other simulation parameters are as in Table 2.1.

6.4.2 $\mu - V$ curves for different values of $\mathcal{S}/L$

In Fig. 6.11 we plot $\mu - V$ curve for different values of $\mathcal{S}/L$. The $\mu - V$ data for type A interaction were also presented in Chapter 3. For both type A and B dynamics, the curve shows a peak for $\mathcal{S}/L = 1$ and becomes monotonic concave curve for $\mathcal{S}/L \gg 1$. However, as $\mathcal{S}/L$ becomes smaller than unity, the curve becomes convex for type A and for type B the curve continues to show a peak and the peak position does not depend on $\mathcal{S}/L$ in this regime. So the main qualitative difference in this case is obtained for small values of $\mathcal{S}/L$ when the membrane dynamics is much slower than the filament dynamics. Since for very large $\mathcal{S}$, the difference between type A and B ceases to exist, we find concave $\mu - V$ curves for both models in this limit.

In order to explain this difference, we measure the relative contribution of V_{bind} and V_{bulk} towards the average membrane velocity. In Fig. 6.12 we plot $\frac{V_{bind}}{(L-1)V_{bulk}}$ at a fixed $\mu < \mu^*$ as a function of $\mathcal{S}/L$. When this ratio is close to 1, that means both binding site and bulk sites have comparable contribution, but if the ratio is much larger than 1, bulk site contribution

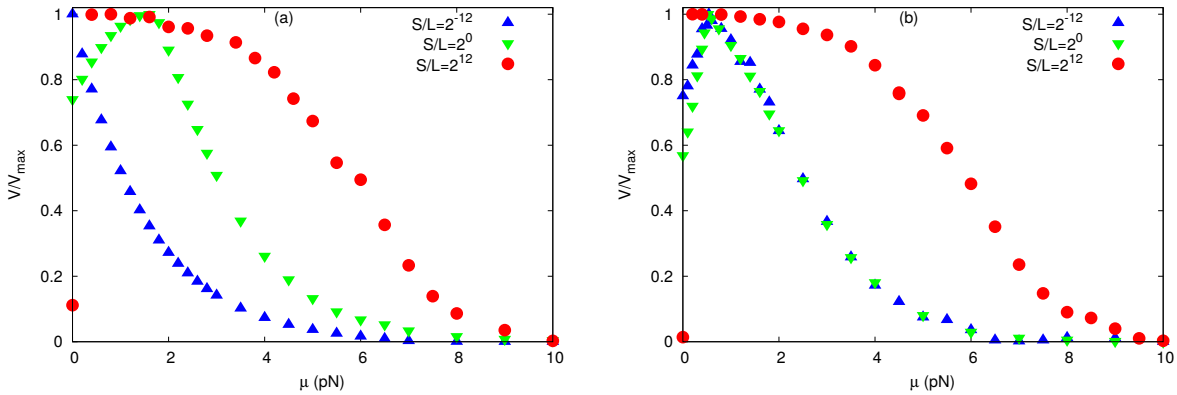

Figure 6.11: $\mu - V$ curve for different values of $\mathcal{S}/L$ for elastic barrier. We have scaled V by maximum velocity V_{max} to compare them in the same scale. **(a)** Type A: For $\mathcal{S}/L \sim 1$, the $\mu - V$ curve is non-monotonic with a peak at $\mu = \mu^*$. As $\mathcal{S}/L$ increases, the peak shifts towards to smaller value of μ and finally the curve becomes concave for $\mathcal{S}/L >> 1$. For $\mathcal{S}/L << 1$, the curve is convex. **(b)** Type B: In this case, unlike the previous case, we do not have any convex curve even for $\mathcal{S}/L << 1$. For all the above plots, we have used $L = 64$. Note that for $\mathcal{S}/L >> 1$, both the cases show a concave $\mu - V$ curve. Other simulation parameters are as in Table 2.1.

can be ignored. Our data show that for type A model, the ratio increases as $\mathcal{S}/L$ decreases, meaning for small $\mathcal{S}/L$ binding site velocity dominates. Since, V_{bind} falls monotonically with μ (Chapter 3), the average velocity also falls monotonically. For type B, on the other hand, the ratio remains close to 1 even when $\mathcal{S}/L << 1$ and due to non-monotonic variation of V_{bulk} with μ the $\mu - V$ curve remains peaked in this case.

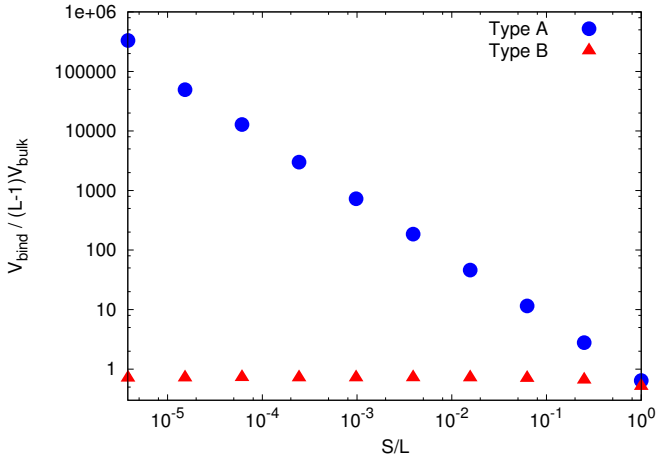

Figure 6.12: Variation of $\frac{V_{bind}}{(L-1)V_{bulk}}$ with $\mathcal{S}/L$ for elastic barrier. For type A, we note that as $\mathcal{S}/L$ decreases, the value of $\frac{V_{bind}}{(L-1)V_{bulk}}$ increases which means that the contribution of binding site to the total velocity increases in comparison to the bulk sites. Thus, the nature of $\mu - V$ curve changes to convex for $\mathcal{S}/L << 1$. Here we use $\mu = 0.87pN$ which is less than μ^*. For type B, as $\mathcal{S}/L$ decreases, the value of $\frac{V_{bind}}{(L-1)V_{bulk}}$ does not vary much. Thus, even for $\mathcal{S}/L << 1$, the terms V_{bind} and V_{bulk} remain comparable and the $\mu - V$ curve remains non-monotonic. Here we use $\mu = 0.26pN$. For both the models, we use $L = 64$. Other simulation parameters are as in Table 2.1.

6.4.3 *Variation of μ^* with $\mathcal{S}/L$*

In chapter 3, we have seen that μ^* decreases with $\mathcal{S}/L$ for type A interaction, but for type B, the variation of μ^* as a function of $\mathcal{S}/L$ is different. We note that for type B, the peak position in the elasticity-velocity curve remains fixed over a wide range of $\mathcal{S}/L \lesssim 1$ (see Fig. 6.13). In Sec. 3.3.3, we have calculated analytically the variation of μ^* with $\mathcal{S}/L$ for type A (see Eq. 3.6). The same behavior can also be explained by the force balance at the tip of filament. Note that for the rigid barrier case discussed in Sec. 6.2.3, the balance between polymerization force and externally applied force is reached at the point of stalling and we can therefore use the expression for F_s calculated in Sec. 6.2.3 for the polymerization force generated by the filaments, even in the case of an elastic barrier. The only modification in this case is for type A model, where there is an explicit $\mathcal{S}$ dependence of F_s (see Eq. 6.5), one must replace $\mathcal{S}$ by $\mathcal{S}/L$ because unlike a rigid barrier, the whole elastic barrier does not move as a single unit and height fluctuations take place at each of L sites on the barrier. This gives for type A

$$\mu^* = -\frac{1}{2\beta d} ln\left[\left(\frac{U_0 - W_0 + 2\frac{\mathcal{S}}{L}}{2\frac{\mathcal{S}}{L}}\right)\left(1 - \sqrt{1 - \frac{4U_0W_0(\frac{\mathcal{S}}{L})^2}{U_0^2(U_0 - W_0 + 2\frac{\mathcal{S}}{L})^2}}\right)\right] \tag{6.17}$$

and for type B

$$\mu^* = \frac{1}{2\beta d} ln\left(\frac{U_0}{W_0}\right). \tag{6.18}$$

Our data in Fig. 6.13 shows good agreement with this calculation. This plot shows that for type A, as $\mathcal{S}/L$ is increased, μ^* decreases and for type B it remains constant. The data for type A appeared earlier in Chapter 3. Note that although the $\mu - V$ curve becomes monotonic for type A model in the limit of small $\mathcal{S}/L$, one still has a finite μ^*.

In this section, we have studied the comparison between type A and B interactions using the gradient model for the barrier, which is studied in Chapter 3. In Chapter 4, where we have studied the Gaussian model, the elastic energy of the barrier is proportional to square of the local height gradient [26, 70]. In this case, we find only quantitative difference between type A and B dynamics (data not shown here), and qualitative behavior remains mostly similar.

6.5 CONCLUSION

In summary, we have studied the force generation by a set of parallel actin filaments growing against a barrier by considering two models for the filament-barrier interaction. In type A

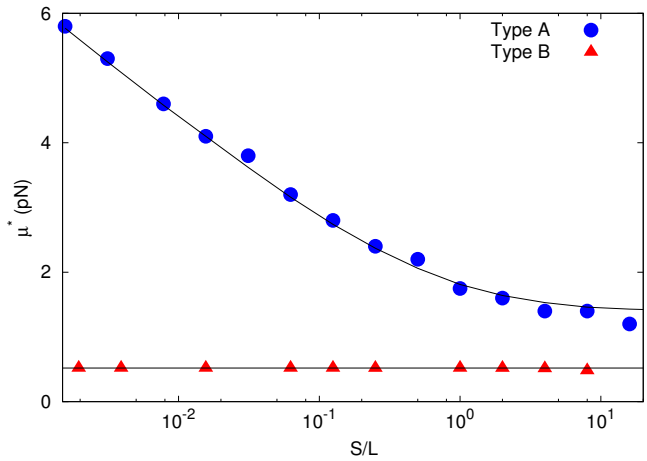

Figure 6.13: Variation of μ^* with $\mathcal{S}/L$ for elastic barrier. For type A, μ^* decreases continuously with $\mathcal{S}/L$. For type B, μ^* remains constant for a wide range of $\mathcal{S}/L$. Our analytical predictions matches well with the numerical results. Simulation parameters are as in Table 2.1.

model, the filaments can push the barrier and grow, while in type B model, the filaments can grow only when thermal fluctuations of the barrier position creates a space for growth. It is clear from the definition of the two models that in identical conditions, the velocity of the barrier in type A model cannot fall below that in type B model. We also find important qualitative differences between the two model types. We demonstrate these differences for three barrier dynamics: Rigid barrier, KPZ barrier and elastic barrier. In all three cases, we find that the main differences between type A and B models are manifested in the way various properties depend on the relative time-scale $\mathcal{S}$ between the filament and barrier dynamics. In the limit of very large $\mathcal{S}$, when the thermal fluctuations of barrier position are much faster than filament (de)polymerization, we find type A and B models become similar. In this case, since the contact probability p_0 becomes negligible, the filaments grow freely most of the time without pushing the barrier even for type A interaction. Thus, in this limit, the two models yield same results. However, for small and moderate $\mathcal{S}$ values, we find significant differences.

The competition between polymerization force of the filaments and the opposing force exerted by the barrier shapes the underlying physics of the system. For a rigid barrier and a KPZ barrier, this opposing force is described as an external force that tends to move the barrier downward, while polymerization force coming from the filaments is pushing the barrier upward. The point of balance between these two forces is achieved at stalling, when the barrier velocity vanishes. For an elastic membrane, the competition between the two forces plays out in a different way. In this case, the elastic force of the barrier tries to maintain a flat shape of the membrane, while filament polymerization tends to create protrusions on the membrane. The point of balance in this case is μ^*, when the binding site and bulk site velocities become equal. We show that for all three barriers, the point of balance depends

on $\mathcal{S}$ for type A model: The stall force F_s (for rigid and KPZ barrier) and μ^* (for elastic barrier) decreases with $\mathcal{S}$ and saturates to a constant value for large $\mathcal{S}$. For type B models, we find that F_s and μ^* remains independent of $\mathcal{S}$. In other words, when the bound filament polymerization is not allowed, the polymerization force is insensitive to the time-scale of thermal fluctuations, but when the bound filaments can actively push the barrier and grow, the polymerization force decreases as the barrier dynamics becomes faster. On the contrary, when there is no opposing force offered by the barrier, i.e. $F = 0$ or $\mu = 0$, the two models show opposite behavior. For type A models, in this limit there is no difference between free and bound filament polymerization rate, and the barrier velocity V_0 in this case does not depend on $\mathcal{S}$ for rigid and elastic barrier. However, for type B models, since bound filaments cannot polymerize, polymerization process still has to wait when thermal fluctuations create a space for growth and hence V_0 for type B models increases with $\mathcal{S}$.

Our study shows that while modelling force generation of actin filaments, it is important to consider what type of filament barrier interaction should be included in the model. The seemingly minor details like whether bound filament polymerization is allowed or not, may give rise to qualitatively different outcomes. Based on the results we have presented here, it is also possible to perform experimental measurements to decide which type of model would be suitable in a given situation. The relative time-scale between the barrier and filament dynamics may be varied by controlling the free filament polymerization rate which depends on the concentration of monomers in the medium. By directly measuring the variation of quantities like stall force, or force-velocity curve as a function of this time-scale, it should be possible to decide the suitability of a particular model type.

BIBLIOGRAPHY

[1]J. Howard, *Mechanics of motor proteins and the cytoskeleton* (Sunderland, MA: Sinauer Associates, 2001) (cit. on pp. 1, 17).

[2]T. D. Pollard and J. A. Cooper, "Actin, a central player in cell shape and movement," Science **326**, 1208–1212 (2009), eprint: http://science.sciencemag.org/content/326/5957/1208.full.pdf (cit. on p. 1).

[3]L. Blanchoin, R. Boujemaa-Paterski, C. Sykes, and J. Plastino, "Actin dynamics, architecture, and mechanics in cell motility," Physiological Reviews **94**, PMID: 24382887, 235–263 (2014), eprint: https://doi.org/10.1152/physrev.00018.2013 (cit. on p. 1).

[4]P. Friedl and D. Gilmour, "Collective cell migration in morphogenesis, regeneration and cancer," Nature Reviews Molecular Cell Biology **10**, Review Article, 445 EP – (2009) (cit. on p. 1).

[5]J. Plastino and C. Sykes, "The actin slingshot," Current Opinion in Cell Biology **17**, 62 –66 (2005) (cit. on p. 1).

[6]M. P. Taylor, O. O. Koyuncu, and L. W. Enquist, "Subversion of the actin cytoskeleton during viral infection," Nature Reviews Microbiology **9**, Review Article, 427 EP – (2011) (cit. on p. 3).

[7]Y. Marcy, J. Prost, M.-F. Carlier, and C. Sykes, "Forces generated during actin-based propulsion: a direct measurement by micromanipulation," Proceedings of the National Academy of Sciences **101**, 5992–5997 (2004), eprint: http://www.pnas.org/content/101/16/5992.full.pdf (cit. on pp. 3, 7, 29, 32).

[8]C. Brangbour, O. du Roure, E. Helfer, D. Démoulin, A. Mazurier, M. Fermigier, M.-F. Carlier, J. Bibette, and J. Baudry, "Force-velocity measurements of a few growing actin filaments," PLOS Biology **9**, 1–7 (2011) (cit. on pp. 3, 29, 32).

[9]D. Démoulin, M.-F. Carlier, J. Bibette, and J. Baudry, "Power transduction of actin filaments ratcheting in vitro against a load," Proceedings of the National Academy of Sciences **111**, 17845–17850 (2014), eprint: http://www.pnas.org/content/111/50/17845.full.pdf (cit. on pp. 3, 4, 29, 32).

[10]S. H. Parekh, O. Chaudhuri, J. A. Theriot, and D. A. Fletcher, "Loading history determines the velocity of actin-network growth," Nature Cell Biology **7**, 1219 EP – (2005) (cit. on pp. 3, 4, 29, 32).

[11]M. Prass, K. Jacobson, A. Mogilner, and M. Radmacher, "Direct measurement of the lamellipodial protrusive force in a migrating cell," The Journal of Cell Biology **174**, 767–772 (2006), eprint: http://jcb.rupress.org/content/174/6/767.full.pdf (cit. on pp. 3, 4, 7).

[12]F. Heinemann, H. Doschke, and M. Radmacher, "Keratocyte lamellipodial protrusion is characterized by a concave force-velocity relation," Biophysical Journal **100**, 1420 –1427 (2011) (cit. on pp. 3, 4, 7).

[13]C. Peskin, G. Odell, and G. Oster, "Cellular motions and thermal fluctuations: the brownian ratchet," Biophysical Journal **65**, 316 –324 (1993) (cit. on pp. 3–5, 7, 9, 28, 29, 32, 36, 66, 68).

[14]A. E. Carlsson, "Force-velocity relation for growing biopolymers," Phys. Rev. E **62**, 7082–7091 (2000) (cit. on pp. 3–5, 28, 29).

[15]N. J. Burroughs and D Marenduzzo, "Growth of a semi-flexible polymer close to a fluctuating obstacle: application to cytoskeletal actin fibres and testing of ratchet models," Journal of Physics: Condensed Matter **18**, S357 (2006) (cit. on pp. 3–5).

[16]T. E. Schaus and G. G. Borisy, "Performance of a population of independent filaments in lamellipodial protrusion," Biophysical Journal **95**, 1393 –1411 (2008) (cit. on pp. 3–5).

[17]K. Tsekouras, D. Lacoste, K. Mallick, and J.-F. Joanny, "Condensation of actin filaments pushing against a barrier," New Journal of Physics **13**, 103032 (2011) (cit. on pp. 3–5, 7, 9, 13, 21, 23, 29, 36, 66, 68).

[18]J. Krawczyk and J. Kierfeld, "Stall force of polymerizing microtubules and filament bundles," EPL (Europhysics Letters) **93**, 28006 (2011) (cit. on pp. 3–7, 36, 66).

[19]D. Das, D. Das, and R. Padinhateeri, "Collective force generated by multiple biofilaments can exceed the sum of forces due to individual ones," New Journal of Physics **16**, 063032 (2014) (cit. on pp. 3–5, 7, 9, 29, 36, 66, 68, 76).

[20]D. R. Kovar and T. D. Pollard, "Insertional assembly of actin filament barbed ends in association with formins produces piconewton forces," Proceedings of the National Academy of Sciences **101**, 14725–14730 (2004), eprint: http://www.pnas.org/content/101/41/14725.full.pdf (cit. on pp. 3, 6).

[21]M. J. Footer, J. W. J. Kerssemakers, J. A. Theriot, and M. Dogterom, "Direct measurement of force generation by actin filament polymerization using an optical trap," Proceedings of the National Academy of Sciences **104**, 2181–2186 (2007), eprint: http://www.pnas.org/content/104/7/2181.full.pdf (cit. on pp. 3, 6).

[22]J. Zimmermann, C. Brunner, M. Enculescu, M. Goegler, A. Ehrlicher, J. Käs, and M. Falcke, "Actin filament elasticity and retrograde flow shape the force-velocity relation of motile cells," Biophysical Journal **102**, 287 –295 (2012) (cit. on p. 4).

[23]D. K. Hansda, S. Sen, and R. Padinhateeri, "Branching influences force-velocity curves and length fluctuations in actin networks," Phys. Rev. E **90**, 062718 (2014) (cit. on pp. 4, 6, 9, 17, 29, 32, 36, 66, 68).

[24]E. Atilgan, D. Wirtz, and S. X. Sun, "Mechanics and dynamics of actin-driven thin membrane protrusions," Biophysical Journal **90**, 65 –76 (2006) (cit. on pp. 4, 9, 30, 52, 53).

[25]S. L. Narasimhan and A. Baumgaertner, "Dynamics of a driven surface," The Journal of Chemical Physics **133**, 034702 (2010), eprint: https://doi.org/10.1063/1.3447384 (cit. on pp. 4, 9, 31, 44, 46, 66).

[26]A. Baumgaertner, "Crawling of a driven adherent membrane," The Journal of Chemical Physics **137**, 144906 (2012), eprint: https://doi.org/10.1063/1.4757664 (cit. on pp. 4, 9, 31, 46, 81).

[27]L. Hu and G. A. Papoian, "Molecular transport modulates the adaptive response of branched actin networks to an external force," The Journal of Physical Chemistry B **117**, PMID: 23962335, 13388–13396 (2013), eprint: https://doi.org/10.1021/jp405179e (cit. on pp. 4, 9, 53, 55).

[28]J. Weichsel and P. L. Geissler, "The more the tubular: dynamic bundling of actin filaments for membrane tube formation," PLOS Computational Biology **12**, 1–13 (2016) (cit. on pp. 4, 9, 53).

[29]A. E. Carlsson, "Model of reduction of actin polymerization forces by atp hydrolysis," Physical Biology **5**, 036002 (2008) (cit. on pp. 4, 7, 76).

[30]J. Zhu and A. Mogilner, "Mesoscopic model of actin-based propulsion," PLOS Computational Biology **8**, 1–12 (2012) (cit. on pp. 6, 29, 40).

[31]R. Wang and A. E. Carlsson, "Load sharing in the growth of bundled biopolymers," New Journal of Physics **16**, 113047 (2014) (cit. on pp. 6, 9, 29, 32, 36, 40, 66, 68, 70).

[32]P. A. Giardini, D. A. Fletcher, and J. A. Theriot, "Compression forces generated by actin comet tails on lipid vesicles," Proceedings of the National Academy of Sciences **100**, 6493–6498 (2003), eprint: http://www.pnas.org/content/100/11/6493.full.pdf (cit. on p. 7).

[33]G. S. van Doorn, C. Tănase, B. M. Mulder, and M. Dogterom, "On the stall force for growing microtubules," European Biophysics Journal **29**, 2–6 (2000) (cit. on p. 7).

[34]P. Sens and J. Plastino, "Membrane tension and cytoskeleton organization in cell motility," Journal of Physics: Condensed Matter **27**, 273103 (2015) (cit. on pp. 8, 30).

[35]A. Diz-Muñoz, D. A. Fletcher, and O. D. Weiner, "Use the force: membrane tension as an organizer of cell shape and motility," Trends in Cell Biology **23**, 47 –53 (2013) (cit. on pp. 8, 30).

[36]J. Lemière, F. Valentino, C. Campillo, and C. Sykes, "How cellular membrane properties are affected by the actin cytoskeleton," Biochimie **130**, Lipidomics and Functional Lipid Biology, 33 –40 (2016) (cit. on pp. 8, 30).

[37]K. Keren, "Cell motility: the integrating role of the plasma membrane," European Biophysics Journal **40**, 1013 (2011) (cit. on pp. 8, 30).

[38]N. C. Gauthier, M. A. Fardin, P. Roca-Cusachs, and M. P. Sheetz, "Temporary increase in plasma membrane tension coordinates the activation of exocytosis and contraction during cell spreading," Proceedings of the National Academy of Sciences **108**, 14467–14472 (2011), eprint: http://www.pnas.org/content/108/35/14467.full.pdf (cit. on p. 8).

[39]D. Raucher and M. P. Sheetz, "Cell spreading and lamellipodial extension rate is regulated by membrane tension," The Journal of Cell Biology **148**, 127–136 (2000), eprint: http://jcb.rupress.org/content/148/1/127.full.pdf (cit. on pp. 8, 30, 65).

[40]E. L. Batchelder, G. Hollopeter, C. Campillo, X. Mezanges, E. M. Jorgensen, P. Nassoy, P. Sens, and J. Plastino, "Membrane tension regulates motility by controlling lamellipodium organization," Proceedings of the National Academy of Sciences **108**, 11429–11434 (2011), eprint: http://www.pnas.org/content/108/28/11429.full.pdf (cit. on pp. 8, 65).

[41]A. P. Liu, D. L. Richmond, L. Maibaum, S. Pronk, P. L. Geissler, and D. A. Fletcher, "Membrane-induced bundling of actin filaments," Nature Physics **4**, 789 EP – (2008) (cit. on pp. 8, 65).

[42]R. Dimova, "Recent developments in the field of bending rigidity measurements on membranes," Advances in Colloid and Interface Science **208**, Special issue in honour of Wolfgang Helfrich, 225 –234 (2014) (cit. on pp. 8, 53, 65).

[43]J. R. Henriksen, T. L. Andresen, L. N. Feldborg, L. Duelund, and J. H. Ipsen, "Understanding detergent effects on lipid membranes: a model study of lysolipids," Biophys J **98**, 20483328[pmid], 2199–2205 (2010) (cit. on pp. 8, 53, 65).

[44]H. Bouvrais, L. Duelund, and J. H. Ipsen, "Buffers affect the bending rigidity of model lipid membranes," Langmuir **30**, PMID: 24377876, 13–16 (2014), eprint: https://doi.org/10.1021/la403565f (cit. on pp. 8, 53, 65).

[45]J. Henriksen, A. C. Rowat, and J. H. Ipsen, "Vesicle fluctuation analysis of the effects of sterols on membrane bending rigidity," European Biophysics Journal **33**, 732–741 (2004) (cit. on pp. 8, 53, 65).

[46]G. Niggemann, M. Kummrow, and W. Helfrich, "The bending rigidity of phosphatidylcholine bilayers: dependences on experimental method, sample cell sealing and temperature," J. Phys. II France **5**, 413–425 (1995) (cit. on pp. 8, 53, 65).

[47]W. Helfrich, "Elastic properties of lipid bilayers: theory and possible experiments.," Z. Naturforsch **C28**, 693 –703 (1973) (cit. on pp. 9, 53).

[48]A. Perilli, C. Pierleoni, G. Ciccotti, and J.-P. Ryckaert, "On the force-velocity relationship of a bundle of rigid bio-filaments," The Journal of Chemical Physics **148**, 095101 (2018), eprint: https://doi.org/10.1063/1.5001124 (cit. on pp. 9, 66, 68).

[49]J. Valiyakath and M. Gopalakrishnan, "Polymerisation force of a rigid filament bundle: diffusive interaction leads to sublinear force-number scaling," Scientific Reports **8**, 2526 (2018) (cit. on pp. 9, 66, 68).

[50]M. Kardar, G. Parisi, and Y.-C. Zhang, "Dynamic scaling of growing interfaces," Phys. Rev. Lett. **56**, 889–892 (1986) (cit. on p. 13).

[51]T. Sasamoto and H. Spohn, "The 1 + 1-dimensional kardar-parisi-zhang equation and its universality class," Journal of Statistical Mechanics: Theory and Experiment **2010**, P11013 (2010) (cit. on p. 13).

[52]T. Sasamoto, "The 1d kardar-parisi-zhang equation: height distribution and universality," Progress of Theoretical and Experimental Physics **2016**, 022A01 (2016), eprint: /oup/backfile/content_public/journal/ptep/2016/2/10.1093_ptep_ptw002/3/ptw002.pdf (cit. on p. 13).

[53]P. Nath, P. K. Mandal, and D. Jana, "Kardar-parisi-zhang universality class of a discrete erosion model," International Journal of Modern Physics C **26**, 1550049 (2015), eprint: https://doi.org/10.1142/S0129183115500497 (cit. on p. 13).

[54]P. Gonçalves and M. Jara, "The einstein relation for the kpz equation," Journal of Statistical Physics **158**, 1262–1270 (2015) (cit. on p. 13).

[55]J. Quastel and H. Spohn, "The one-dimensional kpz equation and its universality class," Journal of Statistical Physics **160**, 965–984 (2015) (cit. on p. 13).

[56]M. Gubinelli and N. Perkowski, "Kpz reloaded," Communications in Mathematical Physics **349**, 165–269 (2017) (cit. on p. 13).

[57]T. Song and H. Xia, "Long-range temporal correlations in the kardar-parisi-zhang growth: numerical simulations," Journal of Statistical Mechanics: Theory and Experiment **2016**, 113206 (2016) (cit. on p. 13).

[58]W. S. Alves, E. A. Rodrigues, H. A. Fernandes, B. A. Mello, F. A. Oliveira, and I. V. L. Costa, "Analysis of etching at a solid-solid interface," Phys. Rev. E **94**, 042119 (2016) (cit. on p. 13).

[59]P. Dolai, A. Basu, and A. Simha, "Universal spatiotemporal scaling of distortions in a drifting lattice," Phys. Rev. E **95**, 052115 (2017) (cit. on p. 13).

[60]H. Xia, G. Tang, and Y. Lan, "Numerical analysis of long-range spatial correlations in surface growth," Phys. Rev. E **94**, 062121 (2016) (cit. on p. 13).

[61]M. Hoshino, "Kpz equation with fractional derivatives of white noise," Stochastics and Partial Differential Equations: Analysis and Computations **4**, 827–890 (2016) (cit. on p. 13).

[62]R. K. Sadhu and S. Chatterjee, "Actin filaments growing against a barrier with fluctuating shape," Phys. Rev. E **93**, 062414 (2016) (cit. on pp. 14, 32, 35, 40).

[63]S. F. Edwards and D. R. Wilkinson, "The surface statistics of a granular aggregate," Proceedings of the Royal Society of London. Series A, Mathematical and Physical Sciences **381**, 17–31 (1982) (cit. on p. 16).

[64]T. D. Pollard, "Rate constants for the reactions of atp- and adp-actin with the ends of actin filaments.," The Journal of Cell Biology **103**, 2747–2754 (1986), eprint: `http://jcb.rupress.org/content/103/6/2747.full.pdf` (cit. on p. 17).

[65]A. Mogilner and G. Oster, "Cell motility driven by actin polymerization," Biophysical Journal **71**, 3030 –3045 (1996) (cit. on pp. 28, 66).

[66]A. Mogilner and G. Oster, "The physics of lamellipodial protrusion," European Biophysics Journal **25**, 47–53 (1996) (cit. on p. 28).

[67]D. Das, D. Das, and R. Padinhateeri, "Force-induced dynamical properties of multiple cytoskeletal filaments are distinct from that of single filaments," PLOS ONE **9**, 1–21 (2014) (cit. on p. 29).

[68]A. Mogilner and G. Oster, "The polymerization ratchet model explains the force-velocity relation for growing microtubules," European Biophysics Journal **28**, 235–242 (1999) (cit. on p. 29).

[69]A. Mogilner and G. Oster, "Force generation by actin polymerization ii: the elastic ratchet and tethered filaments," Biophysical Journal **84**, 1591 –1605 (2003) (cit. on p. 29).

[70]R. K. Sadhu and S. Chatterjee, "Actin filaments growing against an elastic membrane: effect of membrane tension," Phys. Rev. E **97**, 032408 (2018) (cit. on pp. 31, 46, 59, 69, 81).

[71]*Statistical mechanics of membranes and surfaces* (World Scientific, 2004) (cit. on p. 31).

[72]R. Lipowsky and S. Grotehans, "Renormalization of hydration forces by collective protrusion modes," Biophysical Chemistry **49**, 27 –37 (1994) (cit. on pp. 31, 44, 46).

[73]A. Volmer, U. Seifert, and R. Lipowsky, "Critical behavior of interacting surfaces with tension," The European Physical Journal B - Condensed Matter and Complex Systems **5**, 811–823 (1998) (cit. on pp. 31, 44, 46).

[74]R. Lipowsky and S. Grotehans, "Hydration vs. protrusion forces between lipid bilayers," EPL (Europhysics Letters) **23**, 599 (1993) (cit. on pp. 31, 44, 46).

[75]B. Fogelson and A. Mogilner, "Computational estimates of membrane flow and tension gradient in motile cells," PLOS ONE **9**, 1–12 (2014) (cit. on p. 45).

[76]Y. Schweitzer, A. Lieber, K. Keren, and M. Kozlov, "Theoretical analysis of membrane tension in moving cells," Biophysical Journal **106**, 84 –92 (2014) (cit. on p. 45).

[77]X. Li and A. B. Kolomeisky, "The role of multifilament structures and lateral interactions in dynamics of cytoskeleton proteins and assemblies," The Journal of Physical Chemistry B **119**, 4653–4661 (2015) (cit. on p. 66).

[78]R. K. Sadhu and S. Chatterjee, "Actin filaments pushing against a barrier: comparison between two force generation mechanisms," Eur. Phys. J. E, (In press) (2019) (cit. on p. 67).